REVIEW ARTICLE

Check for updates

Bulk COFs and COF nanosheets for electrochemical energy storage and conversion

Jie Li,† Xuechun Jing,† Qingqing Li, Siwu Li, Xing Gao, Xiao Feng [ID] * and Bo Wang [ID] *

Covalent organic frameworks (COFs) as an emerging class of crystalline porous materials have received much attention due to their tunable porosity, modifiable skeletons, and atomically precise structures. Besides, COFs can provide multiple high-rate charge carrier transport (electron, hole, and ion) pathways, including conjugated skeletons, overlapped π electron clouds among the stacked layers, and open channels with a variable chemical environment. Therefore, they have shown great potential in electrochemical energy storage (EES) and conversion (EEC). However, in bulk COFs, the defects always impede charge carrier conduction, and the difficulties in reaching deep-buried active sites by either electrons or ions lead to limited performance. To overcome these obstacles, numerous research studies have been carried out to obtain COF nanosheets (NSs). This review first describes the preparation strategies of COF NSs *via* bottom-up and top-down approaches. Then, the applications of bulk COFs and COF NSs in EES and EEC are summarized, such as in batteries, supercapacitors, and fuel cells. Finally, key challenges and future directions in these areas are discussed.

1. Introduction

Demand for continued energy supply is one of the tremendous challenges that we are facing today due to the disparity between increasing energy requirements and worldwide energy shortage. Electrochemical energy conversion (EEC) and storage (EES) are represented as the most effective technologies for the

Beijing Key Laboratory of Photoelectronic/Electrophotonic Conversion Materials, Key Laboratory of Cluster Science, Ministry of Education, School of Chemistry and Chemical Engineering, Beijing Institute of Technology, Beijing 100081, P. R. China. E-mail: bowang@bit.edu.cn, fengxiao86@bit.edu.cn
† These authors contributed equally to this work.

utilization of energy. The EEC techniques can convert sustainable energy sources (*e.g.*, wind energy and solar energy) into transportable and stable chemical energy.[1–4] To obtain higher energy densities and energy conversion efficiency, developing novel materials with high performance is of vital importance.[5–13]

Covalent organic frameworks (COFs), assembled by covalent bonds through reversible reactions, have the advantage of high porosity,[14,15] adjustable and periodic pores,[16–19] well-defined structures,[20,21] and functional skeletons.[22,23] The reversibility of the polymerization reaction allows "error corrections" to ensure the obtaining of thermodynamically stable networks with long-range order.[20,24] COFs have been widely applied in

Jie Li received her Bachelor's degree from Wuhan University of Technology in 2016. She then joined Prof. Bo Wang's group as a doctoral student at the School of Chemistry and Chemical Engineering, Beijing Institute of Technology. Her research interests include design, synthesis, and functional application of novel metal–organic frameworks and covalent organic frameworks.

Jie Li

Xuechun Jing received her Bachelor's degree from Qingdao University of Science and Technology in 2018 and then joined Prof. Bo Wang's group as a MS student at the School of Chemistry and Chemical Engineering, Beijing Institute of Technology. Her current research focuses on the synthesis and application of covalent organic framework films.

Xuechun Jing

This journal is © The Royal Society of Chemistry 2020

Chem. Soc. Rev., 2020, **49**, 3565–3604 | **3565**

storage and sorption,[25–28] separation,[29–32] catalysis,[33–39] sensing,[40–42] optoelectronics,[43–47] and so on. The first COFs were synthesized by Yaghi and co-workers in 2005.[48] The successful preparation of COFs has overcome the "crystallization problem", *i.e.* the covalent bonding of building blocks often produces amorphous or poorly crystalline polymeric materials, and makes it possible to design and prepare polymers with highly ordered and predictable primary, secondary, and tertiary structures based on the reticular chemistry principle. Furthermore, the recent achievement of producing high-quality single crystals enables the deciphering of their structures with atomic precision.[49,50]

COFs can be categorized into two dimensional (2D) and three dimensional (3D) COFs depending on the geometric symmetry of the building blocks (Fig. 1).[51–55] In 2D COFs, the organic units are covalently bonded and restricted in 2D sheets that further stack to form a layered structure *via* π–π interaction. Most of them are stacked in eclipsed mode with the formation of periodically aligned channels, while very few of them are stacked in a staggered fashion.[15,51] Both stacking modes show well-defined arrangements. For 3D COFs, their building blocks including an sp³ carbon, silane, or boron atom help to expand the network to three-dimensional space. Furthermore, the diversity of building blocks creates numerous combinations, which endows the COFs with immense possibilities in structural design (Fig. 2).[56]

The unique structural features of COFs endow them with great advantages and potential for application in EES and EEC. (a) Periodic arrangement. The redox/catalytic active sites can be accurately anchored to specific sites on the skeleton with the predesigned environment, and their electronic structures can be easily tuned, offering great opportunities for tailoring the performance of COFs and serving as platforms for the mechanism and structure–function relationship study. Moreover, in 2D COFs, vertical columnar arrays formed by the stacking of aromatic building units as well as conjugated polymeric layers can provide continuous channels for the hole and/or electron
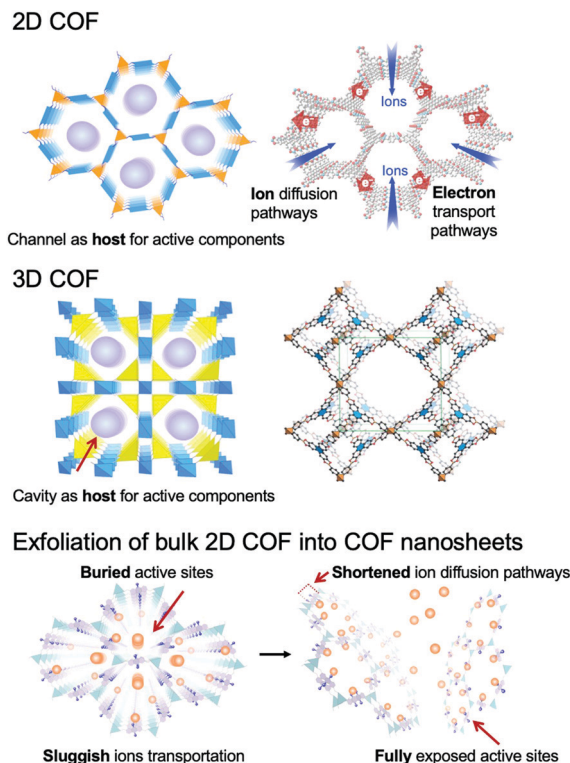

Fig. 1 Schematic representation of 2D COFs, 3D COFs, and the exfoliation of the bulk 2D COF into COF nanosheets. The atomic connectivity and structure of 3D COFs (right) is reproduced from ref. 53 with permission from American Association for the Advancement of Science, copyright 2007.

movement.[57–60] In 3D COFs, the 1D conjugated segments interlace with each other and construct long-range conjugated systems that may also provide transport pathways. (b) Porous framework with well-aligned channels. Normally, both 2D and 3D COFs have the advantages of modified skeletons, multiple open sites, and a highly porous structure with large pore volume. Because of these advantages, COFs provide the possibility of incorporating active fragments into their skeletons or

Xiao Feng received his BS degree in materials chemistry in 2008 and PhD degree in materials science in 2013 from Beijing Institute of Technology. He pursued his study in Japan as a joint PhD student at the Institute for Molecular Science (2009–2012). He is now a professor at Beijing Institute of Technology and is mainly engaged in the research of crystalline porous materials (e.g., covalent organic frameworks and metal–organic frameworks) and their applications in membrane separation.

Xiao Feng

Bo Wang obtained his BS and MS degrees from Peking University in 2004 and the University of Michigan in 2006, respectively, and his PhD from the University of California Los Angeles in 2008. He has been a professor in the School of Chemistry and Chemical Engineering, Beijing Institute of Technology, since 2011. His research interests focus on novel functional porous materials design and synthesis, energy storage, advanced battery materials, gas purification, toxicant capture, and sensing.

Bo Wang

3566 | *Chem. Soc. Rev.*, 2020, **49**, 3565–3604

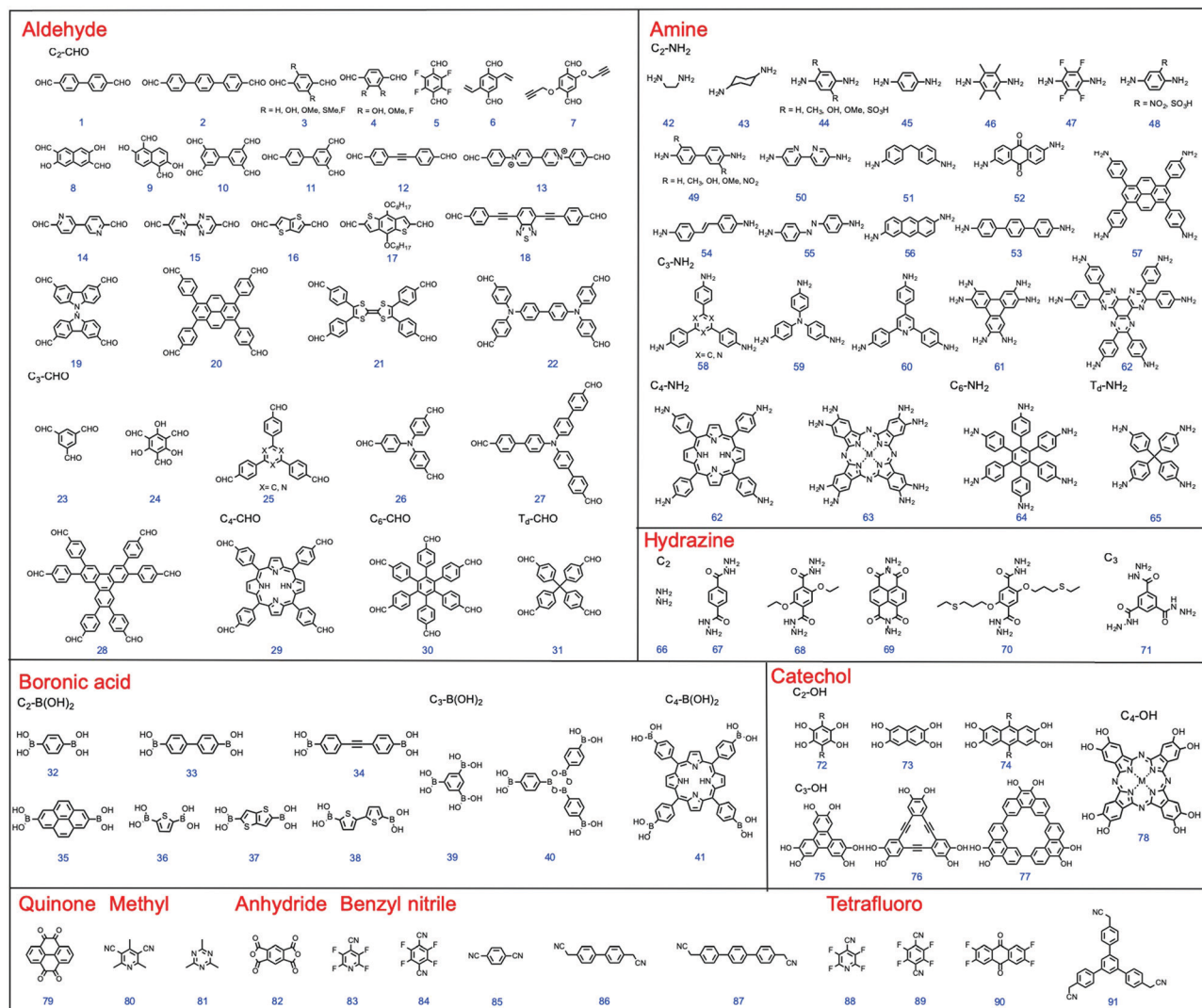This journal is © The Royal Society of Chemistry 2020

Fig. 2 Chemical structures of building blocks with different geometries.

impregnating active molecules within their channels. The ability for selective adsorption or enrichment of particular reactants, like gases or ions,[26] inside their channels is beneficial for electrochemical reactions. In addition, the open channels of COFs are capable of permitting ion migration;[61] especially, the ionic COFs or COFs encapsulated with carriers can efficiently accelerate ion transport.

In the past few years, COFs have been broadly investigated in the EES and EEC fields (Fig. 3).[62–65] Although 2D COFs are good electro-functional materials, long channels formed by stacked layers pose a great obstacle for ion diffusion and for reaching the active sites, and the defects of COFs and boundaries between particles restrict the transportation of electrons and ions. These issues lead to an increased mass transport resistance and inherent low conductivity of bulk COFs, which limit their applications. Remarkably, the sheet-like COFs with a thickness of single- or few-atom layers possess unique chemical, physical, electronic, and optical properties.[66–68] They can minimize the transport length for the ions to reach the active sites, and

provide sufficient electron conduction pathways from the electrodes or conductive additives to the active sites in COFs. Specifically, COF NSs with adjustable electronic/optoelectronic properties and fully exposed active sites are of particular interest for EES and EEC applications.

Specifically, for battery electrodes and supercapacitors, the shortened ion diffusion pathways and more accessible active sites in the COF NSs give rise to an elevated rate performance; for anode materials, the sheet-like structure provides the capability of accommodating ions between the layers based on the manner in which ions are inserted, even the single-layered COF NSs can follow the surface ion storage mechanism where ions are exchanged on the surface of electrodes during the charging–discharging processes; for supercapacitors, COF NSs by virtue of their porous nature and higher specific surface area are helpful for wetting the electrode surface by electrolytes and absorbing ions, resulting in improving their specific capacitances. As for electrocatalysts: (a) compared with the bulk COFs, COF NSs possess more accessible active sites on

This journal is © The Royal Society of Chemistry 2020

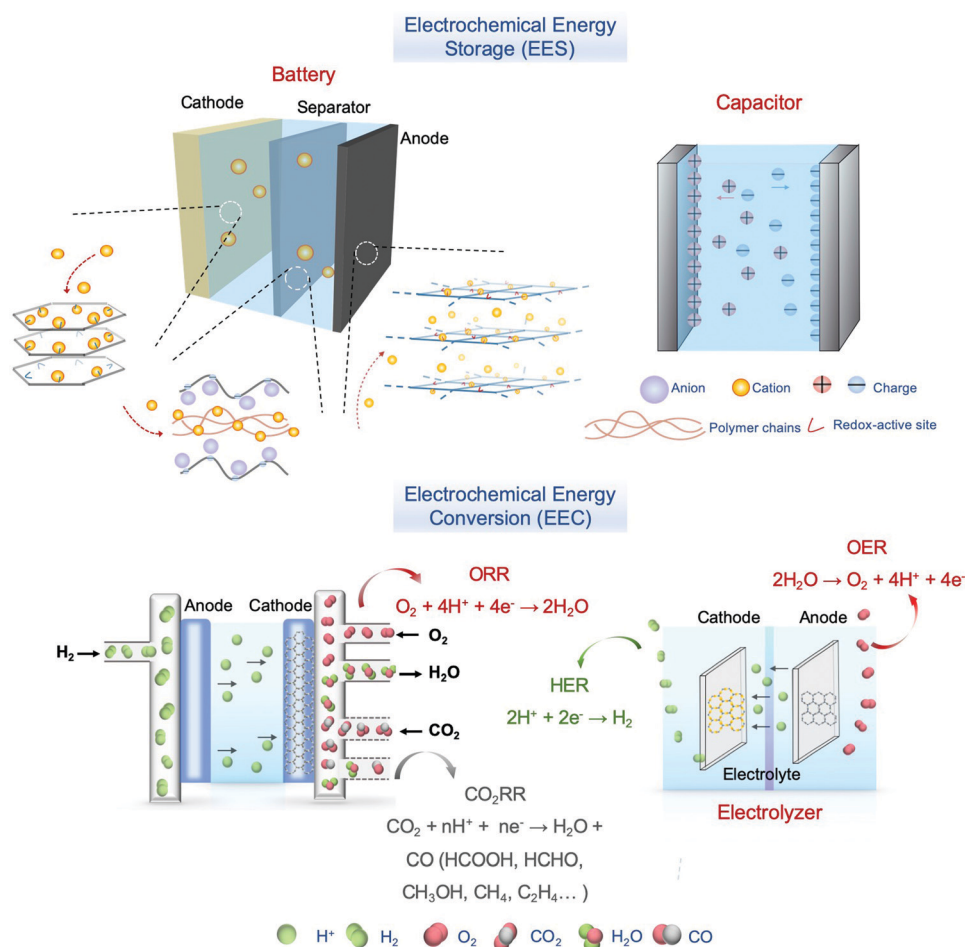Chem. Soc. Rev., 2020, 49, 3565–3604 | 3567

Fig. 3 Conceptual presentation of an integrated system of EES and EEC.

the surface that are able to directly contact substrate molecules as well as electrons with a lower diffusion/transportation barrier; (b) in terms of metal-containing COF-based electrocatalysts, the ultrathin nanosheet structures are conducive to the incorporation of metal atoms/clusters in a similar chemical and physical environment, benefiting the study of the structure–function relationship and the modulation of their performance; (c) generally, COF NSs exhibit a better dispersibility in solvents, making it easier to afford electrodes with uniform coverage of active materials.

Many reviews focusing on COFs in EES and EEC fields have been summed up,[69–72] but few have discussed the fundamental understanding of the relationship between COFs' structure and their electrochemical performance. In this review, we have presented the most recent progress, emphasized the importance of preparing 2D COF nanosheets for their electrochemical applications, highlighted the transport pathways of electrons and ions in COFs, established the association between the functions of COFs and their applications, and evaluated their performance from structural design. Firstly, we have summarized the synthetic methods for COF NSs and thin films which have been classified into bottom-up and top-down approaches; then we discussed the development of COFs in EES and

EEC applications, including in rechargeable batteries, supercapacitors, as well as electrocatalysis; in the final part, we have discussed the challenges that still exist in these areas and have provided some perspectives.

2. Synthesis of COF nanosheets

Bulk COF materials can be prepared under solvothermal, microwave, ionothermal, or mechanical conditions, and many previous reviews have summarized and discussed these methods in detail.[15,46,51] Thus, in the following sections, we have mainly introduced the strategies for the preparation of COF NSs and thin films, which are classified into bottom-up and top-down methodologies (Fig. 4).

2.1 Bottom-up synthesis

The bottom-up strategy is an approach of great importance to fabricate COF NSs and thin films, the key point of which is the preorganization of precursors and the restriction of condensation reactions between the monomers in well-confined spaces, such as the surface of smooth substrates or the interface between two phases.
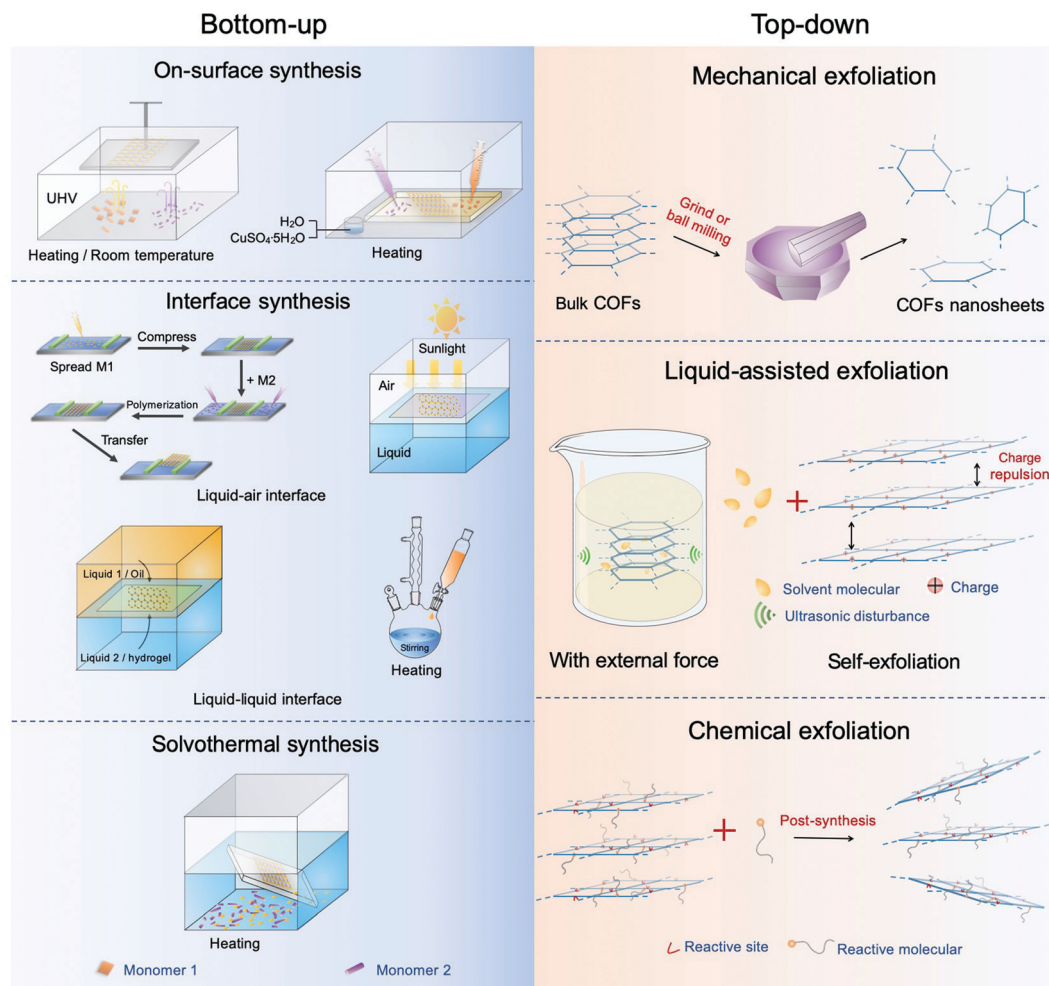
3568 | Chem. Soc. Rev., 2020, 49, 3565–3604

This journal is © The Royal Society of Chemistry 2020

Fig. 4 Diagram of the synthesis of CONs. The left represents the bottom-up method and the right top-down synthesis.

For the preparation of COF NSs with atomic thickness, generally, an on-surface strategy is employed. It is crucial to control the growth orientation of COF NSs or thin films and avoid random dispersion or accumulation of monomers on substrates. Therefore, the selected substrates, such as highly oriented pyrolytic graphite (HOPG) and metals, should possess a well-defined single-crystal surface to guide the polymerization reactions. Very recently, few-layered COF NSs were successfully prepared with the aid of surfactants or laminar assembly polymerization (LAP).[73]

In comparison, the conditions for the fabrication of COF thin films with multilayer nanosheet-stacked structures are not so strict, but it is required to carefully optimize the temperature, monomer concentration, solvent polarity, substrate, *etc.*

2.1.1 Single-layered covalent organic frameworks (sCOFs). The on-surface synthesis approach has been proved to be one of the most efficient ways to produce single-layered COF nanosheets. The atomic arrangement of sCOFs can be well visualized by scanning tunneling microscopy (STM) with high resolution. Compared with the supramolecular systems organized by non-covalent interactions, sCOFs linked by covalent bonds are more chemo- and thermo-robust. Indeed,

the reversibility of the condensation reaction is of vital importance to ensure error-checking and proof-reading processes to yield COFs with long-range order. However, for the preparation of sCOFs, in addition to reversible reactions like imine coupling and boronic anhydridation reaction, irreversible reactions (*e.g.*, Ullmann coupling) can also be applied owing to the pre-organization of the monomers guided by the ultra-flat surface.

2.1.1.1 Chemical vapor deposition growth under ultrahigh vacuum (UHV). The pioneers of on-surface synthesis of 2D covalently bonded molecular nanostructures are Grill and Hecht *et al.*,[74] who reported that molecular nanostructures containing porphyrin building blocks and linked by covalent bonds were successfully formed on Au(111) surface after thermal activation. Moreover, they also noted that the resulting nano-architectures with controlled shape and size could be precisely manipulated by changing the chemical structures of the construction units. To activate the molecular building blocks, they proposed two alternative methods but obtained similar products. The first one was depositing the intact molecules on the metal surface and then dissociating the Br substituents by heating. The second one was activating the molecules in the evaporator
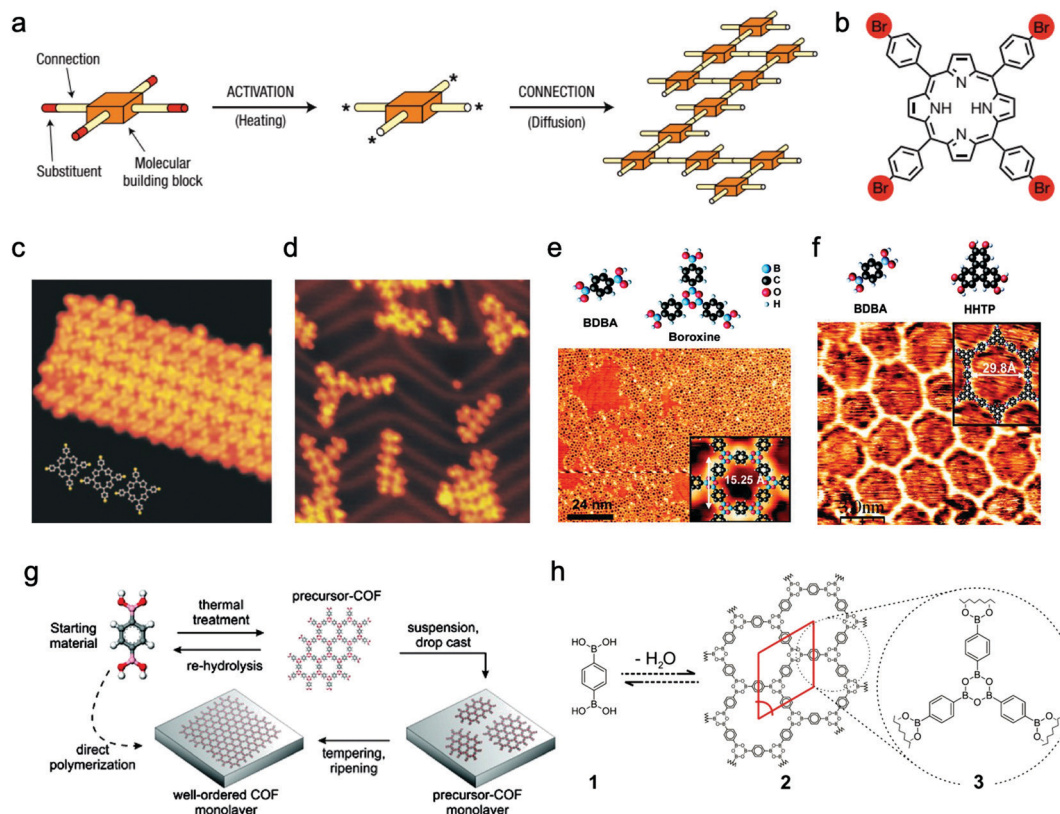
This journal is © The Royal Society of Chemistry 2020

Chem. Soc. Rev., 2020, **49**, 3565–3604 | **3569**

Fig. 5   (a) Schematic illustration of activated building units interconnected to form the covalent networks. (b) Molecular structure of Br$_4$TPP (Br atom is marked red). (c) STM image of unactivated Br$_4$TPP deposited on Au(111) at a low evaporator temperature of 550 K. (d) In method (ii), the molecules are activated to form a network on the surface of Au(111) at an evaporator temperature of 610 K. Reproduced from ref. 74 with permission from Nature Publishing Group, copyright 2007. (e) Construction units (upper left: BDBA, upper right: three BDBA monomers form boroxine by dehydration condensation) and STM image of nearly single-layered sCOF-1 on Ag(111). (f) Top: Molecular structures of BDBA and HHTP; bottom: STM image of SCOF-2 on Ag(111). Reproduced from ref. 77 with permission from American Chemical Society, copyright 2008. (g) Schematic illustration of the two methods. (h) Reaction scheme for self-condensation of BDBA monomers. Reproduced from ref. 105 with permission from American Chemical Society, copyright 2011.

and then depositing them onto the metal surface at room temperature (Fig. 5a–d). By comparison, the former method was more efficient, attributed to the enhanced molecular diffusion and clustering of networks upon heating compared to that at room temperature. Similarly, other halogenated aromatic monomers have been utilized for the preparation of sCOFs under UHV conditions.[75,76]

Boronate linkage with planar molecular configuration and good reversibility has been applied for constructing sCOFs.[77–81] In 2008, Abel et al.[77] prepared sCOFs with tunable nanoporous structures on Ag(111) surface under UHV by using boronate-based building units. Both sCOF-1 (obtained by self-condensation of 1,4-benzenediboronic acid (BDBA) (32)) and sCOF-2 (obtained by co-condensation of BDBA and 2,3,6,7,10,11-hexahydroxytriphenylene (HHTP) (40)) displayed energetically favorable structures and formed a hexagonal array with boroxine or triphenylene moieties at the nodes (Fig. 5e and f). Since the network of sCOF-2 showed fewer defects compared to that of sCOF-1, they thought that it could be attributed to the fact that the bimolecular reaction for dioxaborole formation was more kinetically favorable than the trimolecular boroxine reaction and the HHTP units may

help to improve the rigidity of the networks. They found that the temperature of the substrate and evaporator, as well as the annealing process, greatly influenced the surface coverage by sCOFs. In 2012, Zamora, Gómez-Rodríguez et al. reported the formation of a sCOF on Au(111) based on polyester condensation under UHV.[82] In 2015, Chi and Li et al. showed that the cyclotrimerization of acetyls to aromatics can also be used for the preparation of sCOFs on the surface under UHV.[83] In addition, Schiff-base coupling between primary amines and aldehydes is of great interest in the on-surface synthesis of sCOFs.[84–87]

2.1.1.2 Thermal polymerization at ambient pressure. The process of implementing UHV conditions is complex, and the instrumentation and also single-crystal metallic surfaces have to meet high requirements. Alternatively, solution deposition may serve as a more efficient and simpler preparation route to obtain long-range ordered sCOFs. However, after solution deposition, the aryl–aryl coupling reaction proceeded on a heated gold surface only afforded dimers and trimers.[88] The long-range ordered sCOFs with high surface coverage have been

successfully prepared by reversible dehydration reactions with the manipulation of the amount of water.[86,89–104]

In 2011, Lackinger et al. first deposited BDBA monomers with boronic acid groups or nanocrystalline precursor COFs on the graphite surface by drop-casting (Fig. 5g and h), and then positioned the samples in a container placed within a preheated oven.[105] Additional water was added in the reactor but did not directly contact the samples, and the container remained slightly open to maintain the ambient environment during the reaction. They found that the presence of water molecules was helpful for dominating the growth of COFs, which came to an end when all the water molecules were evaporated. STM characterization showed that the resulting monolayers of COF-1 formed on the graphite substrate with or without precondensation seemed to be indistinguishable regarding lattice parameters, domain size, and defect density. Then they obtained a series of high-quality sCOFs with pore sizes ranging from 1.0 to 3.2 nm by choosing building blocks with different lengths.[91] Additionally, they investigated the impact of the activation temperature on molecule diffusion ability and reaction rate. They observed the structural characteristics of both sCOFs and noncovalently self-assembled structures depositing on the surface before the thermally activated polycondensation. Furthermore, Lei and Tian et al.[106] reported that they successfully co-condensed triangular aromatic aldehydes and linear aromatic diamines based on Schiff-base reaction at the octanoic acid/HOPG interface either at room temperature or in a low vacuum with moderate heating.

In 2012, Wan and Wang et al. successfully fabricated well-ordered and large-scale sCOF-1 with a domain size of 200 × 200 nm^2 on HOPG by modulating the chemical equilibrium via introducing $CuSO_4 \cdot 5H_2O$ into a closed reaction system. The controlled experiments without the addition of $CuSO_4 \cdot 5H_2O$ only resulted in products with disordered networks.[89] Then they successfully produced another three ordered sCOFs with triangular, rhombille, or semi-regular Archimedean tilings, via Schiff-base reaction on the surface of HOPG with the aid of $CuSO_4 \cdot 5H_2O$.[107]

Notably, most of the sCOFs usually possess single linkages. To further broaden the variety of sCOF structures, it is attractive to develop multi-component molecular covalent nanoarchitectures. Wang's group proved that Schiff-base reaction and boronic acid dehydration have orthogonality; in other words, they can take place simultaneously during on-surface synthesis without interference with each other.[100] They adopted the gas–solid (HOPG) interface reaction methods to prepare highly ordered hybrid sCOFs linked by boroxine rings and imine bonds. Moreover, they successfully synthesized the first chiral sCOF with a windmill structure.

Kunitake et al. proved that extended 2D networks could be fabricated via a surface-mediated Schiff-base reaction on hydrophobic iodine-modified Au(111) surface in aqueous solution with precise pH and thermodynamic control.[90] They emphasized the importance of choosing substrates and monomers. This method avoided complicated operations such as high temperature and ultrahigh vacuum. It paved the way

for the synthesis of well-designed sCOFs via facile ways of "bottom-up" methodology.

2.1.1.3 Influencing factors. The on-surface synthesis of 2D sCOFs contains many kinetic processes such as adsorption, diffusion, nucleation, growth, etc. In order to obtain well-ordered and high-quality 2D sCOFs, the density of the nucleus, the diffusion rate of the precursors, and the growth rate should be taken into account. In most cases, the suitable growth conditions for the formation of 2D sCOFs include low nucleus density, high diffusion rate, and slow growth rate to guarantee a large domain size, high reaction efficiency, and thermodynamically stable structures, respectively. In this part, we have discussed the primary influencing factors for sCOF growth.

(a) Thermodynamic equilibrium control. The key to produce ordered and uniform molecular networks constructed with covalent bonds is the regulation of the reaction equilibrium and reversibility.

The substrate or system temperature will affect the reaction rate, and consequently, the quality of the sCOFs. Usually, the condensation reaction does not occur at low temperature; however excessively high temperature leads to a large number of defects caused by desorption or excessive polymerization of monomers.[82,83] Therefore, a suitable temperature range that allows the reaction to proceed in a controllable and reversible manner is of great importance.

The reversible surface polycondensation is considered to be endothermic, and thus, elimination and release of water molecules will entropically promote the forward reaction. According to Le Chatelier's principle, the reversibility of the condensation reaction, which determines the domain size and defect degree, can be manipulated by water control. In the above-mentioned methodologies, the amount of water in the reaction system has been managed by additional water supplement, pressure control, or adding aquo-complex. For example, $CuSO_4 \cdot 5H_2O$ in the closed system acted as a water "reservoir". During heating, the water molecules were released from $CuSO_4 \cdot 5H_2O$ to facilitate defect repair via decomposing and reconnecting mislinked units; on the other hand, during the cooling process, these water molecules would be soaked up again by anhydrous $CuSO_4$ to prevent the sCOFs from decomposition.[89,107]

(b) Substrate. In addition to the ability to guide the polymerization process, substrates also have a great influence on the adsorption capacity and diffusion degree of the precursor molecules on them.[75,76,79,108,109] Therefore, substrates play significant roles in increasing the coverage, regularity, and orientation of the resultant polymeric sCOFs. Substrates with single-crystal surfaces are required to produce high-quality sCOFs for the on-surface synthetic procedures. For example, Gutzler and Lackinger et al. polymerized halogenated aromatic monomers under UHV and found that the dissociation of covalent carbon–halogen bonds and subsequent association of radicals were different on graphite(001), Cu(111), and Ag(110), respectively.[75] Bieri and Fasel et al. prepared polyphenylene networks by covalent bonding of the hexaiodo-substituted

This journal is © The Royal Society of Chemistry 2020

Chem. Soc. Rev., 2020, **49**, 3565–3604 | **3571**

macrocycle on Cu(111), Au(111), and Ag(111).[76] They found that the morphologies of the resultant products were significantly different on different substrates. Density functional theory (DFT) analysis revealed that the equilibrium of diffusion and coupling pathways of the precursors influenced by substrates were different. On Cu(111), the formation of covalent intermolecular bonds between radicals occurred spontaneously as soon as the primal diffusion barrier was overcome. In contrast, the diffusion progress proceeded prior to the intermolecular coupling on the Ag surface, thus promoting the motion of the radicals and resulting in well-ordered 2D networks.

(c) *Monomer.* Monomers, as well as their relative ratios, also have strong impacts on the structure, stability, uniformity, and application properties of sCOFs.[86,92–98,110]

Wan and Wang *et al.* investigated the effects of monomer diffusion and the molecule–substrate interaction by changing the length and rigidity of the monomer skeleton. They demonstrated that the increase of substrate–molecule interaction preferred to form macrocycle structures rather than sCOFs due to the poor mobility of the adsorbates.[110] They also demonstrated that sCOFs synthesized on the surface by using tetrathiafulvalene equipped with four benzaldehyde groups (4ATTF) (21) and two linear diamine molecules with different lengths as precursors showed compelling differences.[93] When reacted with *p*-phenylenediamine (PPDA) (45), 4ATTF was inclined to form long-range ordered rhombus structures. In contrast, 4ATTF when reacted with 1,1′-biphenyl-4,4′-diamine dihydrochloride (BPDA) (49) resulted in the formation of triangular and irregular rhombus structures.

Lei's group investigated the influence of precursor concentration on the production of sCOFs.[95] They proved that, when reacting with the same aldehyde, the larger amine monomer demanded lower concentration to form a well-ordered crystalline 2D polymer. Wang's group used tetradentate monomer 1,3,6,8-tetrakis(*p*-formylphenyl)pyrene (20) with D_{2h} symmetry and ditopic linear diamines to prepare sCOFs whose network shape varied from rhombus, parallelogram, and Kagome. They illustrated that high precursor concentration led to the formation of quadrate networks, while low concentration resulted in Kagome networks.[97]

2.1.2 COF multilayer nanosheets and thin films

2.1.2.1 Solvothermal method. The solvothermal synthesis method as a typical wet-chemical synthesis strategy is widely applied to produce ultrathin 2D nanomaterials. During the solvothermal synthesis, water or an organic solvent works as the reaction medium in a closed system and the heating temperature is set above the boiling point of the solvent. The heated solvents in high pressure can facilitate the reaction and enhance the crystallinity of nanocrystals.[111] The solvothermal method has also been used to prepare COF multilayer nanosheets and thin films with or without the presence of substrate soaking in the solvents.[112–119]

In a typical example, Dichtel *et al.* reported that 2D COF-5 thin films can be formed on the surface of single-layer graphene (SLG) supported by copper, silicon carbide, or transparent fused silica (SiO₂) substrates in a mixture of monomers and solvents at 90 °C (Fig. 6a–d).[120] Compared with the corresponding COF powder sample, the COF film possessed a much higher orientation, in which the polymeric layers stacked normal to the SLG surface.

Talyzin's group developed a hybrid 2D–2D material consisting of perpendicularly oriented COF-1 NSs and graphene (Fig. 6e).[112] For directing the vertical growth of COF-1 NSs, they modified graphene oxide with diboronic acid molecules to function as nucleation sites. The thickness of COF-1 NSs was controlled from about 3 to 15 nm. Besides, Wang's group realized the growth of boronic ester-based COFs on carbon nanotubes (CNTs) to form COF-10@CNT with a few-layered structure. It can be seen from the high-resolution transmission electron microscope (HRTEM) images that the CNTs were covered by a COF-10 thin layered structure (about 6 nm) with a layer spacing of 0.35 nm.[121]

2.1.2.2 Interface synthesis. Liquid/air and liquid/liquid interfaces can provide confined spaces for the preparation of 2D COF nanosheets or films.

For instance, Zhang's group prepared Schiff-base 2D COF NSs with a thickness of about 0.7 nm at the air/water interface by the Langmuir–Blodgett method.[122] Bao's group placed the reaction solution in a covered Petri dish for 2 days in an ambient environment and the COF films were formed at the solution/air interface. The surfaces of the resulting films were smooth and the thickness could be tailored from 1.8 nm to 29 nm by altering the monomer concentration and reaction time.[123] Choi *et al.* found that the formation of the COF NSs at the air/water interface could be significantly shortened to less than 1 h by photon irradiation, and the thickness of the resultant COF NSs was 0.75–2.59 nm (Fig. 6f and g).[117,124] They noted that photon energy played a vital role in both accelerating imine condensation and facilitating the transformation from generated amorphous imine to crystalline COFs.

Feng's group prepared crystalline quasi-two-dimensional (q2D) polyaniline (PANI) films at the air–water interface by using surfactant (sodium oleyl sulfate, SOS) monolayers as the template. The obtained crystalline q2D PANI films possessed lateral sizes of 50 cm² and tunable thickness (2.6–30 nm).[125] Furthermore, Feng, Zheng, and Kaiser *et al.* successfully proposed a surfactant-monolayer-assisted interfacial synthesis (SMAIS) strategy to synthesize crystalline few-layered 2D polyimide (2DPI) and 2D polyamide (2DPA) at the interface of water and air with the aid of surfactant monolayers (sodium oleyl sulfate, SOS). The obtained 2DPI possessed a thickness of about 2 nm and a crystal domain size of about 3.5 μm², while these values for 2DPA were 10 nm and 0.4 nm μm², respectively. They also identified that the amorphous areas connected with crystalline domains dominated about 40% area (Fig. 7a–e).[126] Very recently, Feng, Dong, Zheng, and Kaiser *et al.* used a similar strategy to synthesize three fully crystalline PI-2DPs with tunable thickness (6 to 200 nm) and crystalline domain (100–150 nm in size), which were one order of magnitude larger than those of previously reported 2D polyimine films.[127] Feng, Dong, and Cuniberti *et al.* further prepared 2D crystalline boronate ester

3572 | *Chem. Soc. Rev.*, 2020, **49**, 3565–3604

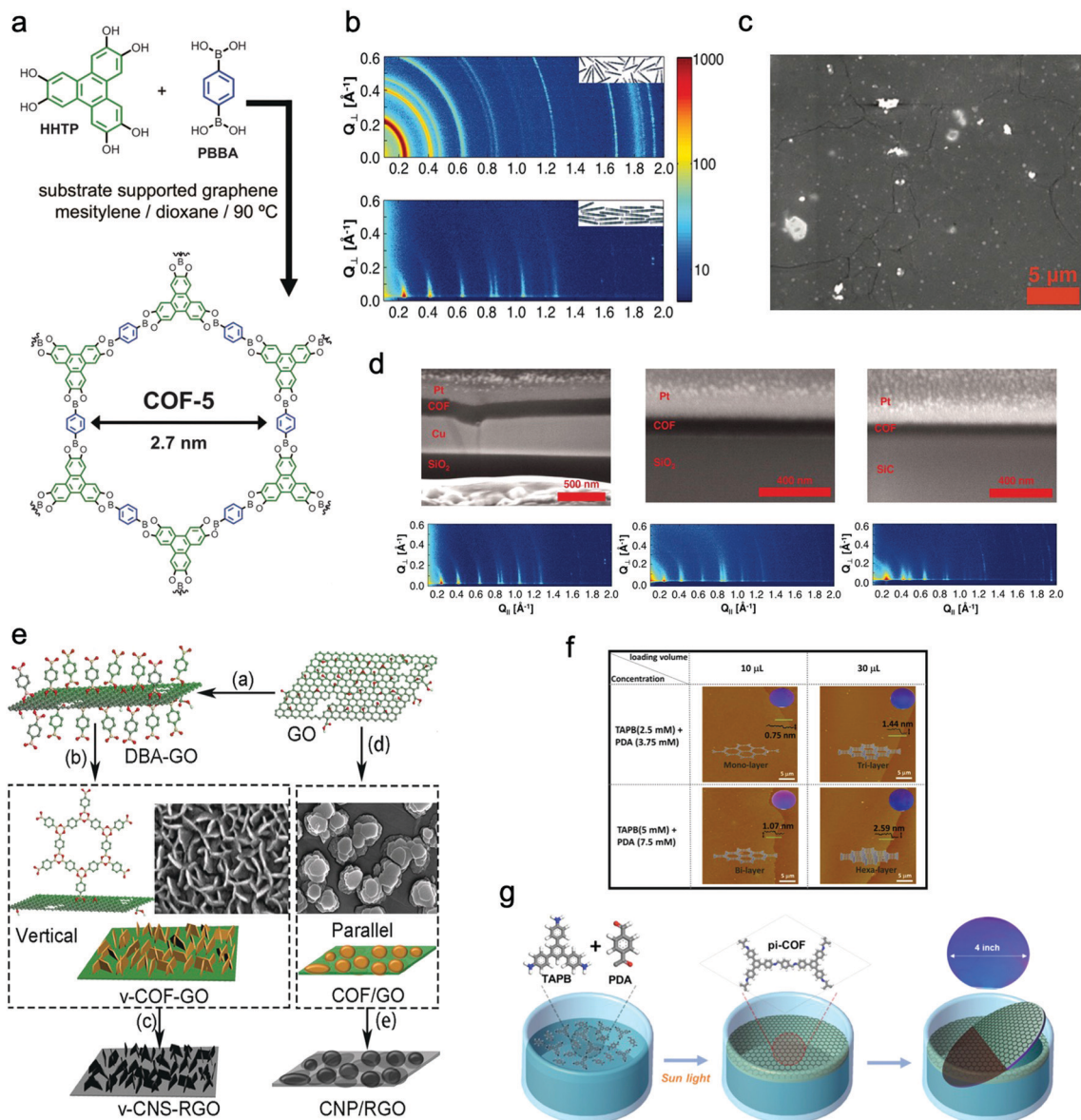This journal is © The Royal Society of Chemistry 2020

Fig. 6 (a) Schematic illustration of the reaction of COF-5 films. (b) X-ray scattering data of the COF-5 powder (top) and GID data of the COF-5 film on SLG/Cu (down). (c) SEM image of the COF-5 thin film. (d) Cross-sectional SEM images and their corresponding GIDs of COF-5 films grown on SLG/Cu for 30 minutes, 2 hours, and 8 hours with film thicknesses of 195 ± 20 nm, 94 ± 5 nm, and 73 ± 3 nm, respectively. Reproduced from ref. 120 with permission from American Association for the Advancement of Science, copyright 2011. (e) Schematic illustration of the two methods: (a–b–c) functionalization of GO with DBA which worked as a vertically growing COF-1 nanosheet molecular nucleation site; (a–d–e) formation of COF-1 platelets parallel to GO in the absence of BDA for GO functionalization followed by carbonization to form carbon nanosheets oriented perpendicular or parallel to the RGO surface. Reproduced from ref. 112 with permission from Wiley-VCH Verlag GmbH & Co. KgaA, copyright 2018. (f) AFM images and thickness distribution of single, double, triple, and six 2D Lp-pi-COF films. (g) Schematic illustration of the reaction of Lp-pi-COF synthesized on the water interface with the assistance of photons. Reproduced from ref. 124 with permission from American Chemical Society, copyright 2018.

covalent organic framework (BECOF) films with tunable thickness (6–16 nm) and large single-crystalline domain up to 60 μm². [128]

Li and Ma et al. reported a buffering interlayer interface (BII) method to synthesize high-quality 2D COF NSs at the interface of two miscible organic solvents. [129] They introduced a low-density solvent interlayer between two miscible solvents to work as a buffer layer, in which the difference in density caused the directional movement of the interface.

Banerjee, Mukherjee, and Das et al. prepared a series of freestanding large-scale COF thin films with a thickness of sub-100 nm at the liquid–liquid interface by Schiff-base reaction. [130] They introduced amine-p-toluene sulfonic acid (PTSA) salt to slow down the precursors' diffusion rate for increasing the crystallinity of films (Fig. 8a–c). Zhang, Ma, and Chen et al. transformed polymeric covalent organic frameworks (polyCOFs) into defect-free and freestanding films. The linear polymers PEG400/600 were used as building blocks to prepare the polymer
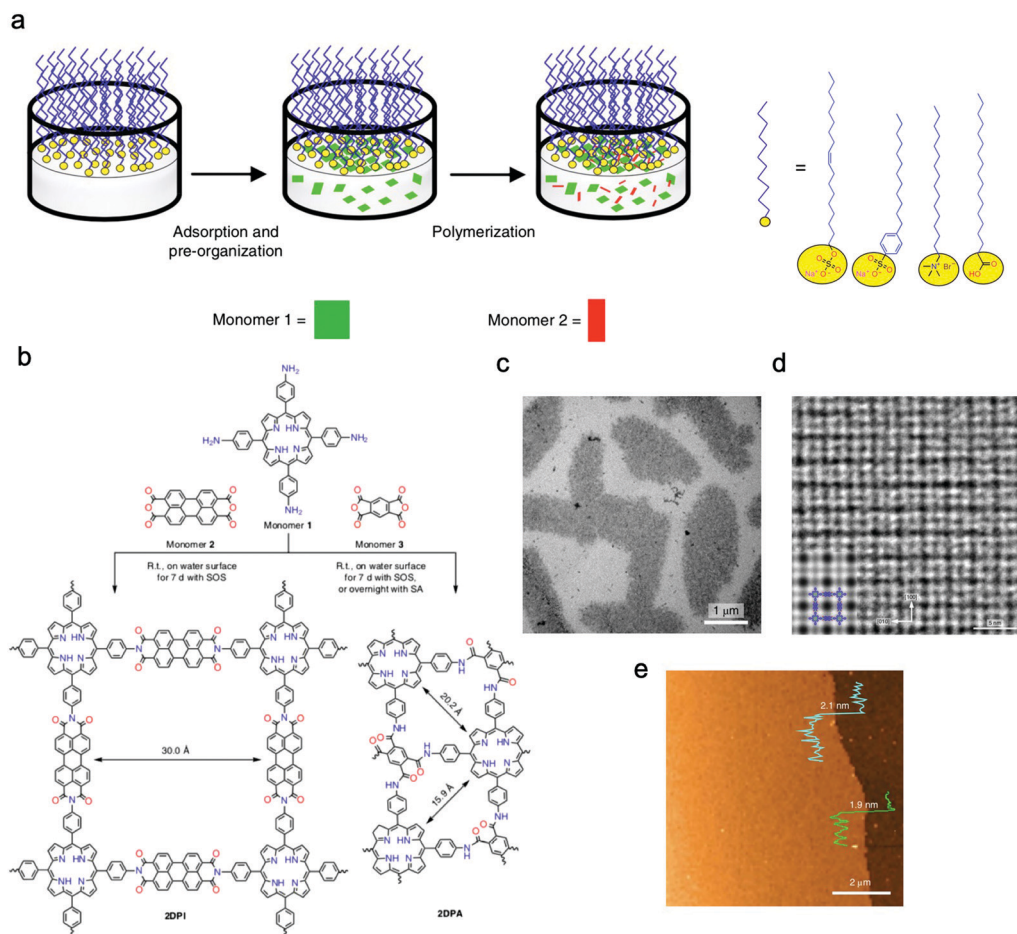
This journal is © The Royal Society of Chemistry 2020

Chem. Soc. Rev., 2020, 49, 3565–3604 | 3573

Fig. 7 (a) Schematic illustration of the synthetic procedure for the 2D polymers at the interface of water and air with the aid of surfactant monolayers. (b) Schematic illustration of the reaction of 2DPI and 2DPA. (c) A TEM image of the 2DPI film. (d) An AC-HRTEM image of 2DPI. (e) An AFM image of the 2DPI film. Reproduced from ref. 126 with permission from Nature Publishing Group, copyright 2019.

monomer (DTH-POLYMER) containing 2,5-diethoxy-terephthalo-hydrazide (DTH) (68) moieties, and then, DTH-POLYMER and DTH reacted with another monomer triformylbenzene (TB) (23) to form the final product poly$_x$COF-42 films at the interface between mesitylene and mixed solution of water and dioxane. What's more, they successfully synthesized films with a thickness of 4.5 ± 0.3 nm by adjusting the concentration of the reactants.[131]

Besides, Xu's group successfully proposed a solution-synthesis strategy to prepare triazine-based COF NSs with single-/multi-layered structures.[132] They first added CF_3SO_3H to a flask, and then the monomer solution (1,4-dicyanobenzene (85) in CH_2Cl_2) was introduced into the flask through a dropping funnel at a reaction temperature of 100 °C. Abundant liquid–liquid interfaces, where the cyclotrimerization reaction took place, were formed between the two insoluble solvent phases (Fig. 8d–f).

Wang and Liu *et al.* synthesized free-standing 2D COF films by using superspreading water layers between hydrogel and oil phase as a confined interface. In detail, 4,4′,4″-(1,3,5-triazine-2,4,6-triyl)trianiline (TTA) (58) was dissolved in the hydrogel while 2,5-dihydroxyterethaldehyde (DHTA) (3) was dissolved in the oil phase; the two monomers encountered and reacted in

the superspreading water layer to form COF films with tunable thickness ranging from 4 to 150 nm when changing the concentration of monomers (Fig. 8g and h).[133]

2.1.2.3 Influencing factors for few-layered COF NSs. In order to obtain highly qualified few-layered COF NSs for different applications, many factors should be taken into account, including monomer, solvent, reaction time, temperature, substrate, auxiliary reagent, and so on.

(a) Monomer. Types, concentration, ratio, and other related parameters of monomers greatly affect the preparation process, thickness, quality, number of layers, and other properties of COF NSs.[112,115,117,124,127,130,132,133]

Typically, the concentration of monomers plays an important role in controlling the thickness and layer number of COF NSs. In the process of preparing perpendicularly oriented COF-1 NSs on GO, Talyzin's group successfully controlled the thickness of films in the range of 3–15 nm by adjusting the loading of monomers.[112] Wang's group synthesized COF$_{TFPy}$-PPDA thin films on SLG by a solvothermal method, wherein they employed 1,3,6,8-tetrakis(*p*-formylphenyl)pyrene (TFPy) (20) and *p*-phenylenediamine (PPDA) (45) as building blocks.
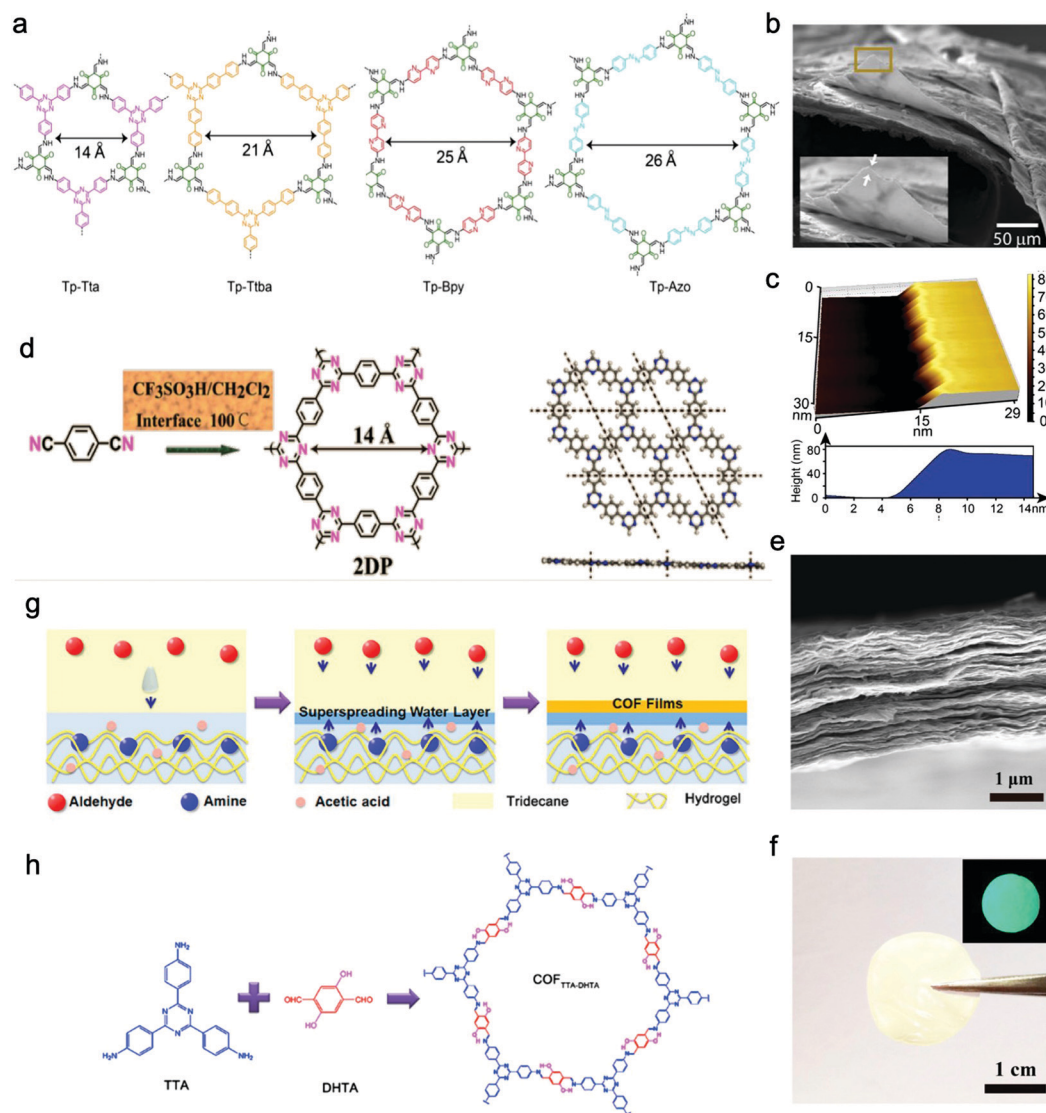
3574 | *Chem. Soc. Rev.*, 2020, **49**, 3565–3604

This journal is © The Royal Society of Chemistry 2020

Fig. 8 (a) Chemical structures of COF films (Tp-Tta, Tp-Ttba, Tp-Bpy, Tp-Azo). (b and c) SEM and AFM images of Tp-Bpy films. Reproduced from ref. 130 with permission from American Chemical Society, copyright 2017. (d) Schematic illustration of the reaction of triazine-based 2DP. (e) Cross-sectional SEM image of the 2DP film. (f) The photo of the self-supporting 2DP film. The inset is 2DP film's fluorescent picture under UV light. Reproduced from ref. 132 with permission from American Chemical Society, copyright 2017. (g) Schematic illustration of the formation of a self-supporting COF$_{TpPA}$ film at the oil/water/hydrogel interface. (h) Schematic illustration of the reaction of COF$_{TTA-DHTA}$. Reproduced from ref. 133 with permission from American Chemical Society, copyright 2018.

The thickness of the obtained thin films varied in the range of 47–55 nm, based on the concentration of TFPy from 2 to 5 mmol L^{-1}.[115] Choi *et al.* found that the number of layers for COF NSs at the air/water interface could be efficiently regulated by changing the concentration of the precursor solution (Fig. 6f).[117,124]

(b) Solvent. It is worth noting that the proper solvent combination is one of the key factors for preparing uniform and highly crystalline COF thin films. The solvent mixture with an appropriate ratio is beneficial for spreading the precursor solution homogeneously at the interface, which can be attributed to the polarity effect of the precursor solution.[117,124,132] Choi *et al.* synthesized polyimide-based COF (pi-COF) NSs at

the air/water interface. The solvent composition they used to dissolve the reactive monomers was 1,4-dioxane, mesitylene, chloroform, and acetic acid, by which they successfully controlled the polarity of the precursor solution, resulting in the formation of a uniform and stable layer on the water surface.[124]

(c) Reaction time. The duration of the reaction affects the thickness of the obtained COF thin films. For example, Bao's group prepared COF films at the solution/air interface in a covered Petri dish and they found that longer reaction time led to thicker films.[123]

(d) Substrate. Choosing a suitable substrate is regarded as one of the efficient ways to prepare COF thin films with a highly crystalline and ordered structure. The obtained COF thin films

This journal is © The Royal Society of Chemistry 2020

Chem. Soc. Rev., 2020, **49**, 3565–3604 | **3575**

have been shown to form 2D layers oriented preferentially parallel to the substrate surface and vertically aligned *via* π–π stacking.[120]

Dichtel *et al.* demonstrated that 2D COF-5 thin films can be formed on the surface of SLG supported by copper, silicon carbide, or transparent fused silica (SiO_2) substrates. They found that the COF-5 films exhibited a similar structure but a more uniform film/substrate interface and smaller thickness (94 ± 5 nm) on SLG/SiO_2 compared with that on SLG/Cu, while the COF-5 film formed on SLG/SiC showed no visible grain boundaries, few bulk crystallites, and the smallest thickness (73 ± 3 nm) (Fig. 6d).[120]

(e) Auxiliary regent. In some cases, adding auxiliary reagents (*e.g.*, surfactants[125–128] and regulators[119]) to the reaction systems can effectively regulate the structures and improve the quality of COF NSs.

For example, Feng, Zheng, and Kaiser *et al.* successfully synthesized few-layered 2D polyimide (2DPI) and 2D polyamide (2DPA) at the water–air interface with the aid of a surfactant (sodium oleyl sulfate, SOS). They further tried other surfactants with different polar groups, including sodium 4-dodecylbenzene-sulfonate (SDBS) and hexadecyl-trimethyl-ammonium bromide (CTAB). They found that in the pre-organization process, only when the surfactant (SDBS) and monomer 4,4′,4″,4‴-(porphyrin-5,10,15,20-tetrayl) tetraaniline (62) had electrostatic interaction it could lead to the formation of crystalline 2DPI. In contrast, if the surfactant (CTAB) and the monomers had electrostatic repulsion interaction, the obtained product was amorphous.[126]

In 2019, Jiang, Zeng, and Wang, *et al.* reported an imine-exchange synthesis strategy to prepare COF NSs by introducing excess 2,4,6-trimethylbenzaldehyde (TBA) into the reaction system under solvothermal conditions. During the formation of the COF, TBA molecules were attached to the edge of COF NSs, which hindered the accumulation of π–π stacking of COF NSs and promoted the growth of COF NSs along the 2D plane, realizing the control of NS layers, and the increase of yield as well as size. They successfully synthesized porphyrin-based COF-366, COF-367, COF-367-Co, TAPB-PDA COF, and TAPB-BPDA COF by using this method.[119]

2.2 Top-down method

Bulk 2D COFs are layered structures with periodically aligned channels. The individual polymeric layers are stacked along the vertical direction through relatively weak interactions (*e.g.* van der Waals force and/or hydrogen bonding). The top-down method can prepare multi-/mono-layered COF NSs by directly breaking the interactions between the neighboring layers of COFs, which is a facile and effective approach to obtain NSs. To date, the methodologies applied to exfoliate COFs can be divided into four classes, including mechanical exfoliation, liquid-assisted exfoliation, self-exfoliation, and chemical exfoliation.

2.2.1 Mechanical exfoliation. The mechanical delamination has been well established for graphene and other 2D materials.[111] Banerjee *et al.* first employed this method in 2013 to exfoliate COFs.[134] They prepared eight chemically

stable Schiff-base COFs with different functionalized diamines and pore apertures ranging from 15 to 24 Å. These COFs were exfoliated by using a simple and environmentally friendly strategy: firstly, the COFs were placed in a mortar with a few drops of methanol and ground using a pestle at room temperature for 30 min; secondly, the resulting dark red fine powder was dispersed in 100 mL of methanol and then centrifuged to get a clear liquid; finally, the COF NSs with flat nanosheet-like structures were obtained by complete removal of the solvent by evaporation. The size of the nanosheets was several micrometers in length, while their thickness ranged from 3 to 10 nm, corresponding to the presence of only ∼10–30 COF layers. The integrated structures of exfoliated nanosheets were characterized by Fourier Transform Infrared (FT-IR) and Raman spectroscopy. The random displacement of 2D layers in nanosheets affected the eclipsed pore structures and decreased the periodicity along the *z*-direction, as proved by the decrease of the intensity of powder X-ray diffraction (PXRD) assigned to the (100) plane and the broadening of the (001) diffraction.

Compared with pestle grinding,[134–136] ball milling[137–139] is a scalable mechanical delamination method to obtain COF NSs. As an example, a series of aromatic β-ketoenamine linked COFs with intramolecular C=O···HN hydrogen bonding were exfoliated by mechanical milling without solvent, operating at 30 Hz for 30 min.[139] The resultant powder was diluted with toluene (or water) and sonicated for 30 min. After removing big particulates by centrifugation, the visibly clear supernatant containing COF NSs was obtained. The COF NSs revealed approximately half-micron large sheets with the thickness in the range of 0.7–4.5 nm, corresponding to a stack of ∼2–15 COF sheets. Similarly, a Schiff-base COF was wet-ball milled in dimethyl formamide (DMF) (80 mL) at 225 rpm for 24 h. The resultant powder was dispersed by sonication for 30 min and then centrifuged, achieving few-layered nanosheets.[138]

2.2.2 Liquid-assisted exfoliation. Layered bulk COFs can also be exfoliated into ultrathin 2D nanosheets in liquid phase with external mechanical forces such as sonication.[140–149] At first, layered bulk materials are dispersed in a specific solvent with proper surface energy that matches COFs and then are sonicated to obtain a nanosheet suspension. During the operation, sonication introduces bubbles in the solution that provide microjets and shock waves across the layered bulk materials when the bubbles break. The produced intense tensile stress will be applied to the bulk materials, resulting in exfoliated sheets with a few layers.

Firstly, the solvent system is an essential factor for achieving efficient exfoliation in liquid.[140,144,149] The proper solvent system can both facilitate the exfoliation and inhibit the aggregation of the nanosheets. For instance, the relationship between different solvents and products for the exfoliation of 2D hydrazone-linked COF-43 with the expected stability of hydrazone linkages was investigated.[140] When COF-43 was immersed in tetrahydrofuran (THF), trichloromethane ($CHCl_3$), toluene, and methanol, it did not change its original diffraction patterns, whereas its exposure to dioxane, H_2O, and DMF led to the loss of crystallinity as judged from PXRD patterns.

3576 | *Chem. Soc. Rev.*, 2020, **49**, 3565–3604

This journal is © The Royal Society of Chemistry 2020

The authors speculated that the loss of crystallinity might be attributed to the exfoliation of bulk COF-43 rather than breaking of its covalent linkages. The hydrolysis of COF-43 was excluded by solid and solution-state infrared spectroscopy (IR) measurements, demonstrating that COF-43 possessed good chemical stability in each solvent. The atomic force microscope (AFM) images of the suspensions sonicated in different solvent systems further confirmed the exfoliation behavior. When combined with dynamic light scattering (DLS), it was observed that there were significant size differences between the dispersed species in the different solvent systems. When COF-43 was sonicated in dioxane, high aspect ratio platelets with a width of 200 nm were achieved with a height of 1.32 ± 0.37 nm (related to 3–5 layers). Thin sheets with a height of 3.3 Å (bi-/single-layered) were realized after sonicating in H_2O while much thicker sheets were obtained after deposition from non-exfoliating solvents, such as THF. These observations suggested that dispersing COF-43 in exfoliating solvents led to high aspect ratio platelets.

Secondly, the design of skeletons is another crucial factor that can influence the exfoliation products. The introduction of flexible building units into the skeleton of COFs can weaken the π–π interactions and make them easily exfoliated to nanosheets. Two C_{3v}-symmetric flexible building units were used to form an [3+3] imine-linked COF, TPA-COF (Fig. 9a), which possessed a layered hexagonal structure with an interlayer distance of 4.1 Å and could be easily transformed to nanosheets by exfoliation.[141] In a typical process, bulk TPA-COF was dispersed in 150 mL of ethanol and sonicated for 3 h. After sedimentation for 24 h, the upper colloidal suspension was collected and then centrifuged at 7000 rpm for 5 min, resulting in TPA-COF NSs with a thickness of 3.5 ± 0.3 nm (Fig. 9d). Notably, the fine crystallinity of the nanosheets was revealed by low-dose HRTEM (Fig. 9b). The arranged hexagonal

structures were observed in the denoised HRTEM image, matching well the simulated one (Fig. 9c).

A temperature-swing gas exfoliation approach also transforms bulk COFs to NSs in liquid.[142] Three azine-/imine-linked 2D COFs, NUS 30–32, were exfoliated by using this method. First, the bulk powder was heated to 300 °C for 10 min in air, and then immersed into liquid N_2 quickly (Fig. 9e). These procedures were repeated 5 times, and large particles were removed by centrifuging the suspension at 3500 rpm for 10 min. The supernatant containing NSs was further collected and centrifuged at 8000 rpm for 10 min to remove bulk particles. The micrometer-sized CONs with a thickness around 2–4 nm were observed by AFM and transmission electron microscopy (TEM). The authors suggested that the interlayer distance was expanded during the heating processes, allowing the gasified liquid N_2 to exfoliate the layered structure.

2.2.3 Self-exfoliation. Different from the exfoliation with external forces, the self-exfoliation approach tends to delaminate by internal forces introduced from the inbuilt ionic character. Several ionic COFs (iCOFs) with charged centers are exfoliated in solvents *via* self-exfoliation.[150–154] For instance, a guanidinium halide-based 2D iCOF ($TpTG_{Cl}$) in an eclipsed mode with Cl^- counter anions inserted in two monomer units (~ 3.3 Å) was prepared. After immersing the powder in an aqueous medium, the $TpTG_{Cl}$ layers were exfoliated into nanosheets spontaneously since the interlayer distance was increased to ~ 5.5–6 Å in contrast to the initial distance of 3.338 Å.[150] It is attributed to the fact that the π–π interactions between the adjacent layers were significantly weakened by electrostatic repulsion originated from the loosely bound chloride ions and positively charged guanidinium building units. The micrometer to sub-micrometer sized sheets with a height profile of 2–5 nm were observed by TEM and AFM. To prove that the self-exfoliation mechanism was closely connected with COF's ionic skeleton, the positively
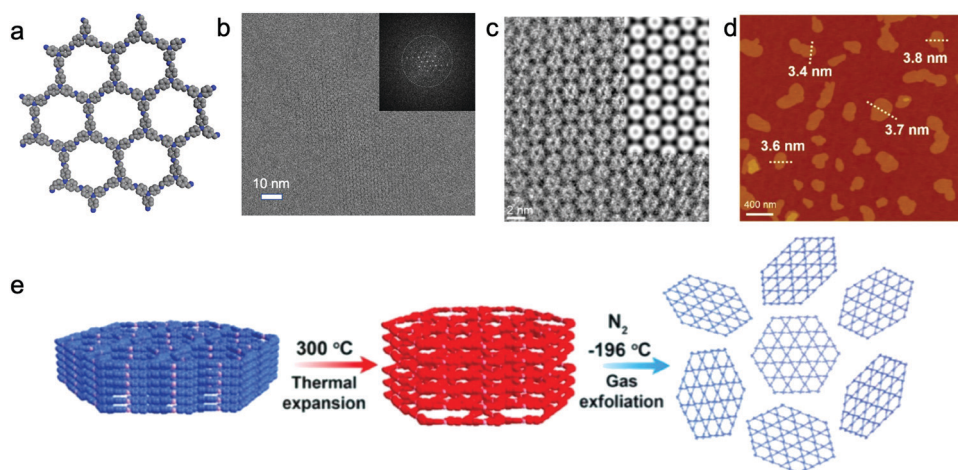
Fig. 9 (a) Schematic of TPA-COF. (b) High-resolution TEM image of a typical TPA-COF NS with the low-dose technique using a direct-detection electron-counting camera. Inset: FFT of the TPA-COF NS. (c) Denoised HRTEM image, and the inset image is the simulated HRTEM image. (d) AFM image of TPA-COF nanosheets. Reproduced from ref. 141 with permission from American Chemical Society, copyright 2017. (e) Schematic illustration of the exfoliation of NUS-30 by the temperature-swing gas method. Reproduced from ref. 142 with permission from the Royal Society of Chemistry, copyright 2019.

This journal is © The Royal Society of Chemistry 2020

Chem. Soc. Rev., 2020, **49**, 3565–3604 | **3577**
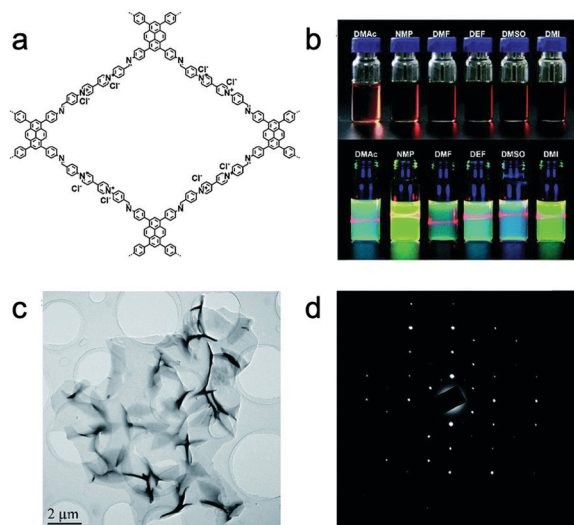
Fig. 10 (a) Schematic of PyVg-COF. (b) Photos represent PyVg-COF dispersed in various solvents. Top, under sunlight; bottom, under 365 nm UV light. (c) Low magnification TEM image of PyVg-COF nanosheets. (d) SAED of the PyVg-COF nanosheet. Reproduced from ref. 155 with permission from the Royal Society of Chemistry, copyright 2019.

charged guanidinium units were replaced by a neutral ligand and no sheet-like products were observed by TEM. Besides, the mechanically grinding method was expected to exfoliate as-synthesized TpTG$_{Cl}$, but there was no significant change in PXRD patterns as well.

The behavior of self-exfoliation in different solvents was also investigated. PyVg-COF (Fig. 10a) was synthesized combining two building blocks with opposing properties.[155] One of the monomers (4,4′,4″,4‴-(pyrene-1,3,6,8-tetrayl)tetraaniline, Py (57)) tends to form crystalline stacks with strong π–π interactions; the other one (1,1-bis(4-formylphenyl)-4,4′-bipyridinium dichloride, Vg^{2+}·2Cl^{-} (13)) with inherently high charge density exhibits strong electrostatic repulsion upon stacking. The large-area monolayer or multilayer nanosheets were achieved after immersing PyVg-COF in various organic solvents, showing an obvious Tyndall effect (Fig. 10b). The HRTEM image and selected area electron diffraction (SAED) pattern revealed the micro-scaled size and high crystallinity of NSs, respectively (Fig. 10c and d). The self-exfoliation behavior appeared when attaining a higher skeleton–solvent interaction absolute value, that is, the successful self-exfoliation of PyVg-COF only happens when the skeleton–solvent interactions are higher than the interlayer interactions of the skeletons.

2.2.4 Chemical exfoliation. The chemical exfoliation method is highly efficient to prepare COF NSs by introducing intercalated molecules or groups to reduce the interlayer interactions.[156–160] An anthracene-based COF (DaTp) was exfoliated chemically by post-synthetic modification of anthracene moieties with *N*-hexylmaleimide molecules through Diels–Alder cycloaddition reaction.[156] The resultant NSs showed a sub-micrometer sized and ribbon-like morphology with a thickness of around 17 nm. The reduction of the interlayer interaction was evidenced by a model reaction, where

the planarity of the anthracene moiety in the cycloaddition product distorted from 180° to 107°. The NSs were assembled layer-by-layer in the air–water interface to cast a scalable thin film of DaTp-CONs, leading to a self-standing and semi-transparent COF thin film with 1 cm in diameter.

In addition, a 2D porphyrin-containing COF (DhaTph) was delaminated by introducing disruptions between the layers, which was implemented through coordinating the porphyrin centers with axial ligands.[157] The NSs with a width of several hundred nanometers and a thickness of around 3 nm were obtained by refluxing DhaTph in pyridine solutions for 20 h.

Notably, Dichtel *et al.* presented a strategy to exfoliate 2D imine-linked COFs by acid. For example, the addition of excess trifluoroacetic acid (TFA) could temporarily protonate BND-TFB COF's imine linkages and lead to a disordered stacking, which minimized the electrostatic repulsion between adjacent sheets and further promoted exfoliation. The exfoliated NSs with the thickness ranging from 5 to 50 nm were capable of being dispersed in organic solvents. The retained imine-linked network, uniform six-fold symmetry, and well-matched diffraction peak (100 plane) were demonstrated by FT-IR, HRTEM, and FFT (fast Fourier transform), respectively.[161]

3 Electrochemical energy storage

3.1 Batteries

A battery is an energy storage device consisting of cathode, anode, electrolyte, and separator. The cathode and anode communicate with electrons under a potential difference, and thus the electrochemical energy is stored or released in the batteries. To prevent short circuits, a porous membrane as a separator is placed between cathode and anode to insulate electrons but allow ions to move across. At the same time, liquid or solid electrolytes with high ionic conductivity are employed to facilitate ion transport. Currently, the capacity, rate performance, and lifetime of electrode materials still cannot fulfill the demand of matching the supply and releasing energy anytime and anywhere; liquid electrolytes suffer from safety risk while solid electrolytes show low ion conductivity. As a highly porous crystalline polymer, COFs are capable of storing numerous ions and their inner surfaces can be metrically modified with redox-active sites.[162,163] Thus, COFs are potential materials as battery electrodes. Besides, their electrical insulation nature and open channels make COFs an attractive option in solid electrolytes and separators.

3.1.1 Cathode. COFs can provide abundant redox-active sites to directly participate in multi-electron redox reactions *via* reversible chemical bonding and can be also used as hosts to accommodate other redox-active materials for fabricating cathode composites.

3.1.1.1 COFs as redox-active cathodes. Conventional electrode materials are dominated by inorganic materials such as transition metal oxides or phosphates (*e.g.*, LiCoO$_2$, LiMn$_2$O$_4$, and LiFePO$_4$). Organic molecules as electrodes have been developed recently for their environmental benignity, adjustable theoretical

3578 | *Chem. Soc. Rev.*, 2020, **49**, 3565–3604

This journal is © The Royal Society of Chemistry 2020

capacity, and redox potential. However, their high capacity is generally accompanied with an inferior cyclic performance at high rates due to their partial dissolubility in the electrolyte and poor conductivity. Besides the merits from organic materials, highly crosslinked COFs exhibit high stability and are almost non-soluble in any solvent, and specifically, 2D COFs theoretically possess high charge carrier (electron and/or hole) conductivity in planar layers through π-conjugation as well as across the stacking sheets *via* overlapped π electrons. Moreover, few-layered 2D COFs are beneficial for ionic/electronic diffusion and are able to deliver a high rate capability.

For instance, 1,3,5-triformylphloroglucinol (Tp) (24) showed a capacity below 30 mA h g^{-1} and couldn't be fully recharged during cycling. 2,7-Bis((E)-benzylideneamino)benzo[*lmn*][3,8]-phenanthroline-1,3,6,8(2H,7H)-tetraone (DANTB) (69) delivered an initial capacity of 125 mA h g^{-1}, and then, the capacity decreased rapidly within 10 cycles. In sharp contrast, on incorporating these redox-active groups into a Schiff-base COF (Tp-DANT-COF), it displayed a capacity of 78.9 mA h g^{-1} at the current density of 1.5C (corresponding to 200 mA g^{-1}) and retained the capacity for more than 200 cycles.[164] It demonstrated the importance of robust networks. In addition, when the monomer Tp is replaced by 1,3,5-triformylbenzene (Tb) (23), the resultant Tb-DANT-COF exhibited lower voltage hysteresis and higher initial discharge capacity.

Despite the fact COFs exhibit high conductivity in and between the layers theoretically, the battery performance still suffers from their limited electron and ion conductivity. The reasons for this are (1) the defects and boundaries between particles greatly hinder the electron transport; (2) the 2D COF sheets tend to be packed closely in an eclipsed fashion due to strong π–π interactions, leading to difficulty in the diffusion of ions to the interior active sites through the long transportation paths even at a high current density.[137,165]

The electron conductivity can be enhanced by integrating COFs with conductive materials such as carbon nanotubes (CNTs) or graphene.[166–169] Jiang *et al.*[167] presented a strategy for improving the electron mobility *via* growing redox-active COFs on CNTs (D$_{TP}$-A$_{NDI}$-COF@CNTs). The capacity of D$_{TP}$-A$_{NDI}$-COF@CNTs was retained at 74 mA h g^{-1} after 700 cycles, corresponding to 90% utilization efficiency of the redox-active sites, and with a stable Coulombic efficiency reaching 100%.

Feng and Wang *et al.* proposed a strategy to reduce the ion/electron migration length and accelerate the ionic/electronic diffusion by exfoliating bulk COF materials into few-layered NSs with more accessible functional sites.[137] An anthraquinone-based COF (DAAQ-TFP-COF) (Fig. 11a) was successfully exfoliated to ultrathin NSs with a thickness of 5 nm *via* ball milling (donated as DAAQ-ECOF) (Fig. 11c). The Li$^+$ ion diffusion coefficient of DAAQ-ECOF is 6.94×10^{-11} cm^2 s^{-1}, which is three times higher than that of DAAQ-TFP-COF and higher than those of conventional inorganic materials. The electrochemical process of bulk DAAQ-TFP-COF was dominated by ion-diffusion, whereas that of DAAQ-ECOF got rid of the ion-diffusion restriction and was controlled by electron transport. Accelerated Li$^+$ transport and shortened diffusion paths resulted in good battery
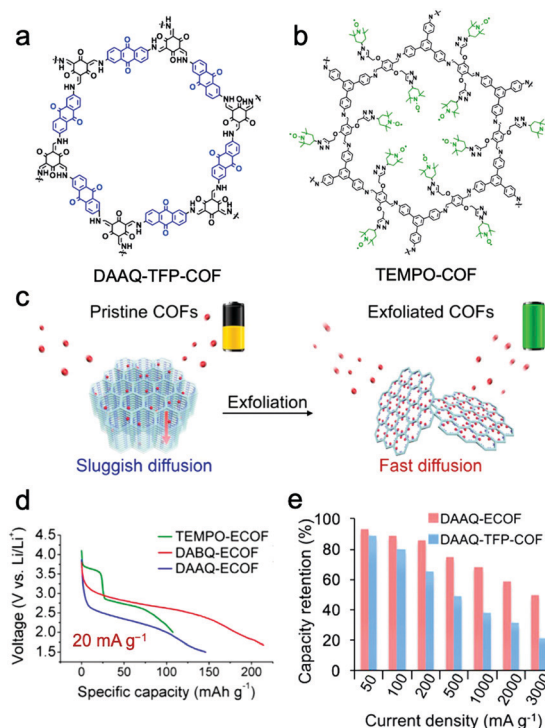

Fig. 11 Chemical structures of DAAQ-TFP-COF (a) and TEMPO-COF (b). (c) Schematic representation of the exfoliated 2D redox-active COFs as cathodes for LIBs; (d) discharge curves; (e) capacity retention. Reproduced from ref. 137 with permission from American Chemical Society, copyright 2017.

performance. DAAQ-ECOF presented a capacity of 145 mA h g^{-1} at 20 mA g^{-1} over more than 70 cycles, delivering 96% of its theoretical capacity, while only 73% was retained for pristine DAAQ-TFP-COF (Fig. 11e). At a current density of 500 mA g^{-1}, DAAQ-ECOF also exhibited a capacity retention of 98% (107 mA h g^{-1}) after 1800 cycles. Attractively, by introducing benzoquinone building units or attaching 2,2,6,6-tetramethylpiperidine-1-oxyl (TEMPO) functional groups (Fig. 11b) *via* molecular design, the capacity could be increased to 210 mA h g^{-1} and the discharge voltage could be increased to 3.6 V (Fig. 11d).

3.1.1.2 COFs as the host for phase-changing components. COFs can be considered as promising hosts for phase changing cathodes. Phase changing cathodes during charge and discharge processes involve chemical bond breaking and recombining as well as multiple phase transitions.[3] The theoretical capacities of the phase changing cathodes are generally high because these reactions usually involve multi-electron transfer.

Taking lithium–sulfur batteries (LSBs) as an example, they are typical multi-electron transfer reaction systems with a high theoretical capacity of 1675 mA h g^{-1}. Although LSBs are considered as one of the most promising candidates for next-generation batteries due to their exceptional theoretical capacity, low cost, and natural abundance, there are several drawbacks hindering their development: (1) element sulfur will produce large volume fluctuation (about 80%) during charge and discharge owing to the huge density mismatch between

This journal is © The Royal Society of Chemistry 2020

Chem. Soc. Rev., 2020, **49**, 3565–3604 | **3579**

sulfur and final products, Li_2S; (2) the insulating nature of sulfur and Li_2S_2/Li_2S will influence electrochemical kinetics; (3) the intermediates (lithium polysulfides (PSs)) during operation are soluble and migrate freely between cathode and anode, leading to a "shuttle effect" and rapid capacity fading.[170–172] COFs are suitable for LSBs for the following reasons: (1) the accessible cavities and adjustable apertures can be designed to accommodate volume changes and limit the migration of PSs; (2) the electronic interactions between the layers in 2D COFs can facilitate the transportation of electrons and ions; (3) the interior of pores can be introduced with specific functionalities to bind the soluble intermediates; (4) COFs consist of strong covalent linkages, which provide favorable thermal and chemical stability. Several efforts have been devoted to illustrating COFs as suitable hosts to encapsulate sulfur species.[173–181]

CTF-1 was the first COF used as the sulfur host for LSBs.[173] It possessed a surface area of 789 m^2 g^{-1} with a pore size of 1.23 nm. The composite CTF-1/S@155 °C was prepared by a melt-diffusion strategy with a sulfur loading of 34 wt%, which showed a discharge capacity of 1197 mA h g^{-1} at the 2nd cycle and maintained at 762 mA h g^{-1} after 50 cycles at 0.1C.

The sulfur loading is an important parameter, which can influence the electrochemical performance. A porphyrin-based COF (Por-COF) loaded with 55 wt% sulfur gave a capacity of 929 mA h g^{-1} at the 2nd cycle and held a capacity of 633 mA h g^{-1} after 200 cycles at 0.5C.[174] Another porphyrin-based COF (Py-COF) with 70 wt% sulfur loading delivered a capacity of 963.4 mA h g^{-1} after 100 cycles at 1.0C.[175]

Compared with N-doped porous organic polymers, doping positively polarized elements or introducing active groups that can react with sulfur can trap PSs more efficiently, such as elemental B, fluorinated groups, or vinyl groups.[176,177,179,180] Tang and Li et al. presented a boronate ester COF (COF-1) as the sulfur host for trapping PSs (Fig. 12a).[176] With a sulfur loading of 40%, COF-1/S delivered an outstanding initial capacity up to 1628 mA h g^{-1}, and a capacity of 929 mA h g^{-1} was achieved after 100 cycles at 0.2C. CTF-1 was selected for comparison because it had a similar pore size but a different pore surface environment. The calculated adsorption energy between Li^+ ions with COF-1 and CTF-1 was similar, while that for linear S_8^{2-} in COF-1 and CTF-1 delivered quite different values: 34 kcal mol^{-1} for COF-1 and 24 kcal mol^{-1} for CTF-1 (Fig. 12b). These differences suggested that COF-1 can trap S_x^{2-} species more effectively, which may be attributed to the more positively polarized pore surface because of the electron-deficient B atoms in COF-1.

The COF-derived material is another alternative to increase the conductivity of the composite cathode and hence improve its electrochemical performance.[177,178] A boron/oxygen co-doped porous carbon (BOC) host material (BOC@CNT) was prepared by carbonizing the COF-10@CNT composite. BOC@CNT/S had a sulfur loading of 68.5% and exhibited an outstanding reversible capacity of 1077 mA h g^{-1} after 200 cycles at 0.2C, and 794 mA h g^{-1} after 500 cycles at 1C.[177]

Tables 1 and 2 summarize the electrochemical performances of COFs as redox-active materials or as hosts for
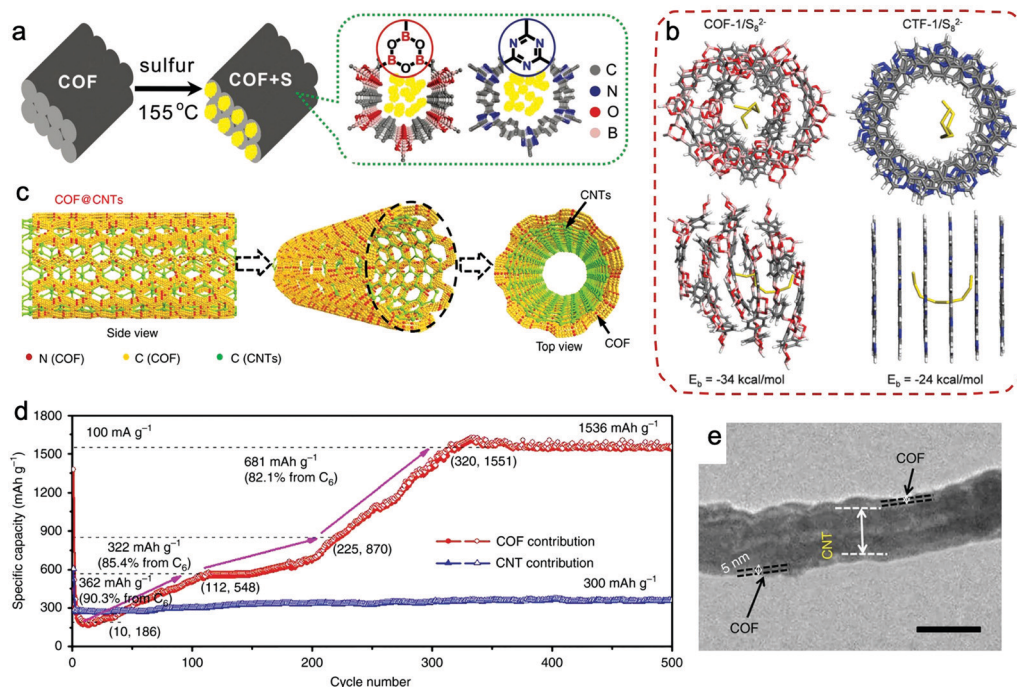
Fig. 12 (a) Graphical representation of the synthesis of COF/S composites. (b) The adsorption energy for S_8^{2-} anions in the pores of COF-1 and CTF-1, calculated by quantum mechanics/molecular mechanics. Reproduced from ref. 176 with permission from Wiley-VCH Verlag GmbH & Co. KGaA, copyright 2016. (c) Schematic of COF@CNTs showing CNTs covered with a few COF layers. (d) COF's capacity contribution calculated based on its mass in COF@CNTs at 100 mA g^{-1} during the charge/discharge process. (e) TEM image of COF@CNTs with a scale bar of 100 nm. Reproduced from ref. 189 with permission from Nature Publishing Group, copyright 2018.

3580 | Chem. Soc. Rev., 2020, 49, 3565–3604

This journal is © The Royal Society of Chemistry 2020

Table 1 COFs as redox-active cathodes

	Capacity (CC/DC/CD)	Cycling performance (RC/CD/CN)	Voltage range (vs. Li/Li$^+$)	Ref.
PIBN-G	—/271.0/28	208.1/280/300	1.5–3.5	168
NT-COF	—/124/20	—/20/100	1.5–4.0	165
2D CCP-HATN	—/62.5/11.7	—/—/—	1.2–3.9	166
2D CCP-HATN@CNT	—/116/11.7	—/58.5/1000		
PI-ECOF-1	—/112/14.2	72/14.2/300	1.5–3.5	193
PI-ECOF-1/rGO50	—/167/14.2	—/142/300		
2D-PAI@CNT	—/104.4/100	—/500/8000	1.5–3.5	169
2D-PAI	—/28.5/100	—/—/—		
DAAQ-ECOF	—/145/20	107/500/1800	1.5–4.0	137
DABQ-ECOF	—/210/20	—/—/—		
TEMPO-ECOF	—/115/20	—/—/—		
DTP-ANDI-COF	—/42/200	—/—/—	1.5–3.5	167
DTP-ANDI-COF@CNTs	—/74/200	67/200/700		
Tp-DANT-COF	78.9/93.4/200	71.7/1000/600	1.5–4.0	164
Tb-DANT-COF	135.4/144.4/50	80.1/500/300		
PPTODB	—/198/20	135.2/20/150	1.5–3.5	194
DAAQ-TFP	—/—/78.5	53.5/157/500	1.4–3.6	195
DAPH-TFP	—/96.2/85.5	81.7/171/500		
PEDOT@DAAQ-TFP	—/—/78.5	59.8/157/500		
PEDOT@DAPH-TFP	—/99.2/85.5	93.2/171/500		

Note: CC: charge capacity (mA h g^{-1}), DC: discharge capacity (mA h g^{-1}), CD: current density (mA g^{-1}), RC: reversible capacity (mA h g^{-1}), CN: cycle number.

Table 2 COFs as the host for the phase-changing component for cathodes

	Loading (ML/PL)	Capacity (CC/DC/CD)	Cycling performance (RC/CD/CN)	Voltage range (vs. Li/Li$^+$)	Ref.
CTF-1/S@155 °C	—/34	1304/1497/168	762/168/50	1.1–3.0	166
S/Azo-COF	—/39	—/1536/167.2	741/167.2/100	1.5–2.8	196
COF-F-S	0.5/60	—/1120/167.2	645/167.2/100	1.7–2.8	180
S/TpPa-COF@MWCNTs	1–2/—	—/1242.2/83.6	526.5/836/450	1.6–2.8	197
S@TFPPy-ETTA-COF	—/—	—/723/167.2	—/167.2/130	1.7–2.8	181
poly-sulfide@TFPPy-ETTA-COF	—/—	—/1069/167.2	—/167.2/130		
Por-COF/S	1.8/55	—/1166/840	633/840/200	1.8–2.7	174
Py-COF/S	0.8–1.2/70	—/1145/836	877.2/3344/200	1.8–2.7	175
S-COF-V	—/67	—/1400/335	959/335/100	1.7–2.8	179
COF-F-SeS$_2$	1.2/40	—/1703/167.2	970/167.2/100	1.7–2.8	198
COF-1/S	—/40	—/1628/334.4	770/836/200	1.5–3.0	176
TAPB-PDA-COF/S	—/60	—/1357/200	705/200/210	1.8–2.8	199
HCPT@COF/S	—/69.3	—/1224/334.4	1053/334.4/300	1.7–2.8	200
Carbonized COFs					
BOC@CNT/S	3.5/—	—/1434/334.4	797/1672/500	1.7–2.8	177

Note: ML: mass loading (mg cm^{-2}), PL: percentage loading (%), DC: discharge capacity (mA h g^{-1}), CD: current density (C), RC: reversible capacity (mA h g^{-1}), CN: cycle number

phase-changing components used in cathodes, respectively. The COF-based cathodes possessed high capacity (up to ∼200 mA h g^{-1}) and good cycling performance, which were comparable or even better than those of the commercialized cathodes (e.g., LiPFeO$_4$, capacity of about 150 mA h g^{-1} in practice). However, due to the lack of investigations of COF-based cathodes in full cells these evaluations are not very appropriate and further efforts are still needed.

3.1.2 Anode. Two mechanisms are involved in the charge–discharge process of COF-based anodes in Li$^+$/Na$^+$/K$^+$ batteries: (1) ion insertion/deinsertion in the 2D COFs with layered graphite-like structures and rich ion transport channels; (2) redox reactions on the skeletons of COFs.[121,182,184–192] Similar to the COFs used in cathodes, the COF NSs provide shortened ion/electron transport paths and accelerated conductivity, leading to the sufficient utilization of active sites.

A COF denoted as IISERP-CON1 and incorporated with the triazole moiety was grown into self-exfoliated COF NSs and further used as the anode in lithium-ion batteries (LIBs).[184] A reversible intercalation mechanism was proposed due to the following reasons: its electrochemical behavior did not show obvious redox peaks during cycling; based on computational studies, the distance between lithium and the ring nitrogen atoms of the triazole or the hydroxyl oxygens of the phloro-glucinol was longer than the Li–N or Li–O distance; IR, PXRD, X-ray photoelectron spectroscopy (XPS) and ^{1}H nuclear magnetic resonance (^{1}H-NMR) characterization demonstrated the weak interaction between lithium ion and COF. A capacity of 720 mA h g^{-1} at 100 mA g^{-1} over 100 cycles was achieved and a capacity of over 500 mA h g^{-1} at 500 mA g^{-1} after 1000 cycles was retained. Such a good cycling performance was attributed to the mildly reversible interaction between lithium and

This journal is © The Royal Society of Chemistry 2020

Chem. Soc. Rev., 2020, **49**, 3565–3604 | **3581**

IISERP-CON1. Wang et al.[121] reported a few-layered structure of COF-10@CNT used in potassium ion batteries. The exposed active sites attributing to the few-layered structure facilitated the intercalation of K$^+$, which was based on the π-cation interaction between K$^+$ and conjugated π-electrons of benzene rings. Thus, an impressive reversible capacity of 288 mA h g^{-1} after 500 cycles at 0.1 A g^{-1} and 161 mA h g^{-1} after 4000 cycles at 1 A g^{-1} was obtained.

For achieving higher capacity, introducing more redox-active sites in the backbones of COFs is desired. A few-layered 2D imine-based COF fixed by carbon nanotubes was achieved and used as the anode in LIBs (Fig. 12c).[189] The CNTs were covered by thin COF layers with a thickness of about 5 nm (Fig. 12e). Interestingly, the capacity of COF@CNTs gradually increased from 362 to 1536 mA h g^{-1} at 100 mA g^{-1} after 320 cycles (Fig. 12d). The activation process and high capacity were attributed to (1) the 14-electron redox mechanism involving the reaction between Li$^+$ ion and COF skeleton (one Li$^+$ per C=N linkage and six Li$^+$ per benzene ring); (2) the expansion of the interlamellar space in COFs by ion insertion during the lithiation/delithiation process.

Besides, the formation and transformation of radical intermediates during the lithiation/delithiation process were observed. Moreover, stabilizing the radical intermediates is an efficient method to improve electrochemical performance.[188,192] β-Ketoenamine linked DAAQ-COF was employed as the anode in sodium-ion batteries (SIBs) and it resulted in C–O$^•$ and α-C radical intermediates upon charging and discharging.[188] It was found that reducing the thickness of COFs could promote the stability of radical intermediates as well as their contributive capacity, owing to the restriction of interlayer electron self-exchange behavior and the increase of available active sites. The COF with a thickness of 4–12 nm exhibited a high capacity of 420 mA h g^{-1} at 100 mA g^{-1} and outstanding cycling stability with 99% capacity retention over 10 000 cycles at 5 A g^{-1}.

Despite the fact that very high capacity (>1500 mA h g^{-1}) can be achieved by using COF-based anodes, their high voltage, long activation process, and high cost are still greatly limiting their real application.

3.1.3 Electrolyte and separator. Ionic transportation is a critical process of battery operation that associates the internal circuit between the electrodes and avoids short circuits caused by electronic transport. High ionic conductivity (δ_i) and transference number (t^+) of working ions (e.g., Li$^+$, H$^+$, Na$^+$) are required for the electrolyte component.

3.1.3.1 Solid electrolyte. Since liquid electrolytes suffer from serious safety issues including electrolyte leakage, flammability, and dendrite formation, solid electrolytes have been considered with great interest.[11,40,201,202] However, the processability and mechanical strength of inorganic electrolytes and the ionic conductivity of polymeric solid electrolytes still cannot fulfill the demands for practical application. For example, poly(ethylene oxide) (PEO) has been accepted as a promising candidate for solid state electrolytes in the past few years, but its further application has been hindered by limited ionic conductivity (ionic conductivity can up to 10^{-4} S cm^{-1} under 65–78 °C) and generally a low t^+ value. Regarding inorganic ceramic materials (e.g., Al$_2$O$_3$ and Li$_7$La$_3$Zr$_2$O$_{12}$), although they have been widely studied owing to their outstanding conductivity (ionic conductivity ranges from 10^{-5} to 10^{-3} S cm^{-1} at room temperature), the poor machinability and the often instability at electrodes limit their practical application.

The basic mechanism for Li$^+$ ion transport is the Grotthuss (hopping) mechanism, in which the ion can hop from sites to sites. COFs may provide the following opportunities: (1) open channels and well-defined pore structures create directional ion conduction pathways; (2) hopping ability is promoted by introducing functional groups and/or guest molecules with hopping sites for ions; (3) versatile structural design features the selective adsorption of counter ions, which can facilitate the migration of target ions.[61,153,203–210]

There are two effective strategies to increase Li-ion conductivity: (1) building an ionic skeleton to facilitate the dissociation of ion pairs and promote target ionic migration; (2) introducing soft and flexible building units or polymer chains in the framework to increase hopping sites.

Feng et al. successfully prepared an anionic 3D COF (CD-COF-Li) with Li$^+$ as the counterion by linking soft and flexible building blocks, and investigated its ion conduction behavior as a quasi-solid electrolyte.[203] With the encapsulation of a small amount of ethylene carbonate (EC)/dimethyl carbonate (DMC) and LiPF$_6$ in the channels, the resultant composite exhibited a conductivity of up to 2.7 × 10^{-3} S cm^{-1} at 30 °C with a low activation energy of 0.26 eV. Besides, the comparison between neutral framework and cationic/anionic framework was investigated for further demonstrating the promotion effect of the ionic framework.[61,153,205,208,209] It is worth mentioning that the organic solvents that can greatly increase ionic conductivity are inevitably used in the solid electrolyte fabrication process, but not all the works clearly clarify whether the solvent molecules are residual or not.

Poly(ethylene oxide) (PEG)-based polymers with oxygen atoms as Li$^+$ ion hopping sites are representative polymeric solid-state electrolytes; however, the existence of the crystalline area restricts their chain oscillation and ion conduction ability. Anchoring oligo(ethylene oxide) chains to the pore walls or accommodating PEG in COFs provides chances to suppress the oxyalkyl chain crystallization and accelerate ion conduction in the channels.[204–207] A polyelectrolyte COF, TPB-BMTP-COF, was loaded with LiClO$_4$ through a solution diffusion method.[204] The Li-ion conductivity of Li$^+$@TPB-BMTP-COF was up to 1.66 × 10^{-4} S cm^{-1} at 80 °C, which is 30 times and 731 times higher than that of Li$^+$@TPB-DMTP-COF (methoxy groups on the edge phenyl units) and Li$^+$@TPB-TP-COF (bare pore walls), respectively. Li$^+$@TPB-BMTP-COF possessed the lowest activation energy of 0.87 eV among these three electrolytes. The obviously increased conductivity and decreased activation energy of Li$^+$@TPB-BMTP-COF could be attributed to the advantage that the covalently bonded dense oligo(ethylene oxide) chains can complex with lithium ions and form a polyelectrolyte interface in the channels, thus accelerating the dissociation of the ionic compounds and facilitating the ion hopping for Li-ion transport between the neighboring hopping sites.
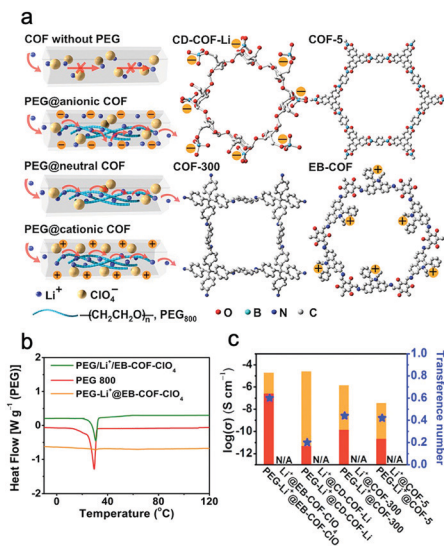
3582 | Chem. Soc. Rev., 2020, 49, 3565–3604

This journal is © The Royal Society of Chemistry 2020

Fig. 13 (a) Schematic for Li$^+$ transport in neutral or ionic COFs, and chemical structures of CD-COF, COF-5, COF-300, and EB-COF. (b) DSC curves of PEG, PEG-Li$^+$@EB-COF-ClO$_4$, and PEG/Li$^+$/EB-COF-ClO$_4$ (mechanical mixture sample). (c) The contribution of Li$^+$ conduction (red area) and anion conduction (orange area). Reproduced from ref. 205 with permission from American Chemical Society, copyright 2019.

Without the complex monomer synthetic procedure, Feng and Wang *et al.* directly encapsulated low-molecular-weight polyethylene glycol (PEG, M_w = 800) and lithium salt into the channels of COFs to prepare all-solid-state electrolytes without any solvent residue (Fig. 13a).[205] The results showed that PEG in the confined space can indeed significantly boost the ion conduction rate by orders of magnitude. PEG-Li$^+$@EB-COF-ClO$_4$ showed a high ion conductivity, reaching 1.78×10^{-3} S cm^{-1} at 120 °C. Interestingly, PEG 800 has a phase transition from the elastic to viscous state at around 30 °C, but after the incorporation of PEG into the channels, the differential scanning calorimetry (DSC) curve did not show any endothermic/exothermic peaks from −10 to 120 °C. It indicated a possibility that the incorporation of PEG chains in the channels could inhibit the formation of crystalline regions of PEG, and endowed a wide operating temperature range (Fig. 13b).

Notably, t^+ is another important factor for electrolytes that depends on the proportion of the target ions to the total ions carried through the electrolyte. During the charge–discharge process, Li$^+$ and its counter anions migrate oppositely, while anions are blocked by the anode and accumulated on it. The accumulation of anions leads to a concentration gradient and polarization problem, which will cause increased internal impedance and the occurrence of inevitable side reaction. Thus, improving the value of t^+ close to unity is important for cell performance.

Feng and Wang *et al.* chose two neutral COFs (COF-5, COF-300), a cationic COF (EB-COF-ClO$_4$), and an anionic COF (CD-COF-Li) with the inclusion of PEG and LiClO$_4$ to explore their t^+ (Fig. 13a).[205] Among these four PEG-included COFs, PEG-Li$^+$@EB-COF-ClO$_4$ showed the highest t^+ of 0.60, while PEG-Li$^+$@CD-COF-Li only possessed a low t^+ of 0.2 (Fig. 13c).

It is attributed to the anionic skeleton that can fix Li$^+$ to restrain its mobility, but the cationic skeleton can trap anions and promote Li$^+$ migration. To further improve t^+, a single-ion conducting strategy was provided. Lee and Zhang *et al.* reported a series of crystalline imidazolate-containing diamine (1-H, 1-CH$_3$, 1-CF$_3$) iCOFs (Li-ImCOFs) as quasi-solid electrolytes.[208] Ion conductivities of 7.2×10^{-3}, 5.3×10^{-3}, and 8.0×10^{-5} S cm^{-1} were achieved at room temperature for CF$_3$-Li-ImCOF, H-Li-ImCOF, and CH$_3$-Li-ImCOF (with ~20% propylene carbonate) with t^+ values of 0.81, 0.88, and 0.93, respectively. These high t^+ values are owing to the fact that, without further addition of Li salt, the anionic groups were fixed in COFs' skeleton and immobilized, thus providing higher Li$^+$ mobility. It is noted that the ion conductivity obtained *via* the single ion conducting strategy in all-solid-state electrolytes needs to be further improved.[209]

In addition to the Li$^+$ ion conduction, COFs can also serve as proton conductors in the proton exchange membrane fuel cells (PEMFCs).[211–219] Nafion-based electrolytes used as proton conductors are strongly dependent on humidity and are deactivated above 80 °C. The current strategies for developing COF-based proton conductors rely on encapsulating proton carriers in the channel,[212,213] constructing an ionic skeleton,[214] covalently decorating pendant acid groups, or combining a proton-conductive polymer to form a composite conductor.[215–217] Nitrogenous molecules (*e.g.*, imidazole molecules, pyridines), acidic molecules (*e.g.*, H$_3$PO$_4$, polyoxometalates), water molecules, and pendant sulfonic acid groups are usually considered as favorable proton carriers encapsulated in COFs' channels or fixed on the walls to enhance the integral proton conductivity.

Jiang *et al.* endowed TPB-DMTP-COF with high proton conductivity by loading proton carriers (triazole or imidazole) in it (Fig. 14a).[212] The im@TPB-DMTP-COF exhibited a conductivity of 4.37×10^{-3} S cm^{-1} at 130 °C with 155% imidazole loading. Besides, Li and Zang *et al.* applied ethidium bromide (EB) based cationic 2D COFs with a series of counterions (EB-COF:X, X = F, Cl, Br, I, and PW$_{12}$O$_{40}$$^{3-}$) for proton conductors.[214] Since hydrophilic PW$_{12}$O$_{40}$$^{3-}$ possesses a good water retention ability, it may attract water clusters and form interconnected hydrogen bonding networks throughout the channels. Therefore, EB-COF:PW$_{12}$ with an abundant proton pathway showed a proton conductivity of 3.32×10^{-3} S cm^{-1} under 97% RH at 25 °C.

Remarkably, COF-based proton conductors were applied to construct a PEMFC (Fig. 14b).[211,220] For example, the RT-COF-1AcB film prepared from 1,3,5-tris(4-aminophenyl)benzene (TAPB) (58) and 1,3,5-benzenetricarbaldehyde (BTCA) (23) possessed a proton conductivity of 5.25×10^{-4} S cm^{-1} at 313 K under 100% RH. When assembled in a PEMFC, it exhibited an optimal balanced performance with high conductivity (1.1×10^{-2} S cm^{-1} at 323 K) and low H$_2$ fuel crossover, leading to a maximum power density (12.95 mW cm^{-2}) and a maximum current density (53.1 mA cm^{-2}).

Up to now, the reported COFs and their composites could achieve a Li$^+$ conductivity of 10^{-3} S cm^{-1} at room temperature and a high ion transference number (>0.9). However, in most cases, COFs were pressed into pellets for the ion conduction
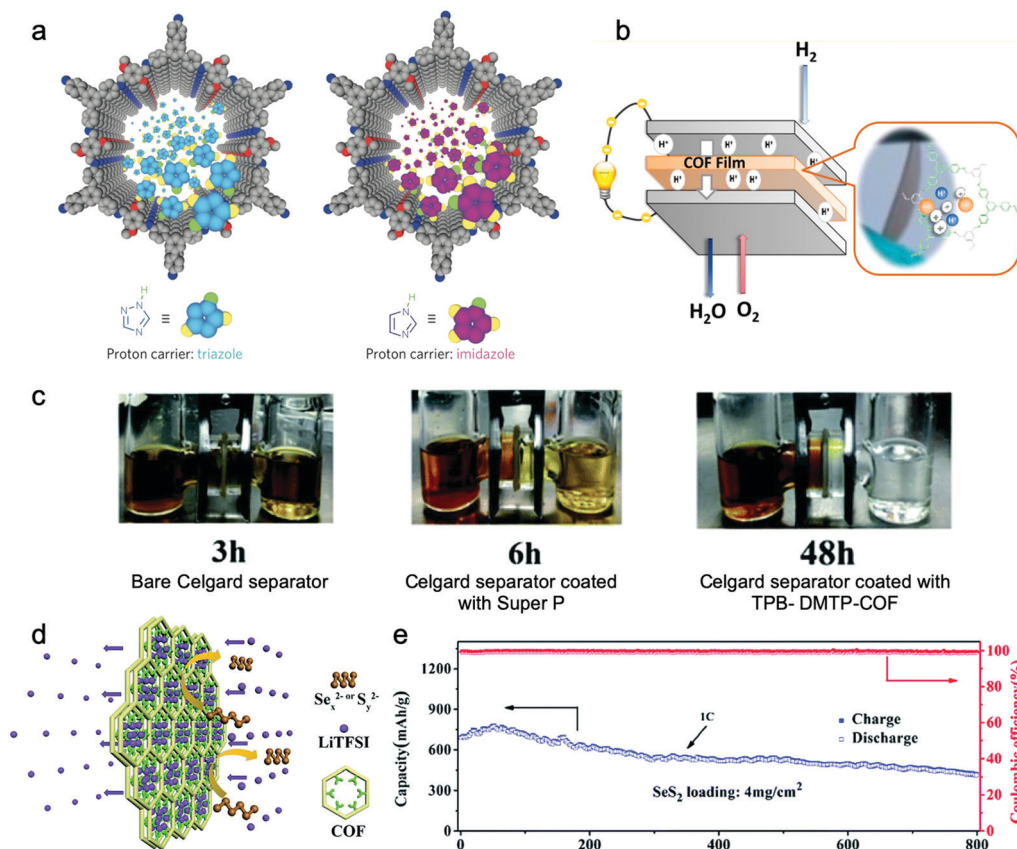
This journal is © The Royal Society of Chemistry 2020

Chem. Soc. Rev., 2020, 49, 3565–3604 | 3583

Fig. 14 (a) Schematic for proton carriers in COFs' channels. Reproduced from ref. 212 with permission from Nature Publishing Group, copyright 2016. (b) Schematic of the PEMFCs with COF films as membrane electrode assemblies (MEA). Reproduced from ref. 211 with permission from American Chemical Society, copyright 2017. (c) Visual experiments displaying permeation of polysulfides with different separators. (d) Schematic illustration of the usage of the TPB-DMTP-COF separator. (e) Cycling performance of the Li–SeS$_2$ cell with the TPB-DMTP-COF modified separator at 1C. Reproduced from ref. 222 with permission from the Royal Society of Chemistry, copyright 2019.

measurements. The ability to form self-standing films for COFs makes them good candidates as flexible solid-state electrolytes but this remains largely unexplored.

3.1.3.2 *Separator and interlayer.* As mentioned in Section 3.1.1.2, one of the most effective strategies to suppress the shuttle effect of phase-changing electrodes is to fabricate a composite electrode by impregnating redox-active components (*e.g.*, S and Se) in a porous host. Although this leads to a remarkable promotion in their electrochemical performance, the energy density is inevitably decreased because the host materials make up a mass percentage. To block the shuttle effect without sacrificing the redox-active component loadings in cathode composites, introducing a cation (*e.g.* Li$^+$ and Na$^+$) selective separator/interlayer between the electrodes that inhibits the passage of soluble intermediates (*e.g.*, PSs) is developed. Compared with the conventional materials used in interlayers/separators including polymers, graphene-based materials, carbon materials, and metal oxides, 2D COFs with pre-designable and well-defined channels in nanometer-scale are more beneficial for selective passage of cations.[221–224]

Wang and Hu *et al.* prepared a COF-rGO double-layer film by depositing dispersed COF-1 onto graphene through filtration and applied it as an ion-sieving separator in both organic sodium-ion batteries and Li–S batteries.[221] The cell assembled with the COF-rGO membrane showed an excellent initial capacity of 1386.9 mA h g^{-1} which slowly decreased to 1169.4 mA h g^{-1} after 50 cycles at 0.1C, while the capacity of the cells without an ionic sieve decreased from 869.9 mA h g^{-1} to 519.1 mA h g^{-1} after 50 cycles. Together with permeation measurements that demonstrated that the COF-rGO membrane could efficiently block the passage of polysulfides, these results proved that the improvement in the electrochemical performance was originated from the inhibition of the shuttle of polysulfides by the ionic sieve membrane.

Besides, a separator coated with TPB-DMTP-COF was proved to preferentially adsorb LiTFSI species into its cavities by strong hydrogen-bonding interactions, which created a narrower cavity size and further blocked the transportation of polysulfide/polyselenide species in the electrolyte and enhanced the Li$^+$ ion conductivity at the same time (Fig. 14d).[222] After separating the LiTFSI solution and LiTFSI/Li$_2$S$_6$ solution in the H-tube by the TPB-DMTP-COF-coated separator, the LiTFSI solution side remained colorless after 48 h, which indicated its effective inhibition for the transport of Li$_2$S$_6$ species (Fig. 14c). Meanwhile, a three-times increment in the lithium ion migration

3584 | *Chem. Soc. Rev.*, 2020, **49**, 3565–3604

This journal is © The Royal Society of Chemistry 2020

coefficient was achieved after using the TPB-DMTP-COF-coated separator. At a SeS_2 loading of 2 mg cm^{-2}, a specific capacity of 844.6 mA h g^{-1} was achieved at 0.5C. After increasing the SeS_2 loading to 4 mg cm^{-2}, a specific capacity of 684 mA h g^{-1} at 1C was achieved, and a capacity of 416.3 mA h g^{-1} was retained after 800 cycles (Fig. 14e).

Lee and Kwak *et al.* presented a strategy to construct a "microporous COF net on mesoporous CNT net" hybrid architecture and fabricated a self-standing film as the interlayer (NN interlayer) between sulfur cathode and separator to capture Li_2S_x.[223] Since the high conductivity and the hierarchical structure including mesopores and micropores of the NN interlayer were beneficial for electron and ion transportation as well as PS capture, the cell equipped with the NN interlayer exhibited a capacity retention of 84% after 300 cycles at 2.0C, but 15% for the cell without the interlayer.

3.2 Supercapacitor

Supercapacitors (SCs) possess high power density, high coulombic efficiency, long cycling life, and fast charge–discharge rate. Traditional SCs store electrical energy based on the surface charging mechanism through electrochemical double-layer capacitors (EDLCs) that attract anions and cations from the electrolyte to opposite electrodes' internal surfaces after applying an external electrical field. The capacity of EDLCs is related to the available surface sites of the electrode materials, where surface area, porosity, thickness of the double layer, dielectric constant, and ion species in the electrolyte all have impacts.[6,9] The representative electrode materials like porous carbon-based active materials for EDLCs have a high specific surface area, good chemical and electrical stability, and good conductivity. Another crucial class of supercapacitors based on reversible surface redox reactions, namely faradaic supercapacitors (FS) or pseudocapacitors, have shown at least an order of magnitude improvement in energy densities. The pseudocapacitance of the electrode materials strongly relies on the pore size and distribution, porosity, and redox-active species. Accordingly, combining the surface charging mechanism and the reversible surface redox reactions can significantly increase the energy density of supercapacitors. COFs with inherently large surface area (abundant adsorption sites), well-defined channels and long-range ordered arrangement (idealized ion transport pathways within the electrode–electrolyte interface), and redox-active building blocks (excellent redox activity) can contribute to both EDLCs and pseudocapacitors. COF-based SCs have been extensively developed in recent years. There are three ways for COFs to apply as electrodes in SCs: (1) synthesizing a redox-active skeleton by directly introducing or post-synthetically functionalizing with reversible redox response units; (2) constructing COF-based composites with conductive materials by inclusion or *in situ* polymerization of conductive polymers in their nanochannels to enhance both electrical conductivity and processability; (3) pyrolyzing COFs to form porous carbon materials to enhance conductivity and capacitance.

3.2.1 Pristine COF. 2D layered COFs provide continuous 1D channels as well as latticed π-columns, rendering them able to provide efficient electronic transport and rapid charge transfer to redox-active groups decorated on the walls.[225–232]

Although high charge carrier transportation rates are achieved in the nano-scaled region of 2D COFs with high periodicity, the electron conductivity of COFs is still limited due to the existence of disordered area and particle boundaries. Therefore, pristine COFs are usually mixed with or grown on conductive materials to afford SCs. The contribution of redox-active groups was illustrated by comparing DAAQ-TFP COF possessing reversible redox-active units 2,6-diaminoanthraquinone (DAAQ) (57) (S_{BET} = 435 m^2 g^{-1}) and DAB-TFP COF without redox-active groups (S_{BET} = 365 m^2 g^{-1}).[225] Not surprisingly, DAAQ-TFP COF provided a capacitance of 48 ± 10 F g^{-1} with a current density of 0.1 A g^{-1} and the capacitance remained at 40 ± 9 F g^{-1} after more than 5000 cycles, while DAB-TFP COF showed a double-layer capacitance behavior that delivered a lower capacitance of 15 ± 6 F g^{-1}. However, only 2.5% of the DAAQ moieties in DAAQ-TFP COF were utilized to participate in the electrode reaction, which may be attributed to the inferior conductivity originated from randomly oriented and polycrystalline DAAQ-TFP COF particles. Yang and Guo *et al.* presented that the conductivity of COFs could be improved by enhancing their nitrogen content. A triazine-based COF, PDC-MA-COF with a nitrogen content of 47.87%, showed an electronic conductivity of 3.34 × 10^{-2} S cm^{-1}.[227] The PDC-MA-COF exhibited a capacitance of 335 F g^{-1} at 1 A g^{-1} and approximately 19.71% triazine units were accessed during the electrochemical process.

An alternative approach to introducing redox-active groups to COFs is post-synthetic modification. Jiang *et al.* prepared radical COFs by post functionalizing the channel wall of imine-linked COFs with TEMPO *via* click chemistry.[228] $[HC≡C]_{X\%}$-NiP-COFs (X = 0, 50, and 100) assembled by 5,10,15,20-tetrakis-(4′-tetraphenylamino) porphyrin (NiP) (62) with different molar ratios of 2,5-bis(2-propynyloxy)terephthalaldehyde (BPTA) (7) and 2,5-dimethoxyterephthalaldehyde (DMTA) (3) were grafted with 4-azido-2,2,6,6-tetramethyl-1-piperidinyloxy to yield $[TEMPO]_{50\%}$-NiP-COF and $[TEMPO]_{100\%}$-NiP-COF (Fig. 15a and b). After decorating TEMPO on the walls, a pair of reversible peaks appeared in CV curves. $[TEMPO]_{100\%}$-NiP-COF exhibited a capacitance of 167 F g^{-1} at 100 mA g^{-1}, similar to redox-active MOFs (Fig. 15c).

Recently, researchers found that the existence of interlayer hydrogen bonds can effectively enhance 2D COFs' electrochemical stability.[226,227,229] In the charge–discharge process of TpPa-(OH)$_2$ synthesized from 1,3,5-triformylpholoroglucinol (Tp) (24) and 2,5-dihydroxy-1,4-phenyldiamine [Pa-(OH)$_2$] (44), a concerted electron–proton transfer reaction occurred.[226] TpPa-(OH)$_2$ exhibited a capacitance of 416 F g^{-1} at 0.5 A g^{-1}, while high accessibility (43%) of redox-active hydroquinone units was achieved. The capacitance remained at 66% after 10 000 cycles, attributed to the fact that the H-bonding between the carbonyl oxygen of the benzoquinone functionality and its neighboring amine functionality inhibited the decomposition of benzoquinone.

Constructing conductive COFs is a promising method for designing high-performance COF-based supercapacitors. Gu, Li, and Yan *et al.* built a Ni-COF containing Ni(ɪɪ)-Salphen units.
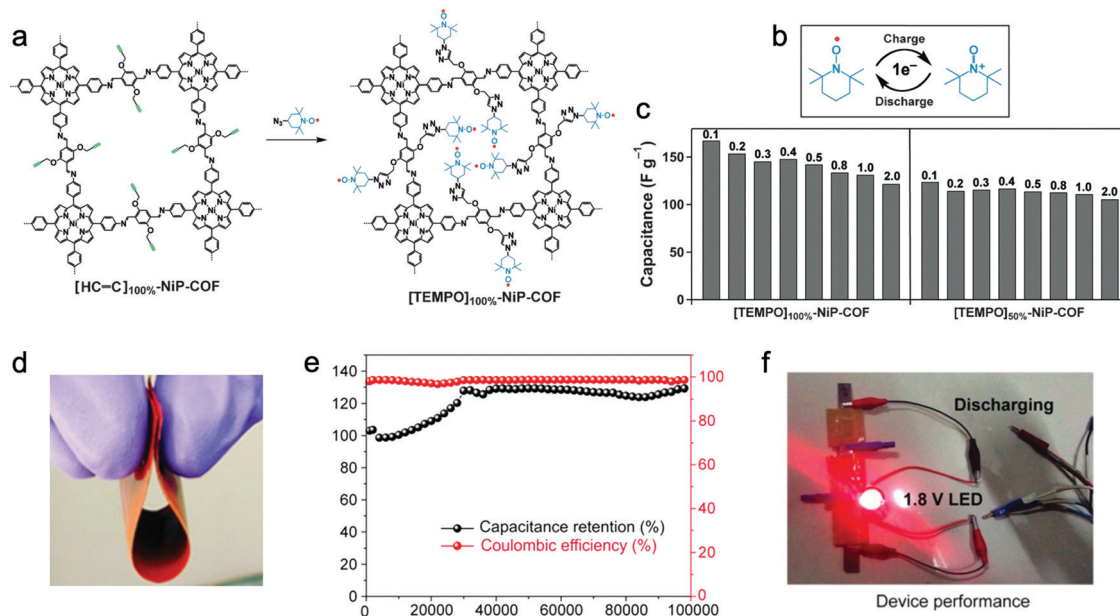
This journal is © The Royal Society of Chemistry 2020

Chem. Soc. Rev., 2020, **49**, 3565–3604 | **3585**

Fig. 15 (a) Schematic illustration of the synthesis of a radical COF ([TEMPO]$_{100\%}$-NiP-COF) in which TEMPO radicals are anchored on the walls. (b) The redox reaction involves one electron of TEMPO radicals during the charge–discharge process. (c) Capacitance of radical COFs at various current density (on the top). Reproduced from ref. 228 with permission from Wiley-VCH Verlag GmbH & Co. KGaA, copyright 2015. (d) Photo of the self-standing and flexible thin sheet. (e) Cycling performance of TpOMe-DAQ with 1 cm^2 area exposed. (f) Photo of the enkindling experiment: a 1.8 V LED was lighted by three solid-state-devices connected with each other. Reproduced from ref. 229 with permission from American Chemical Society, copyright 2018.

The Ni-COF possessed an electrical conductivity up to 1.3×10^{-2} S cm^{-1} and showed a high specific capacitance of 1257 F g^{-1} at 1 A g^{-1} with an outstanding cycling performance in that the capacitance remained at 94% after 10 000 cycles. An excellent energy density of 130 W h kg^{-1} at a power density of 839 W kg^{-1} was achieved after assembling in a two-electrode configuration. In contrast, the COF without Ni^{2+} (Ni$_0$-COF) exhibited an electrical conductivity of 8.4×10^{-6} S cm^{-1}, and a much lower capacitance of 184 F g^{-1} at 1 A g^{-1}. The great promotion of electrical conductivity may be attributed to the strong π-conjugation and square-planar Ni(II) coordination, which further improved the electrochemical performance.[254]

In the above-mentioned examples, pristine COFs are usually mixed with carbon black before measuring their capacitance. Preparing highly oriented COF films is able to effectively alleviate the influence of the grain boundaries and random orientation on the conductivity. A β-ketoenamine-linked 2D COF was used to fabricate crystalline and oriented thin films on the Au electrode surface with adjustable thickness.[249] The vertical orientation along with the stacking direction with respect to the substrate was determined by grazing incidence X-ray diffraction (GIXD). A much higher electrochemical accessibility (83%) of anthraquinone groups in DAAQ-TFP COF thin films was achieved compared to that of the randomly oriented microcrystalline COF powder (3%). A 7.5-fold increase in areal capacitance was observed from powder (0.4 mF cm^{-2} at 150 μA cm^{-2}) to films (3.0 mF cm^{-2} at 150 μA cm^{-2}). Besides, Banerjee *et al.* assembled and tested solid-state supercapacitors based on free-standing COF thin sheets.[229,230] For example, an imine-based COF, TpOMe-DAQ, was fabricated as uniform and

continuous thin sheets with a centimeter scale and a thickness of about 200 μm (Fig. 15d).[229] The pristine COF sheets exhibited an outstanding areal capacitance of up to 1600 mF cm^{-2} (gravimetric capacitance 169 F g^{-1}). Interestingly, an increment of the initial capacitance was obtained in the first 30 000 cycles under a current density of 10 mA cm^{-2}, and the resultant capacitance did not decay in the following 70 000 cycles (Fig. 15e). The activation process may be related to the increasing number of redox-active centers that became available to electrolytes during the cycling progress. The symmetric solid-state supercapacitor device was assembled with two 1 cm^2 pristine COF thin sheets and a 2 M aq. H$_2$SO$_4$/PVA gel (poly(vinyl alcohol)) as an electrolyte. The device showed a high areal capacitance of 84 mF cm^{-2} (8.8 F g^{-1}) and delivered energy and power densities of ∼2.9 μW h cm^{-2} and ∼61.8 μW cm^{-2}, respectively. Using these three solid-state devices connected in a series could light up a 1.8 V LED for 20 s (Fig. 15f).

Researchers also grew COFs on CNTs or graphene to enhance the composites' conductivity.[243,244] For instance, two β-ketoenamine-based 2D COF hybrid films with conductive carbon nanofiber (CNF) were prepared by including CNF into the COF precursor matrix.[243] The intermolecular π···π interaction between the π electrons in COF backbones and the sp^2 graphene carbons of CNF built efficient electron transfer pathways from COFs to the matrix. An increment of 10^9-fold in the electrical conductivity between COF-CNF hybrids (0.25×10^{-3} S cm^{-1}) and pristine COFs was found. The COF-CNF hybrids delivered a high areal capacitance of 464 mF cm^{-2} at 0.25 mA cm^{-2}, much higher than that of the mixture of COF and CNF (6.25 mF cm^{-2}), owing to the feasible long channel electronic movement through

3586 | *Chem. Soc. Rev.*, 2020, **49**, 3565–3604

This journal is © The Royal Society of Chemistry 2020

the $\pi\cdots\pi$ interaction. Integrating the COF-CNF-based super-capacitors with a highly efficient perovskite solar cell achieved a power conversion efficiency of 16.7% and an areal capacitance of 42.0 mF cm^{-2} for the 300 s photocharging at a current density of 0.25 mA cm^{-2}.

Besides, incorporating conductive polymers into the channels was proved to be a feasible strategy to enhance the electron transfer ability of COF-based composites.[242,245] As an example, a redox-active AQ-COF as a scaffold infiltrated with conductive poly(3,4-ethylenedioxythiophene) (PEDOT) was prepared by a facile *in situ* solid-state polymerization method.[242] The resultant PEDOT@AQ-COF nanocomposite showed an excellent electrical conductivity of 1.1 S cm^{-1}, which was 10 orders of magnitude higher than that of AQ-COF. In PEDOT@AQ-COF, the redox-active groups can directly receive the electrons from PEDOT chains encapsulated in the channels, providing a rapid electronic exchange between the working electrode and redox-active groups. Thus, PEDOT@AQ-COF showed a peak current density of 27 A g^{-1} at a sweep rate of 5 mV s^{-1} in CV measurements, while AQ-COF/PEDOT (the mixture of AQ-COF and PEDOT) showed only 1.8 A g^{-1}. The specific capacitance was up to 1663 F g^{-1} at 1 A g^{-1} for the all-organic PEDOT@AQ-COF. Besides, it also showed a comparable rate performance with a capacitance of 998 F g^{-1} at 500 A g^{-1} and was available to operate over 10 000 cycles at 50 A g^{-1} without capacitance decay.

3.2.2 Carbonization of COFs. Porous carbon materials have been widely employed as electrode materials for SCs, which are mostly derived from the thermal decomposition of precursors.[260–262] COFs are one such material with the advantages of intrinsic heteroatom doping (*e.g.* B, N, O, and S), providing a choice to form heteroatom-doped porous carbons for SCs by pyrolyzing.[112,256–259,263]

Hao *et al.* pyrolyzed a series of C_3-symmetric COFs under ionothermal conditions. The resultant porous carbons showed a typical double-layer capacitor behavior.[259] Three Schiff-base BTT-COFs with different pore sizes (BTT-DADP COF, BTT-DAB COF, and BTT-TAB COF) were synthesized and treated in melt ZnCl$_2$ at 700 °C for 20 h, leading to the formation of porous carbon materials. The surface area was largely increased after pyrolyzing, which may be attributed to the additive ZnCl$_2$ that provided the padding and supported the pore structures during thermal decomposition. The specific capacitance of BTT-DADP COF-700 assembled symmetric supercapacitor was more than 100 F g^{-1} at 1 A g^{-1}, and the capacitance remained at 77.5% of the initial after 10 000 cycles at 10 A g^{-1}. A similar strategy was implemented by Awaga and Wu *et al.*[253] The multiple heteroatom-doped carbons (ONC-T1s) with ultra-high specific surface area were pyrolysed from AQ-COF impregnated with K$_2$CO$_3$, in which ONC-T1-850 (S_{BET} = 1518 m^2 g^{-1}) showed a typical EDLC behavior, with a high specific capacitance of 1171 F g^{-1} at 1 A g^{-1}.

In addition to directly pyrolyzing pristine COFs to produce porous carbon materials, carbonizing the hybrid COF materials was also investigated. Talyzin *et al.* grew COF-1 perpendicularly to the surface of graphene (v-COF-GO) *via* covalent bonding.[112] The vertically oriented COF-1 may provide an interconnected pore network to facilitate ion diffusion. After carbonization in molten salts, the orientation of the resultant boron-doped carbon nanostructures (v-CNS-RGO) still remained, and v-CNS-RGO showed a good specific capacitance and excellent cycling stability.

With the rapid development of emergency multifunctional electronics, thinner and lighter supercapacitors with high volumetric power density are needed. The electrode materials are of vital importance. The volumetric energy density of a supercapacitor is positively correlated with its volumetric capacitance (equal to gravimetric capacitance multiplied by bulk density). However, there is a trade-off effect between the gravimetric capacitance and bulk density. For electrode materials, proper surface area with accessible pore volume for ions and high active site density can greatly promote the ion adsorption, which is beneficial for gravimetric capacitance but generally results in a relatively low bulk density. To achieve an ideal supercapacitor electrode, the materials are required to balance the density, porosity, and pore size, instead of only pursuing a high surface area. Furthermore, the capacitor performance is also influenced by other factors, such as electronic conductivity (amount of conductive additive, and electrochemical accessibility of COFs' redox-active sites), loading amount of active materials (volume fraction), and electrolyte system (working voltage). It is a challenge to well balance these parameters to fabricate an outstanding energy-storage device.

We have summarized the performances of supercapacitors based on COFs and carbonized COFs in Tables 3 and 4, respectively. Some of them were compared in the Ragone plot (Fig. 16),[264] possessing a decent energy density with an acceptable power density. Even few devices showed an energy density higher than 5 W h kg^{-1} at a power density greater than 1 kW kg^{-1} under a working voltage larger than 1 V, which can fulfill the basic requirements for the industry devices.

4 Electrochemical energy conversion

For catalysts used in electrochemical energy conversion, possessing catalytic sites with high activity and selectivity, high electrical conductivity for electron transport and path for rapid mass transport is highly desired. In addition, chemical stability towards water and long-term stability upon catalytic cycles also should be taken into consideration.

Many porous frameworks including amorphous porous organic polymers,[265,266] metal–organic frameworks (MOFs),[267,268] COFs,[267] and zeolite[269,270] have been reported to possess electrocatalytic activity and have led to great achievements. They have attracted great interest as electrocatalytic materials because of their large surface area and permanent porosity, which are beneficial for charge/mass transport and full contact between substrate and active sites. Compared with other host materials, COFs have several advantages: (1) in addition to the highly ordered structural feature, the active sites can be incorporated into either backbones or side chains with atomic precision, facilitating electrocatalytic mechanism study; (2) the chemical

Table 3 COF-based supercapacitors

Electrode	Specific capacitance	Current density	Working voltage (V)	Retention (cycle)	S_{BET} (m^2 g^{-1})	Ref.
In three-electrode configuration						
NIBDZ	88.4 F g^{-1}	0.5 A g^{-1}	0–1.0	93.61% (5000)	120	233
TPT-DAHQ COF	256 F g^{-1}	0.5 A g^{-1}	0.1–1.0	98.8% (1750)	1855	232
PDC-MA-COF	355 F g^{-1}	1.0 A g^{-1}	0–1.5	78% (9000)	748.2	227
DAB-TFP-COF	15 ± 6 F g^{-1}	0.1 A g^{-1}	−1.0 to 0.25	—	365	225
DAAQ-TFP-COF	48 ± 10 F g^{-1}			83.3 (5000)	435	
TpOMe-DAQ	169 F g^{-1}	3.3 mA cm^{-2}	−0.5 to 0.5	65% (50 000)	1531	229
[TEMPO]$_{100\%}$-NiP-COF	167 F g^{-1}	0.1 A g^{-1}	0–0.8	—	5.2	228
[TEMPO]$_{50\%}$-NiP-COF	124 F g^{-1}			100	264	
TPA-COF-1	51.3 F g^{-1}	0.2 A g^{-1}	0.2–0.7	—	714	234
TPA-COF-2	14.4 F g^{-1}				478	
TPA-COF-3	5.1 F g^{-1}				557	
TPA-COF-4	2.4 F g^{-1}				1132	
TFP-NDA-COF	348 F g^{-1}	0.5 A g^{-1}	0–1.0	75% (8000)	353	235
Dq$_2$Da$_1$Tp COF thin sheet	122 F g^{-1}	1.56 mA cm^{-2}	−0.7 to 0.3	—	1004	230
DqTpCOF thin sheet	154 F g^{-1}			—	940	
Dq$_1$Da$_1$Tp thin sheet	111 F g^{-1}			—	804	
Car-TPA COF	13.6 F g^{-1}	0.2 A g^{-1}	0–0.6	—	1334	236
Car-TPP COF	14.5 F g^{-1}				743	
Car-TPT COF	17.4 F g^{-1}				721	
TpBD-(OH)$_2$	90 F g^{-1}	0.5 A g^{-1}	−0.2 to 0.5	—	197	226
TpPa-(OH)$_2$	416 F g^{-1}			66% (10 000)	369	
TDFP-1	418 F g^{-1}	0.5 A g^{-1}	0–1.0	95% (1000)	651	237
TpPa-COF@PANI	95 F g^{-1}	0.2 A g^{-1}	0–0.7	83% (30 000)	574.4	238
SWCNTs-TpPa-COFs	153 F g^{-1}	0.5 A g^{-1}	−0.2 to 0.8	>2000	235.5	239
COFDAAQ-BTA-3DG	31 mF cm^{-2}	0.5 mA cm^{-2}	−1.05 to 0.4	24.0% (2000)	—	240
COFs/NH$_2$-rGO	533 F g^{-1}	0.2 A g^{-1}	0–0.5	79% (1000)	—	241
PEDOT@AQ-COF	1663 F g^{-1}	1 A g^{-1}	−0.2 to 0.6	>10 000	131	242
DqDaTp-CNF	364 mF cm^{-2}	0.25 mA cm^{-2}	−0.5 to 0.5	—	532	243
g-C$_{34}$N$_6$-COF/CNT MSC	13.1 mF cm^{-2}	2 mA cm^{-2}	0–0.8	93.1% (5000)	1003	244
PEDOT/DAAQ-TFP	350 mF/cm^3	—	−0.3 to 0.6	>10000	—	245
NH$_2$-f-MWCNT@COFTTA–DHTA	127.5 F g^{-1}	0.4 A g^{-1}	0–0.8	96% (1000)	1157	246
Fe$_3$O$_4$/COF-5d	112 F g^{-1}	0.5 A g^{-1}	−0.1 to 0.7	76% (2000)	872	247
NiNWs@TpPa-COFs	426 F g^{-1}	2 A g^{-1}	−0.2 to 0.6	>2500	596.7	248
DAAQ-TFP thin films	3 mF cm^{-2}	0.15 mA cm^{-2}	−2.0 to 0.5	93% (5000)	—	249
TaPa-Py COF	209 F g^{-1}	0.5 A g^{-1}	−0.3 to 0.4	—	687	250
DAB-TFP COF	98 F g^{-1}	0.5 A g^{-1}	−0.3 to 0.4	—	385	
TPPDA-TPTPE COF	237.1 F g^{-1}	2 A g^{-1}	−0.92 to 0.18	86.2 (5000)	1067	251
TPPDA-TPPyr COF	188.7 F g^{-1}			85.6 (5000)	1020	
PG-BBT	724 F g^{-1}	1 A g^{-1}	0–0.6	96% (10 000)	507	252
ONC-T1-700	768 F g^{-1}	1 A g^{-1}	0–0.6	98.3% (10 000)	3451	253
ONC-T1-850	1711 F g^{-1}			101.5% (10 000)	1518	
Ni-COF	1257 F g^{-1}	1 A g^{-1}	0–0.6	94% (10 000)	362	254
In two-electrode configuration						
PDC-MA-COF//AC	94 F g^{-1}	1.0 A g^{-1}	0–1.5	88% (20000)	748.2	227
CT-Dq1Da1TpCOF//CT-Dq1Da1TpCOF	8.5 mF cm^{-2}	0.39 mA cm^{-2}	0–1.0	78% (7000)	804	230
CT-DqTpCOF//CT-DqTpCOF	12 mF cm^{-2}	0.39 mA cm^{-2}		80% (2500)	940	
TpPa-(OH)$_2$//TpPa-(OH)$_2$	214 ± 1 F g^{-1}	0.2 A g^{-1}	0–0.7	88% (10000)	369	226
DqDaTp-CNF//DqDaTp-CNF	167 F g^{-1}	0.5 mA cm^{-2}	0–1	76% (4500)	532	243
PEDOT/DAAQ-TFP//AC	197 F g^{-1}	—	−0.9 to 0	—	—	245
TaPa-Py COF//TaPa-Py COF	102 F g^{-1}	0.5 A g^{-1}	0–0.8	92% (6000)	687	250
DAB-TFP COF//DAB-TFP COF	42.7 F g^{-1}			—	385	
e-JUC-510//e-JUC-510	4.17 mF cm^{-2}	1000 mV s^{-1}	0–1.3	—	666	255
e-JUC-511//e-JUC-511	5.46 mF cm^{-2}			100% (10000)	416.6	
e-JUC-512//e-JUC-512	5.85 mF cm^{-2}			100% (10000)	336	
PG-BBT//AC	220 F g^{-1}	1 A g^{-1}	0–1.5	—	507	252
ONC-T1-700/CNT//ONC-T1-700/CNT	480 F g^{-1}	1 A g^{-1}	0–0.6	—	3451	253
ONC-T1-850/CNT//ONC-T1-850/CNT	700 F g^{-1}			—	1518	
Ni-COF//AC	417 F g^{-1}	1 A g^{-1}	0–1.5	—	362	254
TpOMe-DAQ//TpOMe-DAQ	84 mF cm^{-2}	0.25 mA cm^{-2}	0–1	>70% (30000)	1531	229

and physical environment around the active sites is able to be easily modulated, resulting in the fine-tuning of their catalytic activity; (3) their chemical stability can be achieved by choosing proper linkages; (4) 2D COF NSs with conjugated electron structure may provide sufficient conductivity; (5) the rich choices in the linkers and linkages lead to tremendous opportunities for

the designing of high performance electrocatalysts. Moreover, despite boroxine and boronate linkage-based COFs are sensitive to moisture, most of the developed linkages (*e.g.*, imine, hydrazine, azine, ketene, imide, squaraine, triazine, and ethylenic linkages) are chemically stable in water.[56,271] The introduction of tautomerization, hydrogen bonding, and interlayer interactions

3588 | *Chem. Soc. Rev.*, 2020, **49**, 3565–3604

This journal is © The Royal Society of Chemistry 2020

Table 4 Carbonized COF for supercapacitors

| Electrode	Specific capacitance	Current density	Working voltage (V)	Retention (cycle)	S_{BET} (m^2 g^{-1})	Ref.
In three-electrode configuration						
TAPT-DHTA-COF$_{0.1}$@PPZS$_{900}$	411 F g^{-1}	0.5 A g^{-1}	−1.0 to 0	100% (10 000)	456	256
(N)G2	460 F g^{-1}	1 A g^{-1}	−1.0 to 0	90% (10 000)	1147	257
Carbonized ACOF1	234 F g^{-1}	1 A g^{-1}	−1.0 to 0	—	1596	258
In two-electrode configuration						
BTT-DADP COF-700//BTT-DADP COF-700	>100 F g^{-1}	1 A g^{-1}	0–3.5	77.5% (10 000)	2288	259
v-CNS-RGO//v-CNS-RGO	>160 F g^{-1}	1 A g^{-1}	−0.5 to 0.5	100% (3000)	700	112
(N)G2//(N)G2	175 F g^{-1}	0.2 A g^{-1}	0–1.0	—	1147	257
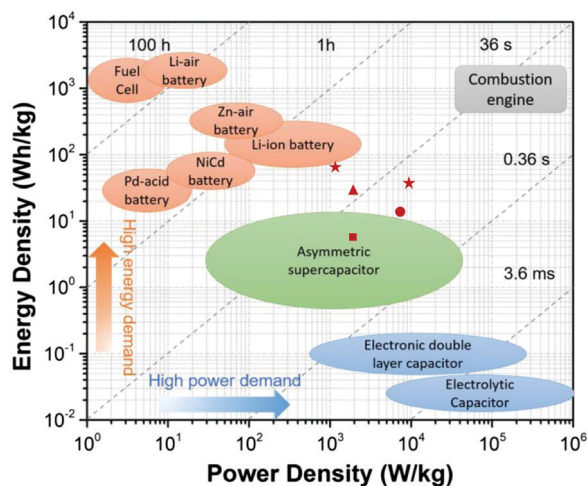
Fig. 16 The specific power *vs.* specific energy for EES devices delineated in the Ragone plot. Reproduced from ref. 264 with permission from American Chemical Society, copyright 2018. The electrochemical performance of COF-based supercapacitors has been reported: (★): ref. 252; (▲): ref. 226; (●): ref. 227; (■): ref. 250.

in the COFs can further improve the stability of imine linkage-based COFs in acidic and basic solutions. The polyaryl ether-based COFs are able to withstand harsh chemical environments including strong acids and bases, as well as oxidation and reduction conditions,[272] the stability of which outperformed most of the known crystalline porous materials.

To solve the conductivity problem of bulk COF materials in energy storage application, two general strategies are usually employed: the first one is to physically mix COFs with conductive supporting materials (*e.g.*, graphene and CNT) or directly grow COFs on them to prepare COF-based composites; the second one is treating COFs at high temperature to pyrolyze them into heteroatom-doped porous carbon. The former approach can retain the ordered structures of COFs and atomically distributed metal ions, which is beneficial for the maximal utilization of catalytic atoms and the realization of high selectivity and activity; the latter approach is easier to achieve high conductivity and robust chemical stability but suffers from the agglomeration of metal ions.

In this section, the recent advances related to the application of COFs in electrocatalysis, including oxygen reduction reaction (ORR), hydrogen evolution reaction (HER), oxygen evolution reaction (OER), and CO_2 reduction reaction (CO_2RR), are presented.

4.1 ORR

The oxygen reduction reaction (ORR, $O_2 + 4H^+ + 4e^- \rightarrow 2H_2O$), as a rate-determining step (RDS), plays a vital role in energy storage and conversion devices, including metal–air batteries and fuel cells.[273–276]

Fuel cells are electrochemical power generation devices that directly convert chemical energy into electrical energy. In proton exchange membrane fuel cells, hydrogen is oxidized at the anode to form protons and electrons, and electrons flow from the anode to the cathode to participate in the ORR, while the protons combine with the reduced oxygen species to form H_2O on the cathode in the electrolyte. They are considered as one of the new clean and efficient power generation technologies in the 21st century.

Metal–air batteries have attracted great interest around the world due to their high theoretical energy density (approximately 2–10 times higher than that of lithium-ion batteries).[277] The negative electrodes of metal–air batteries, combining the features of traditional batteries and fuel cells, are made of metals as in the case of traditional batteries. The oxygen supplied by air is continuously pumped into the cathode as the reactant to conduct ORR, whose efficiency greatly influences the battery voltage and energy density. Among the various kinds of metal–air batteries, Zn–air batteries exhibit great potential for future energy applications.

At present, Pt is considered to be the best ORR electrocatalyst in fuel cells.[278] Nevertheless, its scarcity, high cost, poor long-term stability, as well as low tolerance to the fuel crossover effect are main obstacles.[279] Among the benchmark performers of non-precious metal catalysts (NPMC) that display high activity and stability in catalysis, metal/nitrogen/carbon (M/N/C, M = Fe, Co, Ni, *etc.*) nanohybrids prepared by pyrolysis of precursors have been demonstrated to be one of the most promising candidates to replace Pt-based catalysts.[280,281]

4.1.1 COF-based metal-free electrocatalyst. Additionally, π-conjugated 2D covalent organic radical frameworks (CORFs) have been indicated to be electroactive for ORR. In 2018, Wu and co-workers synthesized the first π-conjugated 2D covalent organic radical framework PTM-CORF containing the polychlorotriphenylmethyl (PTM) radical.[192] The resulting PTM-CORF possessed a small bandgap (about 0.88 eV) and a low LUMO

This journal is © The Royal Society of Chemistry 2020

Chem. Soc. Rev., 2020, **49**, 3565–3604 | **3589**

energy level (-4.72 eV) ascribed to the strong electron-withdrawing feature of the PTM radical and the extended π-conjugation. Following this, the low-lying LUMO energy level and small bandgap of PTM-COR made it easy to accept electrons from oxygen and increase electrocatalytic activity toward ORR. Subsequently, they blended PTM-CORF with carbon black to test its electrocatalytic properties, showing a half-wave potential of 0.671 V (V $vs.$ RHE) under basic conditions and an electron transfer number of 3.89.

Direct pyrolysis of COFs always leads to the formation of an uncontrollable 3D carbon structure with the loss of the 2D structure and inherent porous feature, even though the precursors possess layered 2D structures. Accounting for these problems, Jiang and co-workers proposed a strategy based on template carbonization, which successfully converted a conventional COF (TAPT-DHTA-COF) into carbon sheets (PA@TAPT-DHTA-COF$_{1000}$) with high conductivity, hierarchical pores, and sufficient catalytic edges.[282] They inserted phytic acid (PA) as a template as well as directing agent into the channels and layers during pyrolysis of 2D COF at 1000 °C under N$_2$. The multi-fold functions of PA included stripping the layered 2D COFs into several small-sized carbon plates, guiding the conversion of 2D COFs to 2D carbon when it covered the surface of COFs, triggering the formation of 2D porous carbon structure during its network decomposition, and finally, supplying the carbon sheets with phosphorus. For ORR in aqueous KOH solutions (0.1 M), the resulting PA@TAPT-DHTA-COF$_{1000}$ reached an E_0 value of 0.921 V (V $vs.$ RHE), an $E_{1/2}$ value of 0.751 V (V $vs.$ RHE) and a limit current density of 6.5 mA cm^{-2}. They further improved its ORR activity by pyrolyzing it at 900 °C under NH$_3$ to form PA@TAPT-DHTA-COF$_{1000NH_3}$, whose ORR catalytic performance (E_0, 0.941 V; $E_{1/2}$, 0.831 V; j_{limit}, 7.2 mA cm^{-2}) was superior to that of Pt/C (E_0, 0.911 V; $E_{1/2}$, 0.781 V; j_{limit}, 6.0 mA cm^{-2}).

4.1.2 Metal-containing COF-based electrocatalyst. Metalloporphyrin-based COFs have attracted great attention for electrocatalysis, owing to the fact that porphyrins with N chelating sites act as diluents isolating metal atoms to avoid metal agglomeration during COFs' synthesis and the following pyrolysis process if needed.[283–287] Luo et $al.$ prepared a reduced graphene oxide/Co-porphyrin-based COF network (CoCOF-Py-rGO) by anchoring the COFs to the pyridine-functionalized reduced graphene oxide.[284] Owing to the existence of pyridine functional groups serving as structural nodes, the as-synthesized CoCOF-Py-rGO exhibited a 3D structure. It showed an ORR activity with an onset potential of 0.84 V, a half-wave potential of 0.765 V, as well as good stability and methanol tolerance in an alkaline environment. In 2015, Mao and co-workers prepared a Co/N/C catalyst (Co-COF-900) for ORR by pyrolysis of a cobalt-porphyrin-based COF under a nitrogen atmosphere at 900 °C. Electrochemical studies demonstrated that both the potential and current responses obtained from Co-COF-900 were close to those of commercial 20% Pt/C.[286]

In 2019, Thomas's group reported a "salt-mediated technique" for COFs' growth with p-toluenesulfonic acid (PTSA) as a molecular organizer during bipyridine-COF (TpBpy) synthesis and silica nanoparticles as hard templates to facilitate the formation of mesoporous structures (Fig. 17a).[130] Iron species were introduced into the system coordinated with bipyridine moieties to produce SiO$_2$@TpBpy-Fe, which then formed Fe–N$_x$ sites after a subsequent pyrolysis process followed by the treatment with HCl and NaOH.[288] Electrocatalytic studies showed that the resultant mC-TpBpy-Fe exhibited almost comparable values (E_0 of 0.920 V, $E_{1/2}$ of 0.845 V) to those of commercial Pt/C under basic conditions (Fig. 17b and c). More importantly, it showed long-term durability and good tolerance to methanol during the catalytic reaction and a competitive discharge performance when applied in a Zn–air battery.

Single-atom catalysts (SACs) take advantage of maximal atom utilization and high catalytic activity. However, the isolated metal atoms in the materials tend to agglomerate under elevated temperatures due to their thermodynamic instability.[152,289,290] Therefore, the process for preparing a single-atom catalyst by pyrolysis requires fine adjustment of the carbonization temperature and the reduction of metal ion loading. Recently, Peng, Shi, and Huo et $al.$ synthesized SACs with good electrocatalytic activity via a pyrolysis-free synthetic method.[289] They first prepared a fully closed π-conjugated COF (COF$_{BTC}$) via benzene-1,2,4,5-tetracarbonitrile polymerization and then assembled it with the graphene matrix via intermolecular interaction. The as-synthesized pfSAC-Fe catalysts showed excellent electrocatalytic performance for ORR. When the ratio of COF$_{BTC}$ was increased, the $E_{1/2}$ value changed from 0.88 V to 0.91 V. Besides, the optimized catalyst, pfSAC-Fe-0.2, showed a high kinetic current density J_k of 25.86 mA cm^{-2}, a low Tafel slope of 31.7 mV and good methanol tolerance, which were superior to those of commercial Pt/C ($E_{1/2}$, 0.86 V; J_k, 6.49 mA cm^{-2}). The pfSAC-Fe driven Zn–air battery exhibited a specific capacity of 732 mA h g^{-1} at 100 mA cm^{-2} with 89.3% zinc utilization and a power density of 123.43 mW cm^{-2} (which was higher than that of the battery driven by Pt/C (113.81 mW cm^{-2})). Moreover, it exhibited a remarkable long cycling life over 300 hours with less than 0.1% decrease, whereas the performance of the Pt/C-based battery decreased within 20 hours.

4.2 OER

OER as an anodic reaction occurs in water splitting and in the charging processes of rechargeable metal–air batteries. As seen from the reaction pathways of OER, H$_2$O is oxidized to O$_2$ accompanied with 4e$^-$ transfer. OER can operate in either acidic or alkaline solutions, and the corresponding processes are 2H$_2$O → O$_2$ + 4H$^+$ + 4e$^-$ and 4OH$^-$ → O$_2$ + 2H$_2$O + 4e$^-$, respectively.

Unfortunately, OER suffers from sluggish kinetics owing to the large energy barriers in the complex procedures including breaking four O–H bonds, removing four electrons from H$_2$O molecules, and forming energy-intensive O–O bonds. RuO$_2$ and Ir-based materials are considered to be benchmarked electrocatalysts for OER. However, limited storage, high cost, and poor availability of these noble metal-based electrocatalysts hamper their wide commercial usage. Thus, there is an upsurge in attempts to develop effective, low-cost, and stable catalysts for oxidizing water with minimum energy.
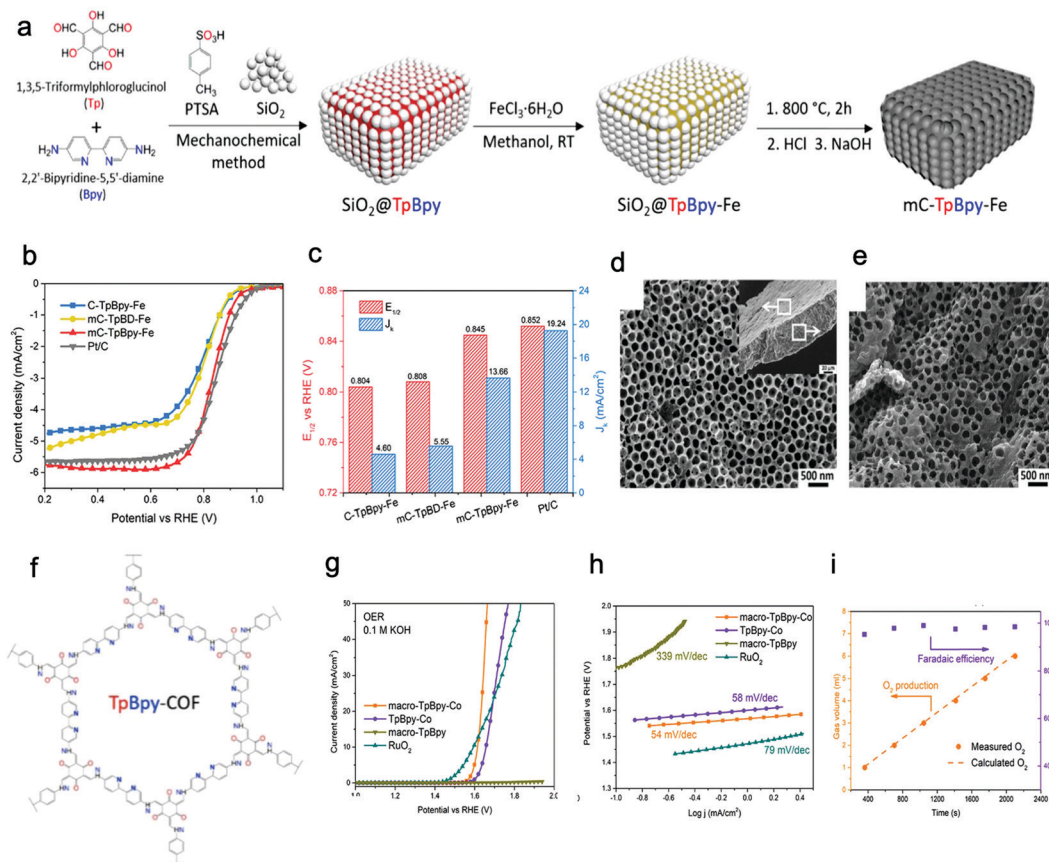
Fig. 17 (a) Synthesis of mC-TpBpy-Fe by PTSA-assisted mechanical milling using SiO₂ nanoparticles as the hard template. (b) LSV curves of mC-TpBpy-Fe, mC-TpBD-Fe, C-TpBpy-Fe, and Pt/C in O_2^- saturated KOH solution. (c) Corresponding columnar charts of these samples' half-wave potential and kinetic current (at 0.8 V). Reproduced from ref. 288 with permission from American Chemical Society, copyright 2019. (d) and (e) Top-view and cross-sectional SEM images of macro-TpBpy, respectively. (f) Chemical structure of macro-TpBpy. (g) OER polarization curves. (h) Tafel plots of macro-TpBpy, TpBpy-Co, macro-TpBpy-Co, and RuO₂ catalysts. (i) Faradaic efficiency of macro-TpBpy-Co for oxygen evolution. Reproduced from ref. 300 with permission from American Chemical Society, copyright 2019.

In order to better evaluate and compare the properties of OER electrocatalysts, a series of criteria have been established, involving η_{10} (the overpotential needed to generate a catalytic current density of 10 mA cm^{-2}), j_0 (the value of OER current density), Tafel slope, the yield of oxygen, turnover frequency (TOF), and faradaic efficiency (FE). Besides, since OER involves the generation and liberation of oxygen, the problem arising from the leaching of the catalyst leading to suboptimal long-term stability should be taken into account. Moreover, the nonconducting gas phase will hinder the exposure of active sites and cause the current density to decrease.

As an alternative candidate, transition metal-based materials became the subject of comprehensive research on OER electro-catalysts. So far, Fe/Co/Ni/Mo/Zr/V-based materials (either free-standing or supported on other materials)[291] have been explored for catalyzing OER, among which cobalt-based catalysts became one of the hot spots. In the case of free-standing transition metal-based catalysts, a number of them suffered from high overpotential and sluggish kinetics in the electrochemical study. On the one hand, there still exist lots of molecular water-oxidizing complexes (WOCs) that will be eventually dissociated into a homogeneous phase during catalysis.[292,293] On the other

hand, carbon materials[294] and metal foam[295,296] as platforms to support metal nanoparticles or clusters as catalytic active materials also confront several problems, such as complicated synthetic procedures.[297,298] COFs equipped with some inherent virtues appear satisfactory for preparing electrocatalysts.

In 2016, Banerjee and Kurungot *et al.* designed Co-TpBpy *via* coordinating Co species to the bipyridine sites on the TpBpy-COF synthesized by the Schiff-base condensation of Tp (24) and 2,2′-bipyridyl 5,5′-diamine (Bpy) (50).[299] The resulting Co-TpBpy retained high accessible surface area (450 m² g^{-1}) and porosity. The electrochemical properties measured in 0.1 M aqueous phosphate buffer (pH = 7) showed an overpotential of 400 mV at a current density of 1 mA cm^{-2}, a TOF of 0.23 s^{-1}, a Tafel slope of 59 mV dec^{-1}, an FE of 95%, and good cycling stability. Further, Thomas *et al.* introduced polystyrene spheres as hard templates and PTSA during the preparation process to enable the formation of TpBpy-COF with a hierarchical pore structure (Fig. 17d–f).[300] Macro-TpBpy-Co exhibited an out-standing performance as a OER catalyst with an overpotential of 380 mV at a current density of 10 mA cm^{-2}, a Tafel slope of 54 mV dec^{-1}, and an FE of 98% (Fig. 17g–i). It should be noted that the TOF value of Macro-TpBpy-Co was much higher than

This journal is © The Royal Society of Chemistry 2020

Chem. Soc. Rev., 2020, **49**, 3565–3604 | **3591**

that of microporous TpBpy-Co and RuO₂. The good electro-catalytic properties were attributed to the homogeneous and continuous macroporous structure, which could facilitate the transportation of O₂ gas bubbles and thereby promote the reaction. It was proved that the Co ions coordinated with pyridine not only worked as the active sites but also increased the conductivity of the catalyst.

Additionally, COFs have been utilized as supports for metal nanoparticles (NPs). The size of NPs and the electronic inter-action between the NPs and the host COFs both played impor-tant roles in enhancing their catalytic activity. For instance, IISERP-COF2 was prepared by using nonplanar building units with tetrahedral sp³ nitrogen, which introduced flexibility in COF skeletons to generate mesopores capable of confining the *in situ* formation of $Co_xNi_y(OH)_2$ NPs down to about 2 nm size without any end-capping reagent.[301] Owing to the localized electronic interactions between the NPs and the COF skeleton, the resultant nanocomposite exhibited an excellent performance

toward the OER process with an overpotential of 258 mV at 10 mA cm⁻² in 0.1 M KOH, which was close to the record of about 200 mV for noble-metal-free electrocatalysts. Also, it possessed a Tafel slope of 38.9 mV dec⁻¹, indicating outstanding kinetics. Similarly, metallic Ni₃N NPs were loaded in a 2D benzimidazole-based COF (IISERP-COF3) with donor–acceptor nodes and face-to-face stacked layers of conjugated π-components that were crucial to generate aligned conduction pathways.[302] The resulting IISERP-COF3_Ni₃N possessed a low overpotential of 230 mV at 10 mA cm⁻², a TOF value of 0.52 s⁻¹, an FE of 0.98 at 1 mA cm⁻², a Tafel slope of 79 mV dec⁻¹, and an O₂ evolution rate of 230 mmol h⁻¹ g⁻¹.

To enhance the conductivity, COFs have also been pyrolyzed into carbon hosts for OER reaction. Kurungot and Vaidhyanathan *et al.* developed a soft pyrolysis approach to prepare two compo-sites consisting of small RuO₂ NPs and carbon derived from COFs (Fig. 18a and b). They explained that the preparation of RuO₂ nanoparticles usually requires surfactant assistance and
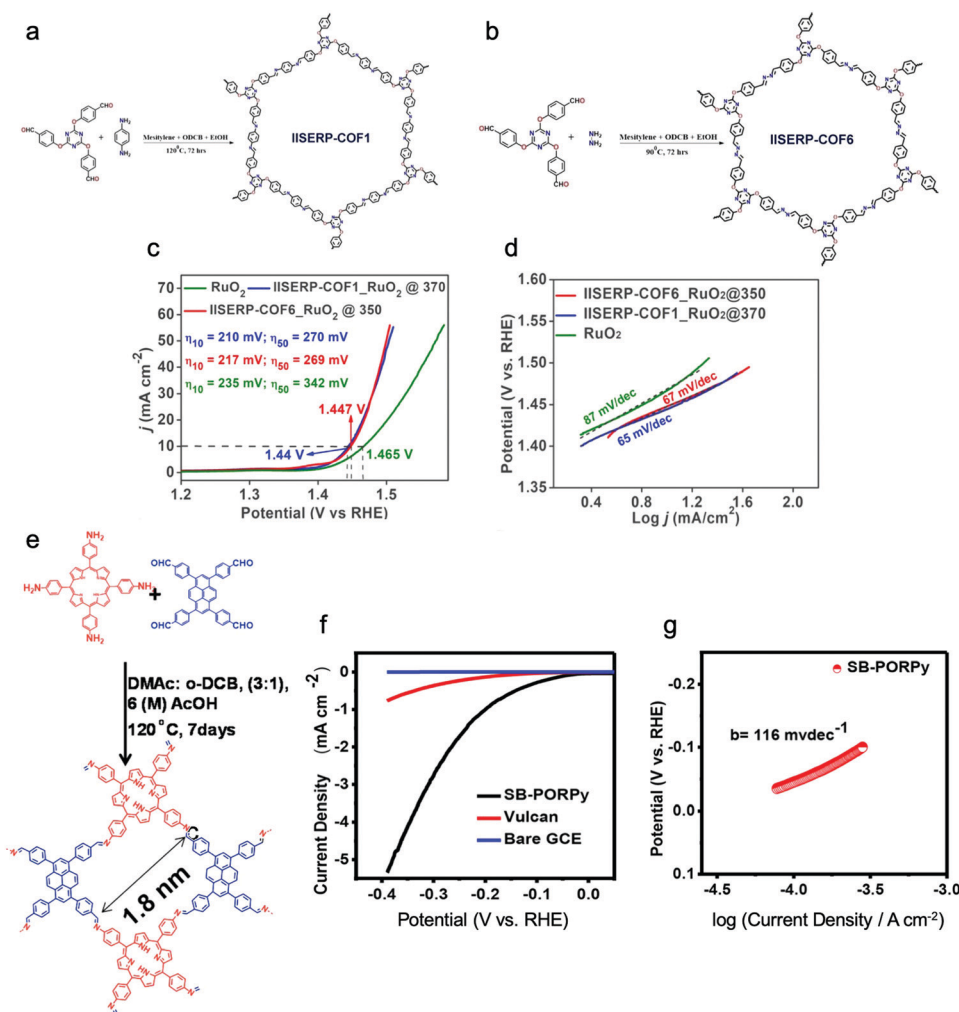

Fig. 18 (a and b) Schematic illustration of the reaction of IISERP-COF1 and IISERP-COF6. (c and d) LSV curves (left) and Tafel slopes (right) of IISERP-COF1 and IISERP-COF6. Reproduced from ref. 303 with permission from American Chemical Society, copyright 2019. (e) Synthetic scheme of COF (SB-PORPy). (f) Polarization curves for the hydrogen production on GC, Vulcan, and SB-PORPy-COF electrodes. (g) Tafel slope of the SB-PORPy-COF electrode. Reproduced from ref. 308 with permission from American Chemical Society, copyright 2017.

3592 | *Chem. Soc. Rev.*, 2020, **49**, 3565–3604

This journal is © The Royal Society of Chemistry 2020

high-temperature annealing under oxidizing conditions. However, when the temperature was higher than 500 °C, the size of RuO_2 NPs would increase significantly. Therefore, they controlled the temperature to about 400 °C and finally obtained $RuO_2@C$ composite materials by the soft pyrolysis method. The two resultant composites exhibited good OER performance with a η_{10} of 210 and 217 mV for composite-I and composite-II, respectively (Fig. 18c and d).[303] It is worth noting that most of the small-sized NPs were dispersed within the interlayers of the pyrolyzed COF, only leaving fewer on the surface to form more accessible active sites.

There are other strategies for producing efficient COF-based electrocatalysts such as introducing transition metal species into macrocyclic clusters (e.g., porphyrin and phthalocyanine) and blending metal-porphyrin with other conductive materials (e.g., metal foam and CNTs).[118,304] For instance, Chen and Zhang et al. developed a metalloporphyrin-based GDY (graphdiyne) analogue (Co-PDY nanosheets) synthesized via Glaser–Hay coupling reaction on copper foam.[118] During the catalytic process, the cobalt centers of metalloporphyrin acted as electrocatalytic active sites, while rapid electron transfer occurred inside the skeleton and the expanded pore structure accelerated the small molecules' diffusion. These three factors endow Co-PDY with superb OER catalytic performance (low overpotential of 270 mV at 10 mA cm^{-2}, Tafel slope of 99 mV dec^{-1}, and long-term cycling stability) (Fig. 19a–e), which was superior to that of commercial catalysts such as RuO_2 (η_{10} of 370 mV), IrO_2 (η_{10} of 340 mV), Ru/C (20%) (η_{10} of 390 mV), and Ir/C (20%) (η_{10} of 380 mV).
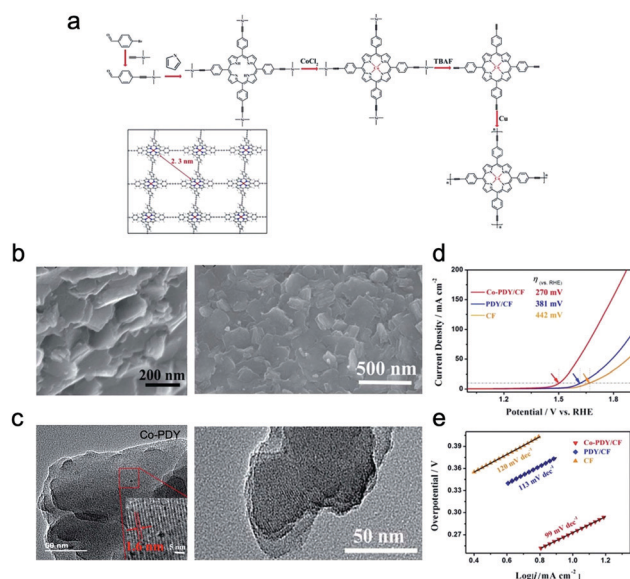

Fig. 19 (a) Schematic illustration of the reaction of Co-PDY. (b) SEM images of Co-PDY/CF before (left) and after (right) the continuous electrocatalysis test for 10 h. (c) TEM images of Co-PDY/CF before (left) and after (right) the continuous electrocatalysis test for 10 h. (d) LSV curves of Co-PDY/CF, PDY/CF, and CF. (e) Tafel slope of Co-PDY/CF, PDY/CF, and CF. Reproduced from ref. 118 with permission from the Royal Society of Chemistry, copyright 2019.

4.3 HER

Hydrogen, as a kind of clean fuel with high energy density, has been deemed to be one of the most promising alternative candidates to replace fossil fuels. At present, hydrogen is mostly produced by steam reforming of hydrocarbons. Besides, heating coal at high temperature without oxygen or partially burning coal with steam can also generate hydrogen; however, these techniques are with a high energy cost and are tedious because hydrogen needs to be separated from the mixture gases of H_2, CO, CO_2, etc.[305] The electrolysis of water is an ideal method to produce high-purity H_2 via HER. The procedure of electrocatalytic HER is a multi-step reaction involving adsorption, reduction, and desorption processes, including a Volmer step ($H^+ + e \rightarrow H_{ads}$) and a Tafel step ($H_{ads} + H^+ + e \rightarrow H_2$) or a Heyrovsky step ($2H_{ads} \rightarrow H_2$). To date, Pt-based materials show the best electrocatalytic performance toward HER but scarcity and high cost limit their large-scale practical applications. The transition-metal-based catalysts applied for electrocatalytic HER still suffer from the corrosion of the metal or leaching of metal ions and easier deactivation, which are the major obstacles for their commercial utilization.[306,307] Thus, tremendous efforts have been devoted to investigating efficient metal-free electrocatalysts for HER. Recently, metal-free COF-based materials have been reported to show good HER activity.[308,309]

For example, SB-PORPy-COF prepared by assembling porphyrin and pyrene units via the Schiff-base reaction was applied for HER (Fig. 18e).[308] It possessed high surface area ($\sim$869 m^2 g^{-1}), permanent microporosity, and excellent stability, allowing it to achieve electrocatalytic properties with an onset potential of 50 mV, a low overpotential of 380 mV at 5 mA cm^{-2}, and a Tafel slope of 116 mV dec^{-1} (Fig. 18f and g). Recently, free-standing 2D conjugated COF films were also applied to electrocatalyze HER. Li's group reported that graphene-like 2DCCOF1 with homogeneous pores was prepared by Suzuki polymerization on the interface of water and toluene at 2 °C.[309] To explore potential applications in electrocatalysis, they horizontally deposited the 2DCCOF1 film on a copper electrode and an electrochemical study showed that the 2DCCOF1 coated electrode was active for catalyzing HER with an overpotential of 541 mV at 10 mA cm^{-2} and a Tafel slope of 130 mV dec^{-1}. However, the performance of the COF-based catalysts mentioned above did not exceed the performance of MoS_2 nanosheets (benchmarked Pt-free HER catalyst) with an overpotential of 187 mV at 10 mA cm^{-2} and a Tafel slope of 43 mV.[310]

4.4 CO₂ reduction

The massive emission of CO_2 caused by the consumption of fossil fuels and industrial production has become a serious environmental issue, leading to worldwide extensive research on efficient and eco-friendly technologies for converting CO_2 into other value-added carbon products.[311] Indeed, extensive approaches have been attempted to facilitate this transformation, among which the electrolytic approach emerged as a promising route to reduce CO_2. It benefits from the following aspects: (1) using water as reaction media is in favor of promoting proton

This journal is © The Royal Society of Chemistry 2020

Chem. Soc. Rev., 2020, **49**, 3565–3604 | **3593**

and electron transfer; (2) since the final products can be used as fuels and chemical feedstocks and the electrolyte can be adequately recycled, zero-emission of pollutants in the overall process is realized; (3) the electricity used can be originated from renewable resources including wind, solar, geothermal energy, *etc.*[312–314]

Typically, the electrochemical reduction (ECR) of CO_2 involves multiple steps to different products, accompanying 2-, 4-, 6-, 8-, 12-, 14-, or 18-electron reaction pathways. There are three major steps for heterogeneous catalysis: (1) chemical adsorption of CO_2 on active sites of electrocatalysts; (2) electron transfer and/or proton migration to cleave C–O bonds and/or form C–H bonds; (3) configuration rearrangement of products (*e.g.*, CO, $HCOO^-$ or HCOOH, CH_4, C_2H_4, C_2H_5OH, and CH_3OH) followed by desorption from the electrode surface and dissolution in the electrolyte.[315]

There still remain several challenges to achieve efficient conversion of CO_2: (1) a large overpotential is required to produce the $CO_2^{\bullet-}$ intermediate due to the high energy barrier for its formation; (2) sluggish kinetics, interference of competitive off-pathway reduction of water as well as the limited soluble and mass transfer ability of CO_2 lead to a low conversion efficiency; (3) the feedstocks produced in the process are mixed together and separating them is a high-cost process; (4) catalytic active sites of electrocatalysts may be blocked and destroyed by impurities and by-products in the reaction system, resulting in a limited lifetime.[313] Consequently, the electrocatalysts for CO_2 reduction should be designed with high activity and selectivity.

Many investigations have elaborated that COF-based materials are capable of acting as electrocatalysts for CO_2 reduction.

Metalloporphyrins/phthalocyanines, as well as related complexes, are highly promising as CO_2 conversion electrocatalysts.[316–321] Yaghi and Chang *et al.* incorporated cobalt porphyrin units into COFs and the resulting COF-366-Co promoted carbon monoxide evolution in a neutral CO_2 saturated solution at −0.67 V with an overpotential of −0.55 V.[39] COF-366-Co exhibited a high FE (90%) and turnover number (up to 290 000) without decomposition over 24 hours. Furthermore, they developed a COF-366-Co analogue, namely COF-367-Co, by replacing 1,4-benzenedicarboxaldehyde (BDA) with BPDA as the strut. Cyclic voltammetry studies showed that COF-367-Co displayed improved catalytic performance with an onset potential of −0.40 V and an increased FE (91%) at −0.67 V. They explained that the larger pores in expanded COF-367-Co enabled higher CO_2 adsorption and provided more possibilities for CO_2 to contact active sites, finally resulting in enhancement in activity and selectivity.

In most cases, COFs are synthesized *via* solvothermal methods to form powders, followed by drop-casting onto electrode surfaces for electrocatalysis. However, there is only a small quantity of COF reaction centers remaining electrochemically accessible and electroactive. Besides, the low aqueous solubility, and confined diffusion and adsorption of CO_2 within the COF channels hinder the CO_2 reduction process. Following this, many researchers have attempted to directly grow COFs onto the surface of electrodes to prepare thin films.[39,320,322] A series of oriented COF films were prepared on HOPG and

their electrocatalytic activity toward CO_2 reduction was investigated.[322] The resulting COF-366-Co film exhibited apparently improved catalytic ability with an FE of 87%. In addition to porphyrin and phthalocyanine macrocycles, tricarbonyl rhenium(i) complexes had quite a high catalytic activity. It was evidenced that COF-2,2′-bpy-Re containing Re-2,2′-bpy fragments could work as an electrocatalyst for CO_2 reduction.[323] COF-Re_Co and COF-Re_Fe, containing both metalloporphyrin and metal bipyridine fragments, were prepared and showed a certain degree of CO_2 reduction activity.[319]

Metal-free COF based electrocatalysts for CO_2 reduction[324–326] have been reported recently. Deng's group[324] reduced the imine linkage in a 3D COF (COF-300) to form more stable COF-300-AR, which exhibited a good electrocatalytic performance for CO_2 reduction with a good CO conversion efficiency. They elaborated that the obvious activity of COF-300-AR for CO_2 reduction could be attributed to the porosity of COFs, which facilitated the diffusion of CO_2 molecules to the electrode, and after that, amine groups close to the electrode surface promoted the conversion of CO_2 into carbamate intermediates.

5 Summary and outlook

In this review, we have summarized the recent progress in the synthetic methods of COF NSs and thin films, along with the potential applications of COFs in batteries, capacitors, and electrocatalysts.

5.1 Synthetic strategy of COF NSs and thin films

To date, several approaches to design COF NSs and thin films with desired structure, chemical property, and thickness have been proposed, which are of great importance to investigate their properties for diverse applications. The synthetic strategies are classified into "bottom-up" and "top-down" approaches, both of which have their own merits and limitations.

In the case of the bottom-up strategy, solvothermal synthesis has received a considerable amount of attention because of its easy operation and broad applicability. When using the solvothermal method, the type and ratio of the selected solvents as well as the heating temperature have a significant influence on successfully controlling the morphology and periodicity of COF NSs and films. Additionally, the heated solvents under high pressure may promote the progress of the reaction and provide a unique environment for the formation of products. However, this method has a relatively insufficient ability to control the thickness of COF films and a certain number of unreacted monomers and oligomers are present in the obtained products.

Considering the on-surface synthesis, this method has been illustrated to be effective for synthesizing single-layered nanomaterials. It is essential to select the appropriate substrates. Specifically, well-defined single-crystal surfaces are capable of providing an ideal atomically flat surface to guide the growth of NSs and thin films in two dimensions and support the resulting products for further applications. Moreover, the appropriate interactions between the substrates and monomers can assist

3594 | *Chem. Soc. Rev.*, 2020, **49**, 3565–3604

This journal is © The Royal Society of Chemistry 2020

the dispersion of precursors on the surface, in favor of avoiding the formation of multi-layer structures and facilitating the formation of high-quality COF NSs and thin films. The commonly used substrates include graphene, HOPG, and metal substrates (Au, Ag, Cu, *etc.*). It is worth mentioning that metal substrates may catalyze the coupling reaction on the surface to confine the formation of highly ordered sCOFs. However, most of the syntheses were conducted under UHV conditions, resulting in unexpected irreversible cross-linking and giving rise to the formation of disordered nanostructures. To improve the surface coverage and reduce the degree of disorder, manipulating the kinetic process by controlling the feed rate of building units may provide a solution. On the other hand, introducing a small amount of water in a closed system to maintain the reaction balance and enhance reversibility is favourable for obtaining uniform sCOFs with few defects. Additionally, directly polymerizing at room temperature by the solid–liquid interface method is able to prepare sCOFs with limited monomers of small molecular sizes. However, the surface coverage and periodicity of sCOFs still require further improvement and the as-formed sCOFs are difficult to be peeled off from the substrates.

The interface formed between liquid and liquid or air can also provide a confined space for the growth of COF NSs and thin films. Different monomers (sometimes involving catalysts) are dissolved in one or two (compatible or incompatible) solvents. Under certain conditions of temperature and pressure, the precursors polymerize at the interface to form relatively large-sized COF films and NSs. However, this approach seems to be not efficient enough to produce well-ordered and high-quality thin COF films, and it is difficult to control the number of COF layers by this means as well.

For the top-down strategy, it is a method of stripping bulk COFs into single-/multi-layered COF NSs by introducing external (sometimes by internal) forces or solvents rather than growing them directly on selected substrates or interface. Compared to the bottom-up approach, this method is easier for scale-up but suffers from the difficulties in controlling the thickness, homogeneity, and quality of COF NSs. We elaborated on the top-down strategy involving mechanical exfoliation, solvent-assisted exfoliation, chemical exfoliation, and self-exfoliation as well as the difference among them that can be attributed to distinct peel strength. The mechanical exfoliation of bulk COFs *via* ball milling or grinding is a conventional exfoliation technique that applies mechanical forces to break the van der Waals interaction between the layers of bulk COF materials without destroying the covalent bonds of the frameworks; then, single- or few-layered 2D COF nanosheets are produced. Moreover, solvent-assisted exfoliation under sonication conditions is also widely used for COF exfoliation. In contrast, the self-exfoliation approach is more likely to depend on internal forces among the building blocks to strip the multi-layered COFs into the single or few-layered structure. Several iCOFs are exfoliated by mixing with solvents in a self-exfoliation method.

Although great achievements have been made, some obstacles need to be overcome in future development. (1) Quality: it is difficult to precisely control the degree of periodicity, crystal domain area, molecular orientation, and defect of the COF films and NSs. Thus, insightful mechanism studies on the growth of COFs based on advanced *in situ* characterization techniques (*e.g.*, TEM, XPS, and Raman spectroscopy) are required; (2) Diversity: in different approaches, due to the solubility, activity, and volatility of the monomers as well as the reversibility of the reactions only limited number of COF films and NSs have been prepared. Therefore, it is desired to develop more facile preparation methods with improved applicability; (3) Electrochemical stability: despite the fact that most of the COFs are chemically robust and are even stable against harsh chemical environments, their electrochemical stability still requires further deep investigation; (4) Scale-up: only up to centimeter-sized COF films and NSs with low yield have been prepared and the reaction conditions always require a large amount of organic solvent, high vacuum, ultra-regular surface, and long production period. Besides, the structure–function relationships of COF films and NSs still remain to be largely explored.

5.2 COFs for energy storage and conversion

Within the last few years, research on COF-based electrochemical energy storage has emerged rapidly and become diversified. As a concluding remark, the research directions focused on EES are summarized:

(1) As the electrode: COFs are positioned to address the challenge in organic electrode materials with a controllable degree of porosity and more stable frameworks (*e.g.*, various organic solvents, and strong acid or base). The following issues should be considered to achieve higher performance: enhancing the density of redox-active sites; increasing or decreasing the voltage plateau for cathode and anode, respectively; increasing the electron conductivity to fully utilize their redox-active sites; balancing the density and porosity by structural optimization to utilize their pores and active sites efficiently; widening the operation potential windows by using organic electrolytes or ionic liquid electrolytes in supercapacitors; charge–discharge mechanism is unclear (especially for anode), and theoretical and experimental studies need to be further investigated.

(2) As the host for the phase-changing component: the prerequisites for COFs to act as a host in phase changing cathode-based batteries, such as Li–S batteries, are high specific surface area and large pore volume, leading to high active component loading in composites. Besides, the introduction of specific functional groups can provide interactions to restrain the migration of soluble intermediates out of the pores and further inhibit the shuttle effect.

(3) As an electrolyte: the ionic skeleton can effectively promote ion-pair dissociation and facilitate ion migration, and the transference number of target ions can be improved by using different strategies. COFs incorporated with flexible chains provide a chance to solve the crystallization and phase transition problems in polymeric electrolytes, leading to a wide usage temperature range. However, when targeting all-solid-state electrodes for portable devices, it is urgently needed to

This journal is © The Royal Society of Chemistry 2020

Chem. Soc. Rev., 2020, **49**, 3565–3604 | **3595**

develop solvent-free flexible COF films with improved ion conductivity and transference number. Moreover, besides the Li^+ ion, the conduction behaviors of other ions, such as Na^+, K^+, Mg^{2+}, Zn^{2+}, and Al^{3+}, have remained unexplored.

(4) As dramatically developed materials, COFs are still very young in the EES fields. Owing to their ordered structures, designable pore size, modifiable skeletons, and high specific surfaces, they have huge potential for developing higher theoretical gravimetric energy density EES systems. Recently, many new fields of EES were investigated, such as aqueous zinc ion batteries,[327] Li–CO2 batteries,[183,328] and artificial SEI layers for use in anodes.[329]

COFs combine the merits of both molecular and heterogeneous catalysts, and many inherent advantages make them promising candidates for preparing efficient electrocatalysts. Since the activity, selectivity, and stability of a catalyst are the main factors to be evaluated, we provide a summary and outlook of the development of COF-based electrocatalysts from these aspects.

The selectivity of an electrocatalyst is mainly determined by the active sites and their surroundings, while the activity is governed by the types, electronic structures, and dispersity of active sites, as well as electron/substrate accessibility.

Multi-electron macrocycles (e.g., porphyrin and phthalocyanine), metal ions (e.g., Fe, Co, Ni, Ir, Ru, and even dual ions), and metallic nanoparticles (e.g., RuO, Ni_3N) as active sites have been introduced onto the skeleton or into the channels via building block design, post-synthetic modification, or in situ generation. The unique structural features of COFs ensure the atomic distribution of active sites like macrocycles and metal ions, while the predesignable and well-aligned channels can confine the formation of metallic nanoparticles in nano-sized diameters. Inherent electron conduction channels existing in the 2D COFs with π–π electron cloud overlap between the adjacent layers as well as the conjugated skeletons in both 2D and 3D COFs. To further alleviate the conductivity loss of bulk COFs caused by interfacial boundaries and disordered area, several efforts have been made, including physically mixing COFs with conductive components (e.g., carbon black), growing COFs on conductive materials (e.g., CNTs and graphene), preparing highly oriented thin COF films on electrodes, exfoliating bulk COFs into NSs, and pyrolyzing them into porous carbons. The large pore diameters, open and straight channels, and high porosity of COFs are favorable for mass transport; their pore structures and environment have been further modulated, and hierarchical structures have been prepared to facilitate reactant and product diffusion. Functional building units with electron-donating or -withdrawing properties have been introduced to tune their electronic structures.

Therefore, ideally, in a COF-catalyzed electrochemical reaction, favorite products can be obtained with high purity and low energy consumption. However, up to now, still remains a large room to increase the selectivity and activity of COF-based electrochemical reactions, including ORR, HER, OER, CO_2 reduction, and N_2 fixation.[330] In addition, although the stability of COFs and their performance are almost satisfactory for

electrochemical reaction, partial decomposition of the COF skeletons and leaching of metal ions have been found in acidic or alkaline test solutions.

To overcome these challenges, the following efforts are suggested: (1) thoroughly investigating their structure–function relationships via precise molecular design; (2) carefully tuning the surrounding environment of active sites that affects the adsorption, bond cleavage and formation, and desorption process; (3) exploring the reaction pathways and their influencing factors via experimental works and theoretical calculations; (4) preparing COFs and their NSs with high periodicity, fewer defects, and high orientation to promote their mass transport and charge transfer process; (6) increasing the loading and accessibility of active sites; (7) verifying their structure evolution after electrochemical processes; (8) increasing their stability under electrocatalytic conditions; (9) developing scalable production methods to reduce their cost.

Abbreviations

COFs	Covalent organic frameworks
EES	Electrochemical energy storage
EEC	Electrochemical energy conversion
2D	Two dimensional
3D	Three dimensional
NSs	Nanosheets
CTFs	Covalent triazine-based frameworks
CORFs	Covalent organic radical frameworks
FT-IR	Fourier Transform Infrared
OPA	o-Phthalaldehyde
DMF	N,N-Dimethylformamide
THF	Tetrahydrofuran
PXRD	Powder X-ray diffraction
AFM	Atomic Force Microscope
DLS	Dynamic light scattering
HRTEM	High-resolution transmission electron microscopy
TEM	Transmission electron microscopy
iCOFs	Ionic covalent organic frameworks
Py	4,4′,4″,4‴-(Pyrene-1,3,6,8-tetrayl)tetraaniline
SAED	Selected-area electron diffraction
TP	1,3,5-Triformylphloroglucinol
DANTB	2,7-Bis((E)-benzylideneamino)benzo[lmn][3,8]-phenanthroline-1,3,6,8(2H,7H)-tetraone
Tb	1,3,5-Triformylbenzene
CNTs	Carbon nanotubes
TEMPO	2,2,6,6-Tetramethylpiperidine-1-oxyl
LSBs	Lithium–sulfur batteries
PSs	Lithium polysulfides
BOC	Boron/oxygen co-doped porous carbon
XPS	X-ray photoelectron spectroscopy
^{1}H-NMR	^{1}H nuclear magnetic resonance
IR	Infrared spectra
LIBs	Lithium-ion batteries
SIBs	Sodium-ion batteries

δ_i	Ionic conductivity
t^+	Transference number (of Li^+)
γ-CD	γ-Cyclodextrin
EC	Ethylene carbonate
DMC	Dimethyl carbonate
PEG	Poly(ethylene oxide)
TPB	1,3,5-Tri(4-aminophenyl)benzene
BMTP	2,5-Bis((2-methoxyethoxy)methoxy)-terephthalaldehyde
DSC	Differential scanning calorimetry
PEMFC	Proton exchange membrane fuel cells
EB	Ethidium bromide
TAPB	1,3,5-Tris(4-aminophenyl)benzene
BTCA	1,3,5-Benzenetricarbaldehyde
RH	Relative humidity
SCs	Supercapacitors
EDLCs	Electrochemical double-layer capacitors
FS	Faradaic supercapacitors
DAAQ	2,6-Diaminoanthraquinone
PDC	1,4-Piperazinedicarboxaldehyde
MA	Melamine
NiP	5,10,15,20-Tetrakis(4′-tetraphenylamino)porphyrin
BPTA	2,5-Bis(2-propynyloxy)terephthalaldehyde
DMTA	2,5-Dimethoxyterephthalaldehyde
PVA	Poly(vinyl alcohol)
TFP	1,3,5-Triformylphloroglucinol
GIXD	Grazing incidence X-ray diffraction
CNF	Conductive carbon nanofiber
PEDOT	Poly(3,4-ethylenedioxythiophene)
BTT	Benzotrithiophene tricarbaldehyde
HOPG	Highly oriented pyrolytic graphite
sCOFs	Single-layered covalent organic frameworks
STM	Scanning tunneling microscopy
UHV	Ultrahigh vacuum
LAP	Laminar assembly polymerization
BDBA	1,4-Benzenediboronic acid
HHTP	2,3,6,7,10,11-Hexahydroxytriphenylene
TMC	Benzene-1,3,5-tricarbonyl trichloride
DFT	Density functional theory
4ATTF	Tetrathiafulvalene equipped with four benzaldehyde groups
PPDA	p-Phenylenediamine
SLG	Single-layer graphene
TBA	2,4,6-Trimethylbenzaldehyde
BII	Buffering interlayer interface
PTSA	Amine-p-toluene sulfonic acid
TTA	4,4′,4″-(1,3,5-Triazine-2,4,6-triyl)trianiline
DHTA	2,5-Dihydroxyterethaldehyde
ORR	Oxygen reduction reaction
HER	Hydrogen evolution reaction
OER	Oxygen evolution reaction
CO_2RR	CO_2 reduction reaction
RDS	Rate-determining step
NPMC	Non-precious metal catalysts
PTM	Polychlorotriphenylmethyl

PA	Phytic acid
SAC	Single-atom catalysts
η_{10}	Overpotential (at a current density of 10 mA cm^{-2})
j_0	Current density
TOF	Turnover frequency
FE	Faradaic efficiency
WOCs	Water-oxidizing complexes
Bpy	2,2′-Bipyridyl 5,5′-diamine
NPs	Nanoparticles
BDA	1,4-Benzenedicarboxaldehyde
ECR	Electrochemical reduction

Conflicts of interest

There are no conflicts to declare.

Acknowledgements

Notes and references

1 B. Dunn, H. Kamath and J. M. Tarascon, *Science*, 2011, **334**, 928–935.
2 N. S. Choi, Z. Chen, S. A. Freunberger, X. Ji, Y. K. Sun, K. Amine, G. Yushin, L. F. Nazar, J. Cho and P. G. Bruce, *Angew. Chem., Int. Ed.*, 2012, **51**, 9994–10024.
3 M. R. Lukatskaya, B. Dunn and Y. Gogotsi, *Nat. Commun.*, 2016, **7**, 12647.
4 C. X. Zu and H. Li, *Energy Environ. Sci.*, 2011, **4**, 2614–2624.
5 W. Xia, A. Mahmood, R. Q. Zou and Q. Xu, *Energy Environ. Sci.*, 2015, **8**, 1837–1866.
6 G. P. Wang, L. Zhang and J. J. Zhang, *Chem. Soc. Rev.*, 2012, **41**, 797–828.
7 Y. G. Wang, Y. F. Song and Y. Y. Xia, *Chem. Soc. Rev.*, 2016, **45**, 5925–5950.
8 L. Wang, Y. Z. Han, X. Feng, J. W. Zhou, P. F. Qi and B. Wang, *Coord. Chem. Rev.*, 2016, **307**, 361–381.
9 F. X. Wang, X. W. Wu, X. H. Yuan, Z. C. Liu, Y. Zhang, L. J. Fu, Y. S. Zhu, Q. M. Zhou, Y. P. Wu and W. Huang, *Chem. Soc. Rev.*, 2017, **46**, 6816–6854.
10 H. Y. Jin, C. X. Guo, X. Liu, J. L. Liu, A. Vasileff, Y. Jiao, Y. Zheng and S. Z. Qiao, *Chem. Rev.*, 2018, **118**, 6337–6408.
11 X. B. Cheng, C. Z. Zhao, Y. X. Yao, H. Liu and Q. Zhang, *Chem*, 2019, **5**, 74–96.
12 N. Chen, H. Q. Zhang, L. Li, R. J. Chen and S. J. Guo, *Adv. Energy Mater.*, 2018, **8**, 1702675.
13 Z. B. Liang, C. Qu, W. H. Guo, R. Q. Zou and Q. Xu, *Adv. Mater.*, 2018, **30**, 1702891.
14 Q. R. Fang, Z. B. Zhuang, S. Gu, R. B. Kaspar, J. Zheng, J. H. Wang, S. L. Qiu and Y. S. Yan, *Nat. Commun.*, 2014, **5**, 4503.

15 X. Feng, X. S. Ding and D. L. Jiang, *Chem. Soc. Rev.*, 2012, **41**, 6010–6022.

16 T. Y. Zhou, S. Q. Xu, Q. Wen, Z. F. Pang and X. Zhao, *J. Am. Chem. Soc.*, 2014, **136**, 15885–15888.

17 G. Zhang, M. Tsujimoto, D. Packwood, N. T. Duong, Y. Nishiyama, K. Kadota, S. Kitagawa and S. Horike, *J. Am. Chem. Soc.*, 2018, **140**, 2602–2609.

18 Z. F. Pang, T. Y. Zhou, R. R. Liang, Q. Y. Qi and X. Zhao, *Chem. Sci.*, 2017, **8**, 3866–3870.

19 R. W. Tilford, S. J. Mugavero, 3rd, P. J. Pellechia and J. J. Lavigne, *Adv. Mater.*, 2008, **20**, 2741–2746.

20 N. Huang, P. Wang and D. L. Jiang, *Nat. Rev. Mater.*, 2016, **1**, 16068.

21 S. Y. Ding and W. Wang, *Chem. Soc. Rev.*, 2013, **42**, 548–568.

22 S. Kandambeth, K. Dey and R. Banerjee, *J. Am. Chem. Soc.*, 2019, **141**, 1807–1822.

23 X. Y. Chen, K. Y. Geng, R. Y. Liu, K. T. Tan, Y. F. Gong, Z. P. Li, S. S. Tao, Q. H. Jiang and D. L. Jiang, *Angew. Chem., Int. Ed.*, 2019, **58**, 2–44.

24 Y. Gu, J. Zhao and J. A. Johnson, *Angew. Chem., Int. Ed.*, 2020, **59**, 2–30.

25 Y. F. Zeng, R. Q. Zou and Y. L. Zhao, *Adv. Mater.*, 2016, **28**, 2855–2873.

26 N. Huang, X. Chen, R. Krishna and D. L. Jiang, *Angew. Chem., Int. Ed.*, 2015, **54**, 2986–2990.

27 H. Furukawa and O. M. Yaghi, *J. Am. Chem. Soc.*, 2009, **131**, 8875–8883.

28 J. T. Yu, Z. Chen, J. L. Sun, Z. T. Huang and Q. Y. Zheng, *J. Mater. Chem.*, 2012, **22**, 5369–5373.

29 S. S. Yuan, X. Li, J. Y. Zhu, G. Zhang, P. Van Puyvelde and B. Van der Bruggen, *Chem. Soc. Rev.*, 2019, **48**, 2665–2681.

30 C. Zhang, B. H. Wu, M. Q. Ma, Z. K. Wang and Z. K. Xu, *Chem. Soc. Rev.*, 2019, **48**, 3811–3841.

31 X. Q. Zou and G. S. Zhu, *Adv. Mater.*, 2018, **30**, 1700750.

32 Z. Wang, S. Zhang, Y. Chen, Z. Zhang and S. Ma, *Chem. Soc. Rev.*, 2020, **49**, 708–735.

33 S. M. J. Rogge, A. Bavykina, J. Hajek, H. Garcia, A. I. Olivos-Suarez, A. Sepulveda-Escribano, A. Vimont, G. Clet, P. Bazin, F. Kapteijn, M. Daturi, E. V. Ramos-Fernandez, I. X. F. X. Llabres, V. Van Speybroeck and J. Gascon, *Chem. Soc. Rev.*, 2017, **46**, 3134–3184.

34 X. Chen, M. Addicoat, E. Jin, L. Zhai, H. Xu, N. Huang, Z. Q. Guo, L. L. Liu, S. Irle and D. L. Jiang, *J. Am. Chem. Soc.*, 2015, **137**, 3241–3247.

35 P. F. Wei, M. Z. Qi, Z. P. Wang, S. Y. Ding, W. Yu, Q. Liu, L. K. Wang, H. Z. Wang, W. K. An and W. Wang, *J. Am. Chem. Soc.*, 2018, **140**, 4623–4631.

36 T. Sick, A. G. Hufnagel, J. Kampmann, I. Kondofersky, M. Calik, J. M. Rotter, A. Evans, M. Doblinger, S. Herbert, K. Peters, D. Bohm, P. Knochel, D. D. Medina, D. Fattakhova-Rohlfing and T. Bein, *J. Am. Chem. Soc.*, 2018, **140**, 2085–2092.

37 S. Y. Ding, J. Gao, Q. Wang, Y. Zhang, W. G. Song, C. Y. Su and W. Wang, *J. Am. Chem. Soc.*, 2011, **133**, 19816–19822.

38 Y. Wang, A. Vogel, M. Sachs, R. S. Sprick, L. Wilbraham, S. J. A. Moniz, R. Godin, M. A. Zwijnenburg, J. R. Durrant, A. I. Cooper and J. Tang, *Nat. Energy*, 2019, **4**, 746–760.

39 S. Lin, C. S. Diercks, Y. B. Zhang, N. Kornienko, E. M. Nichols, Y. B. Zhao, A. R. Paris, D. Y. Kim, P. D. Yang, O. M. Yaghi and C. J. Chang, *Science*, 2015, **349**, 1208–1213.

40 H. Zhang, C. Li, M. Piszcz, E. Coya, T. Rojo, L. M. Rodriguez-Martinez, M. Armand and Z. Zhou, *Chem. Soc. Rev.*, 2017, **46**, 797–815.

41 S. Y. Ding, M. Dong, Y. W. Wang, Y. T. Chen, H. Z. Wang, C. Y. Su and W. Wang, *J. Am. Chem. Soc.*, 2016, **138**, 3031–3037.

42 X. Liu, D. Huang, C. Lai, G. Zeng, L. Qin, H. Wang, H. Yi, B. Li, S. Liu, M. Zhang, R. Deng, Y. Fu, L. Li, W. Xue and S. Chen, *Chem. Soc. Rev.*, 2019, **48**, 5266–5302.

43 S. L. Wang, L. Ma, Q. Y. Wang, P. P. Shao, D. Ma, S. Yuan, P. Lei, P. F. Li, X. Feng and B. Wang, *J. Mater. Chem. C*, 2018, **6**, 5369–5374.

44 L. Ma, X. Feng, S. Wang and B. Wang, *Mater. Chem. Front.*, 2017, **1**, 2474–2486.

45 Y. P. Song, Q. Sun, B. Aguila and S. Q. Ma, *Adv. Sci.*, 2019, **6**, 1801410.

46 M. S. Lohse and T. Bein, *Adv. Funct. Mater.*, 2018, **28**, 1705553.

47 P. P. Shao, J. Li, F. Chen, L. Ma, Q. B. Li, M. X. Zhang, J. W. Zhou, A. X. Yin, X. Feng and B. Wang, *Angew. Chem., Int. Ed.*, 2018, **57**, 16501–16505.

48 A. P. Côté, A. I. Benin, N. W. Ockwig, M. O'Keeffe, A. J. Matzger and O. M. Yaghi, *Science*, 2005, **310**, 1166–1170.

49 T. Q. Ma, K. A. Kapustin, S. X. Yin, L. Liang, Z. Y. Zhou, J. Niu, L. H. Li, Y. Y. Wang, J. Su, J. Li, X. G. Wang, W. D. Wang, W. Wang, J. L. Sun and O. M. Yaghi, *Science*, 2018, **361**, 48–52.

50 A. M. Evans, L. R. Parent, N. C. Flanders, R. P. Bisbey, E. Vitaku, M. S. Kirschner, R. D. Schaller, L. X. Chen, N. C. Gianneschi and W. R. Dichtel, *Science*, 2018, **361**, 52–57.

51 P. J. Waller, F. Gandara and O. M. Yaghi, *Acc. Chem. Res.*, 2015, **48**, 3053–3063.

52 E. Jin, M. Asada, Q. Xu, S. Dalapati, M. A. Addicoat, M. A. Brady, H. Xu, T. Nakamura, T. Heine, Q. H. Chen and D. L. Jiang, *Science*, 2017, **357**, 673–676.

53 H. M. El-Kaderi, J. R. Hunt, J. L. Mendoza-Cortés, A. P. Côté, R. E. Taylor, M. O'Keeffe and O. M. Yaghi, *Science*, 2007, **316**, 268–272.

54 S. C. Yan, X. Guan, H. Li, D. H. Li, M. Xue, Y. S. Yan, V. Valtchev, S. L. Qiu and Q. R. Fang, *J. Am. Chem. Soc.*, 2019, **141**, 2920–2924.

55 X. Guan, F. Chen, Q. Fang and S. Qiu, *Chem. Soc. Rev.*, 2020, **49**, 1357–1384.

56 K. Geng, T. He, R. Liu, K. T. Tan, Z. Li, S. Tao, Y. Gong, Q. Jiang and D. Jiang, *Chem. Rev.*, 2020, DOI: 10.1021/acs.chemrev.9b00550.

57 S. Patwardhan, A. A. Kocherzhenko, F. C. Grozema and L. D. A. Siebbeles, *J. Phys. Chem. C*, 2011, **115**, 11768–11772.

58 X. Feng, L. Liu, Y. Honsho, A. Saeki, S. Seki, S. Irle, Y. Dong, A. Nagai and D. Jiang, *Angew. Chem., Int. Ed.*, 2012, **51**, 2618–2622.

59 X. Feng, L. Chen, Y. Honsho, O. Saengsawang, L. L. Liu, L. Wang, A. Saeki, S. Irle, S. Seki, Y. P. Dong and D. L. Jiang, *Adv. Mater.*, 2012, **24**, 3026–3031.

60 S. Wan, F. G. Andara, A. Asano, H. Furukawa, A. Saeki, S. K. Dey, L. Liao, M. W. Ambrogio, Y. Y. Botros, X. F. Duan, S. Seki, J. F. Stoddart and O. M. Yaghi, *Chem. Mater.*, 2011, **23**, 4094–4097.

61 Y. Du, H. Yang, J. M. Whiteley, S. Wan, Y. Jin, S. H. Lee and W. Zhang, *Angew. Chem., Int. Ed.*, 2016, **55**, 1737–1741.

62 C. Y. Lin, D. Zhang, Z. Zhao and Z. Xia, *Adv. Mater.*, 2018, **30**, 1703646.

63 J. W. Zhou and B. Wang, *Chem. Soc. Rev.*, 2017, **46**, 6927–6945.

64 X. Gao, Y. Dong, S. W. Li, J. W. Zhou, L. Wang and B. Wang, *Electrochem. Energy Rev.*, 2020, **3**, 81–126.

65 B. N. Zheng, X. D. Lin, X. C. Zhang, D. C. Wu and K. Matyjaszewski, *Adv. Funct. Mater.*, 2019, DOI: 10.1002/adfm.201907006.

66 S. J. Kim, H. T. Wang and Y. M. Lee, *Angew. Chem., Int. Ed.*, 2019, **58**, 17512–17527.

67 H. Wang, Z. T. Zeng, P. Xu, L. S. Li, G. M. Zeng, R. Xiao, Z. Y. Tang, D. L. Huang, L. Tang, C. Lai, D. N. Jiang, Y. Liu, H. Yi, L. Qin, S. J. Ye, X. Y. Ren and W. W. Tang, *Chem. Soc. Rev.*, 2019, **48**, 488–516.

68 R. H. Dong, T. Zhang and X. L. Feng, *Chem. Rev.*, 2018, **118**, 6189–6235.

69 P. T. Xiao and Y. X. Xu, *J. Mater. Chem. A*, 2018, **6**, 21676–21695.

70 Z. K. Peng, H. M. Ding, R. F. Chen, C. Gao and C. Wang, *Acta Chim. Sin.*, 2019, **77**, 681–689.

71 W. Zheng, C. S. Tsang, L. Y. S. Lee and K. Y. Wong, *Mater. Today Chem.*, 2019, **12**, 34–60.

72 S. B. Alahakoon, C. M. Thompson, G. Occhialini and R. A. Smaldone, *ChemSusChem*, 2017, **10**, 2116–2129.

73 Y. Zhong, B. R. Cheng, C. Park, A. Ray, S. Brown, F. Mujid, J. U. Lee, H. Zhou, J. Suh, K. H. Lee, A. J. Mannix, K. Kang, S. J. Sibener, D. A. Muller and J. Park, *Science*, 2019, **366**, 1379–1384.

74 L. Grill, M. Dyer, L. Lafferentz, M. Persson, M. V. Peters and S. Hecht, *Nat. Nanotechnol.*, 2007, **2**, 687–691.

75 R. Gutzler, H. Walch, G. Eder, S. Kloft, W. M. Heckl and M. Lackinger, *Chem. Commun.*, 2009, 4456–4458.

76 M. Bieri, M. T. Nguyen, O. Gröning, J. M. Cai, M. Treier, K. Aït-Mansour, P. Ruffieux, C. A. Pignedoli, D. Passerone, M. Kastler, K. Müllen and R. Fasel, *J. Am. Chem. Soc.*, 2010, **132**, 16669–16676.

77 N. A. Zwaneveld, R. Pawlak, M. Abel, D. Catalin, D. Gigmes, D. Bertin and L. Porte, *J. Am. Chem. Soc.*, 2008, **130**, 6678–6679.

78 S. Schlögl, T. Sirtl, J. Eichhorn, W. M. Heckl and M. Lackinger, *Chem. Commun.*, 2011, **47**, 12355–12357.

79 O. Ourdjini, R. Pawlak, M. Abel, S. Clair, L. Chen, N. Bergeon, M. Sassi, V. Oison, J. M. Debierre, R. Coratger and L. Porte, *Phys. Rev. B: Condens. Matter Mater. Phys.*, 2011, **84**, 125421.

80 T. Faury, S. Clair, M. Abel, F. Dumur, D. Gigmes and L. Porte, *J. Phys. Chem. C*, 2012, **116**, 4819–4823.

81 S. Spitzer, A. Rastgoo-Lahrood, K. Macknapp, V. Ritter, S. Sotier, W. M. Heckl and M. Lackinger, *Chem. Commun.*, 2017, **53**, 5147–5150.

82 A. C. Marele, R. Mas-Ballesté, L. Terracciano, J. Rodríguez-Fernández, I. Berlanga, S. S. Alexandre, R. Otero, J. M. Gallego, F. Zamora and J. M. Gómez-Rodríguez, *Chem. Commun.*, 2012, **48**, 6779–6781.

83 B. Yang, J. Björk, H. P. Lin, X. Q. Zhang, H. M. Zhang, Y. Y. Li, J. Fan, Q. Li and L. F. Chi, *J. Am. Chem. Soc.*, 2015, **137**, 4904–4907.

84 C. Chen, T. Joshi, H. F. Li, A. D. Chavez, Z. Pedramrazi, P. N. Liu, H. Li, W. R. Dichtel, J. L. Bredas and M. F. Crommie, *ACS Nano*, 2018, **12**, 385–391.

85 S. Weigelt, C. Busse, C. Bombis, M. M. Knudsen, K. V. Gothelf, E. Lægsgaard, F. Besenbacher and T. R. Linderoth, *Angew. Chem., Int. Ed.*, 2008, **47**, 4406–4410.

86 Z. M. Gong, B. Yang, H. P. Lin, Y. Y. Tang, Z. Y. Tang, J. J. Zhang, H. M. Zhang, Y. Y. Li, Y. S. Xie, Q. Li and L. F. Chi, *ACS Nano*, 2016, **10**, 4228–4235.

87 T. Joshi, C. Chen, H. F. Li, C. S. Diercks, G. Q. Wang, P. J. Waller, H. Li, J. L. Bredas, O. M. Yaghi and M. F. Crommie, *Adv. Mater.*, 2019, **31**, 1805941.

88 J. C. Russell, M. O. Blunt, J. M. Garfitt, D. J. Scurr, M. Alexander, N. R. Champness and P. H. Beton, *J. Am. Chem. Soc.*, 2011, **133**, 4220–4223.

89 C. Z. Guan, D. Wang and L. J. Wan, *Chem. Commun.*, 2012, **48**, 2943–2945.

90 R. Tanoue, R. Higuchi, N. Enoki, Y. Miyasato, S. Uemura, N. Kimizuka, A. Z. Stieg, J. K. Gimzewski and M. Kunitake, *ACS Nano*, 2011, **5**, 3923–3929.

91 J. F. Dienstmaier, D. D. Medina, M. Dogru, P. Knochel, T. Bein, W. M. Heckl and M. Lackinger, *ACS Nano*, 2012, **6**, 7234–7242.

92 J. Y. Yue, X. H. Liu, B. Sun and D. Wang, *Chem. Commun.*, 2015, **51**, 14318–14321.

93 W. L. Dong, L. Wang, H. M. Ding, L. Zhao, D. Wang, C. Wang and L. J. Wan, *Langmuir*, 2015, **31**, 11755–11759.

94 J. Y. Yue, M. Markoulides, A. C. Regan, S. Y. Li, N. Chronakis, A. Gourdon, T. Chen, H. J. Yan and D. Wang, *Chem. Commun.*, 2017, **53**, 428–431.

95 Y. X. Yu, J. B. Lin, Y. Wang, Q. D. Zeng and S. B. Lei, *Chem. Commun.*, 2016, **52**, 6609–6612.

96 L. Yu, Z. B. Li and D. Wang, *Chem. Commun.*, 2016, **52**, 13771–13774.

97 Y. P. Mo, X. H. Liu and D. Wang, *ACS Nano*, 2017, **11**, 11694–11700.

98 L. M. Wang, J. Y. Yue, X. Y. Cao and D. Wang, *Langmuir*, 2019, **35**, 6333–6339.

99 X. H. Liu, C. Z. Guan, S. Y. Ding, W. Wang, H. J. Yan, D. Wang and L. J. Wan, *J. Am. Chem. Soc.*, 2013, **135**, 10470–10474.

100 J. Y. Yue, Y. P. Mo, S. Y. Li, W. L. Dong, T. Chen and D. Wang, *Chem. Sci.*, 2017, **8**, 2169–2174.

101 C. X. Wang, J. L. Chen, C. H. Shu, K. J. Shi and P. N. Liu, *Phys. Chem. Chem. Phys.*, 2019, **21**, 13222–13229.

102 D. Cui, J. M. MacLeod, M. Ebrahimi, D. F. Perepichka and F. Rosei, *Chem. Commun.*, 2015, **51**, 16510–16513.

103 D. L. Cui, J. M. MacLeod and F. Rosei, *Small*, 2019, **15**, 1903294.

This journal is © The Royal Society of Chemistry 2020

Chem. Soc. Rev., 2020, **49**, 3565–3604 | **3599**

104 X. H. Liu, C. Z. Guan, Q. N. Zheng, D. Wang and L. J. Wan, *J. Chem. Phys.*, 2015, **142**, 101905.

105 J. F. Dienstmaier, A. M. Gigler, A. J. Goetz, P. Knochel, T. Bein, A. Lyapin, S. Reichlmaier, W. M. Heckl and M. Lackinger, *ACS Nano*, 2011, **5**, 9737–9745.

106 L. R. Xu, X. Zhou, Y. X. Yu, W. Q. Tian, J. Ma and S. B. Lei, *ACS Nano*, 2013, **7**, 8066–8073.

107 C. Lu, Y. Li, L. M. Wang, H. J. Yan, L. Chen and D. Wang, *Chem. Commun.*, 2019, **55**, 1326–1329.

108 L. R. Xu, X. Zhou, W. Q. Tian, T. Gao, Y. F. Zhang, S. B. Lei and Z. F. Liu, *Angew. Chem., Int. Ed.*, 2014, **53**, 9564–9568.

109 Q. T. Fan, C. C. Wang, Y. Han, J. F. Zhu, W. Hieringer, J. Kuttner, G. Hilt and J. M. Gottfried, *Angew. Chem., Int. Ed.*, 2013, **52**, 4668–4672.

110 X. H. Liu, Y. P. Mo, J. Y. Yue, Q. N. Zheng, H. J. Yan, D. Wang and L. J. Wan, *Small*, 2014, **10**, 4934–4939.

111 C. L. Tan, X. H. Cao, X. J. Wu, Q. Y. He, J. Yang, X. Zhang, J. Z. Chen, W. Zhao, S. K. Han, G. H. Nam, M. Sindoro and H. Zhang, *Chem. Rev.*, 2017, **117**, 6225–6331.

112 J. Sun, A. Klechikov, C. Moise, M. Prodana, M. Enachescu and A. V. Talyzin, *Angew. Chem., Int. Ed.*, 2018, **57**, 1034–1038.

113 M. S. Kim, W. J. Lee, S. M. Paek and J. K. Park, *ACS Appl. Mater. Interfaces*, 2018, **10**, 32102–32111.

114 S. Park, M. S. Kim, W. Jang, J. K. Park and D. H. Wang, *Nanoscale*, 2018, **10**, 4708–4717.

115 B. Sun, C. H. Zhu, Y. Liu, C. Wang, L. J. Wan and D. Wang, *Chem. Mater.*, 2017, **29**, 4367–4374.

116 M. L. Xu, L. Y. Wang, Y. Xie, Y. H. Song and L. Wang, *Sens. Actuators, B*, 2019, **281**, 1009–1015.

117 S. Y. Kim and H. C. Choi, *Chem. Commun.*, 2019, **2**, 60.

118 H. Huang, F. M. Li, Y. Zhang and Y. Chen, *J. Mater. Chem. A*, 2019, **7**, 5575–5582.

119 W. B. Liu, X. K. Li, C. M. Wang, H. H. Pan, W. P. Liu, K. Wang, Q. D. Zeng, R. M. Wang and J. Z. Jiang, *J. Am. Chem. Soc.*, 2019, **141**, 17431–17440.

120 J. W. Colson, A. R. Woll, A. Mukherjee, M. P. Levendorf, E. L. Spitler, V. B. Shields, M. G. Spencer, J. Park and W. R. Dichtel, *Science*, 2011, **332**, 228–231.

121 X. D. Chen, H. Zhang, C. G. Ci, W. W. Sun and Y. Wang, *ACS Nano*, 2019, **13**, 3600–3607.

122 W. Y. Dai, F. Shao, J. Szczerbiński, R. McCaffrey, R. Zenobi, Y. H. Jin, A. D. Schlüter and W. Zhang, *Angew. Chem., Int. Ed.*, 2016, **55**, 213–217.

123 J. I. Feldblyum, C. H. McCreery, S. C. Andrews, T. Kurosawa, E. J. Santos, V. Duong, L. Fang, A. L. Ayzner and Z. N. Bao, *Chem. Commun.*, 2015, **51**, 13894–13897.

124 S. Y. Kim, H. Lim, J. Lee and H. C. Choi, *Langmuir*, 2018, **34**, 8731–8738.

125 T. Zhang, H. Y. Qi, Z. Q. Liao, Y. D. Horev, L. A. Panes-Ruiz, P. S. Petkov, Z. Zhang, R. Shivhare, P. P. Zhang, K. J. Liu, V. Bezugly, S. H. Liu, Z. K. Zheng, S. Mannsfeld, T. Heine, G. Cuniberti, H. Haick, E. Zschech, U. Kaiser, R. H. Dong and X. L. Feng, *Nat. Commun.*, 2019, **10**, 4225.

126 K. J. Liu, H. Y. Qi, R. H. Dong, R. Shivhare, M. Addicoat, T. Zhang, H. Sahabudeen, T. Heine, S. Mannsfel, U. Kaiser, Z. K. Zheng and X. L. Feng, *Nat. Chem.*, 2019, **11**, 994–1000.

127 H. Sahabudeen, H. Y. Qi, M. Ballabio, M. Položij, S. Olthof, R. Shivhare, Y. Jing, S. Park, K. J. Liu, T. Zhang, J. Ma, B. Rellinghaus, S. Mannsfeld, T. Heine, M. Bonn, E. Cμnovas, Z. K. Zheng, U. Kaiser, R. H. Dong and X. L. Feng, *Angew. Chem., Int. Ed.*, 2020, **59**, 2–11.

128 S. Park, Z. Q. Liao, B. Ibarlucea, H. Y. Qi, H. H. Lin, D. Becker, J. Melidonie, T. Zhang, H. Sahabudeen, L. Baraban, C. Baek, Z. K. Zheng, E. Zschech, A. Fery, T. Heine, U. Kaiser, G. Cuniberti, R. H. Dong and X. L. Feng, *Angew. Chem., Int. Ed.*, 2020, DOI: 10.1002/anie.201916595.

129 Y. Li, M. C. Zhang, X. H. Guo, R. Wen, X. Li, X. F. Li, S. J. Li and L. J. Ma, *Nanoscale Horiz.*, 2018, **3**, 205–212.

130 K. Dey, M. Pal, K. C. Rout, H. S. Kunjattu, A. Das, R. Mukherjee, U. K. Kharul and R. Banerjee, *J. Am. Chem. Soc.*, 2017, **139**, 13083–13091.

131 Z. F. Wang, Q. Yu, Y. B. Huang, H. D. An, Y. Zhao, Y. F. Feng, X. Li, X. L. Shi, J. J. Liang, F. S. Pan, P. Cheng, Y. Chen, S. Q. Ma and Z. J. Zhang, *ACS Cent. Sci.*, 2019, **5**, 1352–1359.

132 J. J. Liu, W. Zan, K. Li, Y. Yang, F. X. Bu and Y. X. Xu, *J. Am. Chem. Soc.*, 2017, **139**, 11666–11669.

133 Q. Hao, C. Q. Zhao, B. Sun, C. Lu, J. Liu, M. J. Liu, L. J. Wan and D. Wang, *J. Am. Chem. Soc.*, 2018, **140**, 12152–12158.

134 S. Chandra, S. Kandambeth, B. P. Biswal, B. Lukose, S. M. Kunjir, M. Chaudhary, R. Babarao, T. Heine and R. Banerjee, *J. Am. Chem. Soc.*, 2013, **135**, 17853–17861.

135 W. R. Cui, C. R. Zhang, W. Jiang, R. P. Liang, S. H. Wen, D. Peng and J. D. Qiu, *ACS Sustainable Chem. Eng.*, 2019, **7**, 9408–9415.

136 G. H. Liu, Z. Y. Jiang, H. Yang, C. D. Li, H. J. Wang, M. D. Wang, Y. M. Song, H. Wu and F. S. Pan, *J. Membr. Sci.*, 2019, **572**, 557–566.

137 S. Wang, Q. Y. Wang, P. P. Shao, Y. Z. Han, X. Gao, L. Ma, S. Yuan, X. J. Ma, J. W. Zhou, X. Feng and B. Wang, *J. Am. Chem. Soc.*, 2017, **139**, 4258–4261.

138 X. W. Mu, J. Zhan, X. M. Feng, B. H. Yuan, S. L. Qiu, L. Song and Y. Hu, *ACS Appl. Mater. Interfaces*, 2017, **9**, 23017–23026.

139 M. R. Rao, Y. Fang, S. De Feyter and D. F. Perepichka, *J. Am. Chem. Soc.*, 2017, **139**, 2421–2427.

140 D. N. Bunck and W. R. Dichtel, *J. Am. Chem. Soc.*, 2013, **135**, 14952–14955.

141 Y. W. Peng, Y. Huang, Y. H. Zhu, B. Chen, L. Y. Wang, Z. C. Lai, Z. C. Zhang, M. T. Zhao, C. L. Tan, N. L. Yang, F. W. Shao, Y. Han and H. Zhang, *J. Am. Chem. Soc.*, 2017, **139**, 8698–8704.

142 J. Q. Dong, X. Li, S. B. Peh, Y. Yuan, D. Y. X. Wang, D. D. Ji, S. J. Peng, G. L. Liu, S. M. Ying, D. Q. Yuan, J. W. Jiang, S. Ramakrishna and D. Zhao, *Chem. Mater.*, 2018, **31**, 146–160.

143 K. Wang, Z. Zhang, L. Lin, J. Chen, K. Hao, H. Y. Tian and X. S. Chen, *Chem. Mater.*, 2019, **31**, 3313–3323.

144 G. Das, B. P. Biswal, S. Kandambeth, V. Venkatesh, G. Kaur, M. Addicoat, T. Heine, S. Verma and R. Banerjee, *Chem. Sci.*, 2015, **6**, 3931–3939.

3600 | *Chem. Soc. Rev.*, 2020, **49**, 3565–3604

This journal is © The Royal Society of Chemistry 2020

145 P. Wang, F. Zhou, C. Zhang, S. Y. Yin, L. L. Teng, L. L. Chen, X. X. Hu, H. W. Liu, X. Yin and X. B. Zhang, *Chem. Sci.*, 2018, **9**, 8402–8408.

146 S. J. Gan, X. N. Tong, Y. Zhang, J. H. Wu, Y. Q. Hu and A. H. Yuan, *Adv. Funct. Mater.*, 2019, **29**, 1902757.

147 W. R. Cui, C. R. Zhang, W. Jiang, R. P. Liang and J. D. Qiu, *ACS Appl. Nano Mater.*, 2019, **2**, 5342–5349.

148 C. L. Zhang, S. M. Zhang, Y. H. Yan, F. Xia, A. N. Huang and Y. Z. Xian, *ACS Appl. Mater. Interfaces*, 2017, **9**, 13415–13421.

149 G. Das, F. Benyettou, S. K. Sharma, S. K. Sharama, T. Prakasam, F. Gandara, V. A. de la Pena-O'Shea, N. Saleh, R. Pasricha, R. Jagannathan, M. A. Olson and A. Trabolsi, *Chem. Sci.*, 2018, **9**, 8382–8387.

150 S. Mitra, S. Kandambeth, B. P. Biswal, M. A. Khayum, C. K. Choudhury, M. Mehta, G. Kaur, S. Banerjee, A. Prabhune, S. Verma, S. Roy, U. K. Kharul and R. Banerjee, *J. Am. Chem. Soc.*, 2016, **138**, 2823–2828.

151 N. Zhang, T. S. Wang, X. Wu, C. Jiang, F. Chen, W. Bai and R. Bai, *RSC Adv.*, 2018, **8**, 3803–3808.

152 P. Peng, L. Shi, F. Huo, S. J. Zhang, C. X. Mi, Y. H. Cheng and Z. H. Xiang, *ACS Nano*, 2019, **13**, 878–884.

153 H. W. Chen, H. Y. Tu, C. J. Hu, Y. Liu, D. R. Dong, Y. F. Sun, Y. F. Dai, S. L. Wang, H. Qian, Z. Y. Lin and L. W. Chen, *J. Am. Chem. Soc.*, 2018, **140**, 896–899.

154 A. Mal, R. K. Mishra, V. K. Praveen, M. A. Khayum, R. Banerjee and A. Ajayaghosh, *Angew. Chem., Int. Ed.*, 2018, **57**, 8443–8447.

155 L. L. Wang, C. Zeng, H. Xu, P. C. Yin, D. C. Chen, J. Deng, M. Li, N. Zheng, C. Gu and Y. G. Ma, *Chem. Sci.*, 2019, **10**, 1023–1028.

156 M. A. Khayum, S. Kandambeth, S. Mitra, S. B. Nair, A. Das, S. S. Nagane, R. Mukherjee and R. Banerjee, *Angew. Chem., Int. Ed.*, 2016, **55**, 15604–15608.

157 Z. Y. Fan, K. Nomura, M. S. Zhu, X. X. Li, J. W. Xue, T. Majima and Y. Osakada, *Chem. Commun.*, 2019, **2**, 55.

158 S. Mitra, H. S. Sasmal, T. Kundu, S. Kandambeth, K. Illath, D. Diaz Diaz and R. Banerjee, *J. Am. Chem. Soc.*, 2017, **139**, 4513–4520.

159 M. D. Wang, F. S. Pan, H. Yang, Y. Cao, H. J. Wang, Y. M. Song, Z. Lu, M. Z. Sun, H. Wu and Z. Y. Jiang, *J. Mater. Chem. A*, 2019, **7**, 9912–9923.

160 Y. G. Zhang, M. X. Tan, H. Li, Y. G. Zheng, S. J. Gao, H. Zhang and J. Y. Ying, *Chem. Commun.*, 2011, **47**, 7365–7367.

161 D. W. Burke, C. Sun, I. Castano, N. C. Flanders, A. M. Evans, E. Vitaku, D. C. McLeod, R. H. Lambeth, L. X. Chen, N. C. Gianneschi and W. R. Dichtel, *Angew. Chem., Int. Ed.*, 2020, **59**, 5165.

162 X. J. Zhan, Z. Chen and Q. C. Zhang, *J. Mater. Chem. A*, 2017, **5**, 14463–14479.

163 M. Y. Wang, H. Guo, R. Xue, Q. Li, H. Liu, N. Wu, W. Q. Yao and W. Yang, *ChemElectroChem*, 2019, **6**, 2984.

164 D. H. Yang, Z. Q. Yao, D. H. Wu, Y. H. Zhang, Z. Y. Zhou and X. H. Bu, *J. Mater. Chem. A*, 2016, **4**, 18621–18627.

165 J. Q. Lv, Y. X. Tan, J. F. Xie, R. Yang, M. X. Yu, S. S. Sun, M. D. Li, D. Q. Yuan and Y. B. Wang, *Angew. Chem., Int. Ed.*, 2018, **57**, 12716–12720.

166 S. Q. Xu, G. Wang, B. P. Biswal, M. Addicoat, S. Paasch, W. B. Sheng, X. D. Zhuang, E. Brunner, T. Heine, R. Berger and X. L. Feng, *Angew. Chem., Int. Ed.*, 2019, **58**, 849–853.

167 F. Xu, S. B. Jin, H. Zhong, D. C. Wu, X. Q. Yang, X. Chen, H. Wei, R. W. Fu and D. L. Jiang, *Sci. Rep.*, 2015, **5**, 8225.

168 Z. Q. Luo, L. J. Liu, J. X. Ning, K. X. Lei, Y. Lu, F. J. Li and J. Chen, *Angew. Chem., Int. Ed.*, 2018, **57**, 9443–9446.

169 G. Wang, N. Chandrasekhar, B. P. Biswal, D. Becker, S. Paasch, E. Brunner, M. Addicoat, M. H. Yu, R. Berger and X. L. Feng, *Adv. Mater.*, 2019, **31**, 1901478.

170 R. Fang, S. Zhao, Z. Sun, D. W. Wang, H. M. Cheng and F. Li, *Adv. Mater.*, 2017, **29**, 1606823.

171 P. G. Bruce, S. A. Freunberger, L. J. Hardwick and J. M. Tarascon, *Nat. Mater.*, 2011, **11**, 19–29.

172 Z. Cheng, H. Pan, H. Zhong, Z. Xiao, X. Li and R. Wang, *Adv. Funct. Mater.*, 2018, **28**, 1707597.

173 H. P. Liao, H. M. Ding, B. J. Li, X. P. Ai and C. Wang, *J. Mater. Chem. A*, 2014, **2**, 8854–8858.

174 H. P. Liao, H. M. Wang, H. M. Ding, X. S. Meng, H. Xu, B. S. Wang, X. P. Ai and C. Wang, *J. Mater. Chem. A*, 2016, **4**, 7416–7421.

175 Y. Meng, G. Q. Lin, H. M. Ding, H. P. Liao and C. Wang, *J. Mater. Chem. A*, 2018, **6**, 17186–17191.

176 Z. A. Ghazi, L. Y. Zhu, H. Wang, A. Naeem, A. M. Khattak, B. Liang, N. A. Khan, Z. X. Wei, L. S. Li and Z. Y. Tang, *Adv. Energy Mater.*, 2016, **6**, 1601250.

177 X. D. Chen, Y. J. Xu, F. H. Du and Y. Wang, *Small Methods*, 2019, **3**, 1900338.

178 Z. C. Xiao, D. B. Kong, Q. Song, S. K. Zhou, Y. B. Zhang, A. Badshah, J. X. Liang and L. J. Zhi, *Nano Energy*, 2018, **46**, 365–371.

179 Q. Jiang, Y. S. Li, X. X. Zhao, P. X. Xiong, X. Yu, Y. H. Xu and L. Chen, *J. Mater. Chem. A*, 2018, **6**, 17977–17981.

180 D. G. Wang, N. Li, Y. M. Hu, S. Wan, M. Song, G. Yu, Y. H. Jin, W. F. Wei, K. Han, G. C. Kuang and W. Zhang, *ACS Appl. Mater. Interfaces*, 2018, **10**, 42233–42240.

181 F. Xu, S. H. Yang, X. Chen, Q. H. Liu, H. J. Li, H. Q. Wang, B. Q. Wei and D. L. Jiang, *Chem. Sci.*, 2019, **10**, 6001–6006.

182 L. Y. Bai, Q. Gao and Y. L. Zhao, *J. Mater. Chem. A*, 2016, **4**, 14106–14110.

183 S. Huang, D. Chen, C. Meng, S. Wang, S. Ren, D. Han, M. Xiao, L. Sun and Y. Meng, *Small*, 2019, **15**, 1904830.

184 S. Haldar, K. Roy, S. Nandi, D. Chakraborty, D. Puthusseri, Y. Gawli, S. Ogale and R. Vaidhyanathan, *Adv. Energy Mater.*, 2018, **8**, 1702170.

185 Z. D. Lei, X. D. Chen, W. W. Sun, Y. Zhang and Y. Wang, *Adv. Energy Mater.*, 2019, **9**, 1801010.

186 J. J. Liu, P. B. Lyu, Y. Zhang, P. Nachtigall and Y. X. Xu, *Adv. Mater.*, 2018, **30**, 1705401.

187 B. C. Patra, S. K. Das, A. Ghosh, K. A. Raj, P. Moitra, M. Addicoat, S. Mitra, A. Bhaumik, S. Bhattacharya and A. Pradhan, *J. Mater. Chem. A*, 2018, **6**, 16655–16663.

188 S. Gu, S. F. Wu, L. J. Cao, M. C. Li, N. Qin, J. Zhu, Z. Q. Wang, Y. Z. Li, Z. Q. Li, J. J. Chen and Z. G. Lu, *J. Am. Chem. Soc.*, 2019, **141**, 9623–9628.

This journal is © The Royal Society of Chemistry 2020

Chem. Soc. Rev., 2020, **49**, 3565–3604 | 3601

189 Z. D. Lei, Q. S. Yang, S. Y. Guo, W. W. Sun, H. Liu, L. P. Lv, Y. Zhang and Y. Wang, *Nat. Commun.*, 2018, **9**, 576.

190 X. D. Chen, Y. S. Li, L. Wang, Y. Xu, A. Nie, Q. Q. Li, F. Wu, W. W. Sun, X. Zhang, R. Vajtai, P. M. Ajayan, L. Chen and Y. Wang, *Adv. Mater.*, 2019, **31**, 1901640.

191 S. Feng, H. Xu, C. Zhang, Y. Chen, J. H. Zeng, D. L. Jiang and J. X. Jiang, *Chem. Commun.*, 2017, **53**, 11334–11337.

192 J. S. Wu, S. F. Wu, M. C. Li, H. Phan, D. G. Wang, T. S. Herng, J. Ding and Z. G. Lu, *Angew. Chem., Int. Ed.*, 2018, **57**, 8007–8011.

193 Z. Wang, Y. Li, P. Liu, Q. Qi, F. Zhang, G. Lu, X. Zhao and X. Huang, *Nanoscale*, 2019, **11**, 5330–5335.

194 C. J. Yao, Z. Wu, J. Xie, F. Yu, W. Guo, Z. J. Xu, D. S. Li, S. Zhang and Q. Zhang, *ChemSusChem*, 2019, **12**, 1–8.

195 E. Vitaku, C. N. Gannett, K. L. Carpenter, L. Shen, H. D. Abruna and W. R. Dichtel, *J. Am. Chem. Soc.*, 2020, **142**, 16–20.

196 X. F. Yang, B. Dong, H. Z. Zhang, R. Ge, Y. A. Gao and H. M. Zhang, *RSC Adv.*, 2015, **5**, 86137–86143.

197 X. Zhang, Z. Wang, L. Yao, Y. Y. Mai, J. Q. Liu, X. L. Hua and H. Wei, *Mater. Lett.*, 2018, **213**, 143–147.

198 D. G. Wang, Y. Wang, M. Song, G. C. Kuang and K. Han, *Chem. Commun.*, 2019, **55**, 13247–13250.

199 J. Y. Wang, L. P. Si, Q. Wei, X. J. Hong, L. G. Lin, X. Li, J. Y. Chen, P. B. Wen and Y. P. Cai, *J. Energy Chem.*, 2019, **28**, 54–60.

200 Z. Yang, C. Peng, R. Meng, L. Zu, Y. Feng, B. Chen, Y. Mi, C. Zhang and J. Yang, *ACS Cent. Sci.*, 2019, **5**, 1876–1883.

201 A. Manthiram, X. Yu and S. Wang, *Nat. Rev. Mater.*, 2017, **2**, 16103.

202 Q. Zhao, S. Stalin, C. Z. Zhao and L. A. Archer, *Nat. Rev. Mater.*, 2020, **5**, 229–252.

203 Y. Y. Zhang, J. Y. Duan, D. Ma, P. F. Li, S. W. Li, H. W. Li, J. W. Zhou, X. J. Ma, X. Feng and B. Wang, *Angew. Chem., Int. Ed.*, 2017, **56**, 16313–16317.

204 Q. Xu, S. S. Tao, Q. H. Jiang and D. L. Jiang, *J. Am. Chem. Soc.*, 2018, **140**, 7429–7432.

205 Z. B. Guo, Y. Y. Zhang, Y. Dong, J. Li, S. W. Li, P. P. Shao, X. Feng and B. Wang, *J. Am. Chem. Soc.*, 2019, **141**, 1923–1927.

206 Z. Xie, B. Wang, Z. F. Yang, X. Yang, X. Yu, G. L. Xing, Y. H. Zhang and L. Chen, *Angew. Chem., Int. Ed.*, 2019, **58**, 15742–15746.

207 G. Zhang, Y. L. Hong, Y. Nishiyama, S. Y. Bai, S. Kitagawa and S. Horike, *J. Am. Chem. Soc.*, 2018, **141**, 1227–1234.

208 Y. M. Hu, N. Dunlap, S. Wan, S. L. Lu, S. F. Huang, L. Sellinger, M. Ortiz, Y. H. Jin, S. H. Lee and W. Zhang, *J. Am. Chem. Soc.*, 2019, **141**, 7518–7525.

209 K. H. Jeong, S. Park, G. Y. Jung, S. H. Kim, Y. H. Lee, S. K. Kwak and S. Y. Lee, *J. Am. Chem. Soc.*, 2019, **141**, 5880–5885.

210 D. A. Vazquez-Molina, G. S. Mohammad-Pour, C. Lee, M. W. Logan, X. F. Duan, J. K. Harper and F. J. Uribe-Romo, *J. Am. Chem. Soc.*, 2016, **138**, 9767–9770.

211 C. Montoro, D. Rodriguez-San-Miguel, E. Polo, R. Escudero-Cid, M. L. Ruiz-Gonzalez, J. A. R. Navarro, P. Ocon and F. Zamora, *J. Am. Chem. Soc.*, 2017, **139**, 10079–10086.

212 H. Xu, S. S. Tao and D. L. Jiang, *Nat. Mater.*, 2016, **15**, 722–726.

213 D. B. Shinde, H. B. Aiyappa, M. Bhadra, B. P. Biswal, P. Wadge, S. Kandambeth, B. Garai, T. Kundu, S. Kurungot and R. Banerjee, *J. Mater. Chem. A*, 2016, **4**, 2682–2690.

214 H. P. Ma, B. L. Liu, B. Li, L. M. Zhang, Y. G. Li, H. Q. Tan, H. Y. Zang and G. S. Zhu, *J. Am. Chem. Soc.*, 2016, **138**, 5897–5903.

215 S. Chandra, T. Kundu, K. Dey, M. Addicoat, T. Heine and R. Banerjee, *Chem. Mater.*, 2016, **28**, 1489–1494.

216 Y. W. Peng, G. D. Xu, Z. G. Hu, Y. D. Cheng, C. L. Chi, D. Q. Yuan, H. S. Cheng and D. Zhao, *ACS Appl. Mater. Interfaces*, 2016, **8**, 18505–18512.

217 M. Z. A. Aykanat and K. A. Mirica, *Chem. Mater.*, 2018, **31**, 819–825.

218 H. Zhong, Z. H. Fu, J. M. Taylor, G. Xu and R. H. Wang, *Adv. Funct. Mater.*, 2017, **27**, 1701465.

219 W. F. Kong, W. Jia, R. Wang, Y. F. Gong, C. C. Wang, P. Y. Wu and J. Guo, *Chem. Commun.*, 2019, **55**, 75–78.

220 H. S. Sasmal, H. B. Aiyappa, S. N. Bhange, S. Karak, A. Halder, S. Kurungot and R. Banerjee, *Angew. Chem., Int. Ed.*, 2018, **57**, 10894–10898.

221 C. Jiang, M. Tang, S. L. Zhu, J. D. Zhang, Y. C. Wu, Y. Chen, C. Xia, C. L. Wang and W. P. Hu, *Angew. Chem., Int. Ed.*, 2018, **57**, 16072–16076.

222 Y. Yang, X. J. Hong, C. L. Song, L. H. Li, Y. X. Zheng, D. D. Zhou, M. Zhang, Y. P. Cai and H. X. Wang, *J. Mater. Chem. A*, 2019, **7**, 16323–16329.

223 J. Yoo, S. J. Cho, G. Y. Jung, S. H. Kim, K. H. Choi, J. H. Kim, C. K. Lee, S. K. Kwak and S. Y. Lee, *Nano Lett.*, 2016, **16**, 3292–3300.

224 Q. Xu, K. L. Zhang, J. Qian, Y. Guo, X. K. Song, H. L. Pan, D. Wang and X. P. Li, *ACS Appl. Energy Mater.*, 2019, **2**, 5793–5798.

225 C. R. DeBlase, K. E. Silberstein, T. T. Truong, H. D. Abruña and W. R. Dichtel, *J. Am. Chem. Soc.*, 2013, **135**, 16821–16824.

226 S. Chandra, D. Roy Chowdhury, M. Addicoat, T. Heine, A. Paul and R. Banerjee, *Chem. Mater.*, 2017, **29**, 2074–2080.

227 L. Li, F. Lu, R. Xue, B. L. Ma, Q. Li, N. Wu, H. Liu, W. Q. Yao, H. Guo and W. Yang, *ACS Appl. Mater. Interfaces*, 2019, **11**, 26355–26363.

228 F. Xu, H. Xu, X. Chen, D. C. Wu, Y. Wu, H. Liu, C. Gu, R. W. Fu and D. L. Jiang, *Angew. Chem., Int. Ed.*, 2015, **54**, 6814–6818.

229 A. Halder, M. Ghosh, M. A. Khayum, S. Bera, M. Addicoat, H. S. Sasmal, S. Karak, S. Kurungot and R. Banerjee, *J. Am. Chem. Soc.*, 2018, **140**, 10941–10945.

230 M. A. Khayum, V. Vijayakumar, S. Karak, S. Kandambeth, M. Bhadra, K. Suresh, N. Acharambath, S. Kurungot and R. Banerjee, *ACS Appl. Mater. Interfaces*, 2018, **10**, 28139–28146.

231 W. Liu, M. Ulaganathan, I. Abdelwahab, X. Luo, Z. X. Chen, S. J. Rong Tan, X. W. Wang, Y. P. Liu, D. C. Geng, Y. Bao, J. Y. Chen and K. P. Loh, *ACS Nano*, 2017, **12**, 852–860.

232 A. F. M. El-Mahdy, Y. H. Hung, T. H. Mansoure, H. H. Yu, T. Chen and S. W. Kuo, *Chem. – Asian J.*, 2019, **14**, 1429–1435.

3602 | *Chem. Soc. Rev.*, 2020, **49**, 3565–3604

This journal is © The Royal Society of Chemistry 2020

233 A. Roy, S. Mondal, A. Halder, A. Banerjee, D. Ghoshal, A. Paul and S. Malik, *Eur. Polym. J.*, 2017, **93**, 448–457.

234 A. F. M. El-Mahdy, C.-H. Kuo, A. Alshehri, C. Young, Y. Yamauchi, J. Kim and S.-W. Kuo, *J. Mater. Chem. A*, 2018, **6**, 19532–19541.

235 S. K. Das, K. Bhunia, A. Mallick, A. Pradhan, D. Pradhan and A. Bhaumik, *Microporous Mesoporous Mater.*, 2018, **266**, 109–116.

236 A. F. M. El-Mahdy, C. Young, J. Kim, J. You, Y. Yamauchi and S. W. Kuo, *ACS Appl. Mater. Interfaces*, 2019, **11**, 9343–9354.

237 P. Bhanja, K. Bhunia, S. K. Das, D. Pradhan, R. Kimura, Y. Hijikata, S. Irle and A. Bhaumik, *ChemSusChem*, 2017, **10**, 921–929.

238 S. Liu, L. Yao, Y. Lu, X. Hua, J. Liu, Z. Yang, H. Wei and Y. Mai, *Mater. Lett.*, 2019, **236**, 354–357.

239 Y. Han, Q. Zhang, N. T. Hu, X. Zhang, Y. Y. Mai, J. Q. Liu, X. L. Hua and H. Wei, *Chin. Chem. Lett.*, 2017, **28**, 2269–2273.

240 Z. Q. Zha, L. R. Xu, Z. K. Wang, X. G. Li, Q. M. Pan, P. A. Hu and S. B. Lei, *ACS Appl. Mater. Interfaces*, 2015, **7**, 17837–17843.

241 P. Y. Wang, Q. Wu, L. F. Han, S. Wang, S. M. Fang, Z. H. Zhang and S. M. Sun, *RSC Adv.*, 2015, **5**, 27290–27294.

242 Y. Wu, D. W. Yan, Z. Y. Zhang, M. M. Matsushita and K. Awaga, *ACS Appl. Mater. Interfaces*, 2019, **11**, 7661–7665.

243 A. K. Mohammed, V. Vijayakumar, A. Halder, M. Ghosh, M. Addicoat, U. Bansode, S. Kurungot and R. Banerjee, *ACS Appl. Mater. Interfaces*, 2019, **11**, 30828–30837.

244 J. S. Xu, Y. F. He, S. Bi, M. Wang, P. Yang, D. Q. Wu, J. J. Wang and F. Zhang, *Angew. Chem., Int. Ed.*, 2019, **58**, 12065–12069.

245 C. R. Mulzer, L. X. Shen, R. P. Bisbey, J. R. McKone, N. Zhang, H. D. Abruña and W. R. Dichtel, *ACS Cent. Sci.*, 2016, **2**, 667–673.

246 B. Sun, J. Liu, A. M. Cao, W. G. Song and D. Wang, *Chem. Commun.*, 2017, **53**, 6303–6306.

247 Y. Z. Liao, J. H. Li and A. Thomas, *ACS Macro Lett.*, 2017, **6**, 1444–1450.

248 Y. Han, N. Hu, S. Liu, Z. Hou, J. Liu, X. Hua, Z. Yang, L. Wei, L. Wang and H. Wei, *Nanotechnology*, 2017, **28**, 33LT01.

249 C. R. DeBlase, K. Hernández-Burgos, K. E. Silberstein, G. G. Rodriguez-Calero, R. P. Bisbey, H. D. Abruna and W. R. Dichtel, *ACS Nano*, 2015, **9**, 3178–3183.

250 A. M. Khattak, Z. A. Ghazi, B. Liang, N. A. Khan, A. Iqbal, L. S. Li and Z. Y. Tang, *J. Mater. Chem. A*, 2016, **4**, 16312–16317.

251 A. F. M. El-Mahdy, M. G. Mohamed, T. H. Mansoure, H. H. Yu, T. Chen and S. W. Kuo, *Chem. Commun.*, 2019, **55**, 14890–14893.

252 T. Li, X. D. Yan, Y. Liu, W. D. Zhang, Q. T. Fu, H. Y. Zhu, Z. J. Li and Z. G. Gu, *Polym. Chem.*, 2020, **11**, 47–52.

253 D. W. Yan, Y. Wu, R. Kitauraa and K. Awaga, *J. Mater. Chem. A*, 2019, **7**, 26829–26837.

254 T. Li, W. D. Zhang, Y. Liu, Y. X. Li, C. K. Cheng, H. Y. Zhu, X. D. Yan, Z. J. Li and Z. G. Gu, *J. Mater. Chem. A*, 2019, **7**, 19676–19681.

255 Y. Yusran, H. Li, X. Guan, D. Li, L. Tang, M. Xue, Z. Zhuang, Y. Yan, V. Valtchev, S. Qiu and Q. Fang, *Adv. Mater.*, 2020, **32**, 1907289.

256 Q. Xu, Y. P. Tang, L. P. Zhai, Q. H. Chen and D. L. Jiang, *Chem. Commun.*, 2017, **53**, 11690–11693.

257 J. Romero, D. Rodriguez-San-Miguel, A. Ribera, R. Mas-Ballesté, T. F. Otero, I. Manet, F. Licio, G. Abellán, F. Zamora and E. Coronado, *J. Mater. Chem. A*, 2017, **5**, 4343–4351.

258 G. Kim, J. Yang, N. Nakashima and T. Shiraki, *Chem. – Eur. J.*, 2017, **23**, 17504–17510.

259 H. T. Wei, J. D. Ning, X. Cao, X. H. Li and L. Hao, *J. Am. Chem. Soc.*, 2018, **140**, 11618–11622.

260 L. L. Zhang and X. S. Zhao, *Chem. Soc. Rev.*, 2009, **38**, 2520–2531.

261 M. Kim, P. Puthiaraj, Y. J. Qian, Y. Kim, S. Jang, S. Hwang, E. Na, W. S. Ahn and S. E. Shim, *Electrochim. Acta*, 2018, **284**, 98–107.

262 Y. Y. Lei, X. M. Liang, L. Yang, P. Jiang, Z. Y. Lei, S. S. Wu and J. W. Feng, *J. Mater. Chem. A*, 2020, **8**, 4376–4385.

263 Y. Q. Li, X. T. Xu, S. J. Hou, J. Q. Ma, T. Lu, J. C. Wang, Y. F. Yao and L. K. Pan, *Chem. Commun.*, 2018, **54**, 14009–14012.

264 Y. Shao, M. F. El-Kady, J. Sun, Y. Li, Q. Zhang, M. Zhu, H. Wang, B. Dunn and R. B. Kaner, *Chem. Rev.*, 2018, **118**, 9233–9280.

265 X. X. Lin, P. Peng, J. N. Guo and Z. H. Xiang, *Chem. Eng. J.*, 2019, **358**, 427–434.

266 P. Kaur, J. T. Hupp and S. T. Nguyen, *ACS Catal.*, 2011, **1**, 819–835.

267 H. Zhu, D. X. Liu, D. T. Zou and J. Y. Zhang, *J. Mater. Chem. A*, 2018, **6**, 6130–6154.

268 W. G. Tu, Y. Xu, S. M. Yin and R. Xu, *Adv. Mater.*, 2018, **30**, 1707582.

269 X. Meng and F. S. Xiao, *Chem. Rev.*, 2014, **114**, 1521–1543.

270 K. L. Yeung and W. Han, *Catal. Today*, 2014, **236**, 182–205.

271 S. J. Lyle, P. J. Waller and O. M. Yaghi, *Trends Chem.*, 2019, **1**, 172–184.

272 X. Y. Guan, H. Li, Y. C. Ma, M. Xue, Q. R. Fang, Y. S. Yan, V. Valtchev and S. L. Qiu, *Nat. Chem.*, 2019, **11**, 587–594.

273 M. H. Shao, Q. W. Chang, J. P. Dodelet and R. Chenitz, *Chem. Rev.*, 2016, **116**, 3594–3657.

274 L. M. Dai, Y. H. Xue, L. T. Qu, H. J. Choi and J. B. Baek, *Chem. Rev.*, 2015, **115**, 4823–4892.

275 Y. J. Wang, N. Zhao, B. Fang, H. Li, X. T. Bi and H. Wang, *Chem. Rev.*, 2015, **115**, 3433–3467.

276 Y. Jiao, Y. Zheng, M. Jaroniec and S. Z. Qiao, *Chem. Soc. Rev.*, 2015, **44**, 2060–2086.

277 Y. G. Li and H. J. Dai, *Chem. Soc. Rev.*, 2014, **43**, 5257–5275.

278 A. C. Chen and P. Holt-Hindle, *Chem. Rev.*, 2010, **110**, 3767–3804.

279 M. Zhou, H. L. Wang and S. J. Guo, *Chem. Soc. Rev.*, 2016, **45**, 1273–1307.

280 G. Wu and P. Zelenay, *Acc. Chem. Res.*, 2013, **46**, 1878–1889.

281 F. Jaouen, E. Proietti, M. Lefèvre, R. Chenitz, J. P. Dodelet, G. Wu, H. T. Chung, C. M. Johnston and P. Zelenay, *Energy Environ. Sci.*, 2011, **4**, 114–130.

282 Q. Xu, Y. P. Tang, X. B. Zhang, Y. Oshima, Q. H. Chen and D. L. Jiang, *Adv. Mater.*, 2018, **30**, 1706330.

283 Q. P. Lin, X. H. Bu, A. G. Kong, C. Y. Mao, F. Bu and P. Y. Feng, *Adv. Mater.*, 2015, **27**, 3431–3436.

This journal is © The Royal Society of Chemistry 2020

Chem. Soc. Rev., 2020, **49**, 3565–3604 | **3603**

284 Q. Zuo, G. Z. Cheng and W. Luo, *Dalton Trans.*, 2017, **46**, 9344–9348.

285 S. B. Ren, J. Wang and X. H. Xia, *ACS Appl. Mater. Interfaces*, 2016, **8**, 25875–25880.

286 W. J. Ma, P. Yu, T. Ohsaka and L. Q. Mao, *Electrochem. Commun.*, 2015, **52**, 53–57.

287 X. H. He, Q. He, Y. C. Deng, M. Peng, H. Y. Chen, Y. Zhang, S. Y. Yao, M. T. Zhang, D. Q. Xiao, D. Ma, B. H. Ge and H. B. Ji, *Nat. Commun.*, 2019, **10**, 3663.

288 X. J. Zhao, P. Pachfule, S. Li, T. Langenhahn, M. Y. Ye, G. Y. Tian, J. Schmidt and A. Thomas, *Chem. Mater.*, 2019, **31**, 3274–3280.

289 P. Peng, L. Shi, F. Huo, C. X. Mi, X. H. Wu, S. J. Zhang and Z. H. Xiang, *Sci. Adv.*, 2019, **5**, eaaw2322.

290 W. P. Liu, C. M. Wang, L. J. Zhang, H. H. Pan, W. B. Liu, J. Chen, D. J. Yang, Y. J. Xiang, K. Wang, J. Z. Jiang and X. D. Yao, *J. Mater. Chem. A*, 2019, **7**, 3112–3119.

291 Q. Zhao, Z. H. Yan, C. C. Chen and J. Chen, *Chem. Rev.*, 2017, **117**, 10121–10211.

292 S. W. Sheehan, J. M. Thomsen, U. Hintermair, R. H. Crabtree, G. W. Brudvig and C. A. Schmuttenmaer, *Nat. Commun.*, 2015, **6**, 6469.

293 J. D. Blakemore, R. H. Crabtree and G. W. Brudvig, *Chem. Rev.*, 2015, **115**, 12974–13005.

294 Y. Hou, M. Qiu, T. Zhang, J. Ma, S. Liu, X. Zhuang, C. Yuan and X. Feng, *Adv. Mater.*, 2017, **29**, 1604480.

295 M. Shalom, D. Ressnig, X. F. Yang, G. Clavel, T. P. Fellinger and M. Antonietti, *J. Mater. Chem. A*, 2015, **3**, 8171–8177.

296 X. Y. Lu and C. Zhao, *Nat. Commun.*, 2015, **6**, 6616.

297 J. R. Galán-Mascarós, *ChemElectroChem*, 2015, **2**, 37–50.

298 B. Zhang, X. L. Zheng, O. Voznyy, R. Comin, M. Bajdich, M. García-Melchor, L. L. Han, J. X. Xu, M. Liu, L. R. Zheng, F. P. García de Arquer, C. T. Dinh, F. J. Fan, M. J. Yuan, E. Yassitepe, N. Chen, T. Regier, P. F. Liu, Y. H. Li, P. De Luna, A. Janmohamed, H. L. Xin, H. G. Yang, A. Vojvodic and E. H. Sargent, *Science*, 2016, **352**, 333–337.

299 H. B. Aiyappa, J. Thote, D. B. Shinde, R. Banerjee and S. Kurungot, *Chem. Mater.*, 2016, **28**, 4375–4379.

300 X. J. Zhao, P. Pachfule, S. Li, T. Langenhahn, M. Ye, C. Schlesiger, S. Praetz, J. Schmidt and A. Thomas, *J. Am. Chem. Soc.*, 2019, **141**, 6623–6630.

301 D. Mullangi, V. Dhavale, S. Shalini, S. Nandi, S. Collins, T. Woo, S. Kurungot and R. Vaidhyanathan, *Adv. Energy Mater.*, 2016, **6**, 1600110.

302 S. Nandi, S. K. Singh, D. Mullangi, R. Illathvalappil, L. George, C. P. Vinod, S. Kurungot and R. Vaidhyanathan, *Adv. Energy Mater.*, 2016, **6**, 1601189.

303 D. Chakraborty, S. Nandi, R. Illathvalappil, D. Mullangi, R. Maity, S. K. Singh, S. Haldar, C. P. Vinod, S. Kurungot and R. Vaidhyanathan, *ACS Omega*, 2019, **4**, 13465–13473.

304 H. X. Jia, Z. J. Sun, D. C. Jiang and P. W. Du, *Chem. Mater.*, 2015, **27**, 4586–4593.

305 M. S. Dresselhaus and I. L. Thomas, *Nature*, 2001, **414**, 332–337.

306 Y. Yan, T. He, B. Zhao, K. Qi, H. F. Liu and B. Y. Xia, *J. Mater. Chem. A*, 2018, **6**, 15905–15926.

307 E. J. Popczun, J. R. McKone, C. G. Read, A. J. Biacchi, A. M. Wiltrout, N. S. Lewis and R. E. Schaak, *J. Am. Chem. Soc.*, 2013, **135**, 9267–9270.

308 S. Bhunia, S. K. Das, R. Jana, S. C. Peter, S. Bhattacharya, M. Addicoat, A. Bhaumik and A. Pradhan, *ACS Appl. Mater. Interfaces*, 2017, **9**, 23843–23851.

309 D. Zhou, X. Y. Tan, H. M. Wu, L. H. Tian and M. Li, *Angew. Chem., Int. Ed.*, 2019, **58**, 1376–1381.

310 M. A. Lukowski, A. S. Danie, F. Meng, A. Forticaux, L. S. Li and S. Jin, *J. Am. Chem. Soc.*, 2013, **135**, 10274–10277.

311 J. L. Qiao, Y. Y. Liu, F. Hong and J. J. Zhang, *Chem. Soc. Rev.*, 2014, **43**, 631–675.

312 C. Costentin, M. Robert and J. M. Saveant, *Chem. Soc. Rev.*, 2013, **42**, 2423–2436.

313 D. D. Zhu, J. L. Liu and S. Z. Qiao, *Adv. Mater.*, 2016, **28**, 3423–3452.

314 A. S. Agarwal, Y. Zhai, D. Hill and N. Sridhar, *ChemSusChem*, 2011, **4**, 1301–1310.

315 R. Schlogl, *Angew. Chem., Int. Ed.*, 2015, **54**, 3465–3520.

316 H. L. Wu, M. Zeng, X. Zhu, C. C. Tian, B. B. Mei, Y. Song, X. L. Du, Z. Jiang, C. G. Xia and S. Dai, *ChemElectroChem*, 2018, **5**, 2717–2721.

317 X. Zhang, H. Y. Liu, J. Q. Qin, H. S. Han, C. X. Qiu, S. Y. Zhang, X. Y. Hao, W. Liu and Y. J. Song, *Chem. Commun.*, 2019, **55**, 5659–5662.

318 M. H. Zhu, D. T. Yang, R. Q. Ye, J. Zeng, N. Corbin and K. Manthiram, *Catal. Sci. Technol.*, 2019, **9**, 974–980.

319 E. M. Johnson, R. Haiges and S. C. Marinescu, *ACS Appl. Mater. Interfaces*, 2018, **10**, 37919–37927.

320 P. L. Cheung, S. K. Lee and C. P. Kubiak, *Chem. Mater.*, 2019, **31**, 1908–1919.

321 C. L. Yao, J. C. Li, W. Gao and Q. Jiang, *Chem. – Eur. J.*, 2018, **24**, 11051–11058.

322 C. S. Diercks, S. Lin, N. Kornienko, E. A. Kapustin, E. M. Nichols, C. Zhu, Y. Zhao, C. J. Chang and O. M. Yaghi, *J. Am. Chem. Soc.*, 2018, **140**, 1116–1122.

323 D. A. Popov, J. M. Luna, N. M. Orchanian, R. Haiges, C. A. Downes and S. C. Marinescu, *Dalton Trans.*, 2018, **47**, 17450–17460.

324 H. Y. Liu, J. Chu, Z. L. Yin, X. Cai, L. Zhuang and H. X. Deng, *Chem*, 2018, **4**, 1696–1709.

325 X. Zhu, C. C. Tian, H. H. Wu, Y. Y. He, L. He, H. Wang, X. D. Zhuang, H. L. Liu, C. G. Xia and S. Dai, *ACS Appl. Mater. Interfaces*, 2018, **10**, 43588–43594.

326 Y. H. Wang, J. X. Chen, G. X. Wang, Y. Li and Z. H. Wen, *Angew. Chem., Int. Ed.*, 2018, **57**, 13120–13124.

327 M. A. Khayum, M. Ghosh, V. Vijayakumar, A. Halder, M. Nurhuda, S. Kumar, M. Addicoat, S. Kurungot and R. Banerjee, *Chem. Sci.*, 2019, **10**, 8889–8894.

328 X. Li, H. Wang, Z. Chen, H. S. Xu, W. Yu, C. Liu, X. Wang, K. Zhang, K. Xie and K. P. Loh, *Adv. Mater.*, 2019, **31**, 1905879.

329 D. D. Chen, S. Huang, L. Zhong, S. J. Wang, M. Xiao, D. M. Han and Y. Z. Meng, *Adv. Funct. Mater.*, 2019, **30**, 1907717.

330 S. Liu, M. F. Wang, T. Qian, H. Q. Ji, J. Liu and C. L. Yan, *Nat. Commun.*, 2019, **10**, 3898.

3604 | *Chem. Soc. Rev.*, 2020, **49**, 3565–3604

This journal is © The Royal Society of Chemistry 2020